NASA CR-134979

(NASA-CR-134979) THREE DIMENSIONAL THRUST CHAMBER LIFE PREDICTION Final Contractor Report (Boeing Aerospace Co., Seattle, Wash.) 119 p HC $5.50 CSCL 21H

N76-19229

Unclas
G3/20 20733

3-DIMENSIONAL THRUST CHAMBER LIFE PREDICTION

CONTRACT NAS3-19717

MARCH 1976

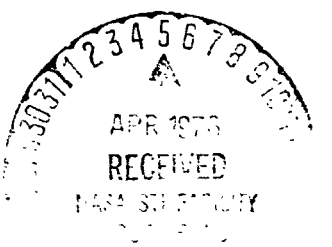

PREPARED BY
BOEING AEROSPACE COMPANY
(A DIVISION OF THE BOEING COMPANY)
RESEARCH AND ENGINEERING
SEATTLE, WASHINGTON

PREPARED FOR
NATIONAL AERONAUTICS AND SPACE ADMINISTRATION
LEWIS RESEARCH CENTER
CLEVELAND, OHIO

1. Report No.	2. Government Accession No.	3. Recipient's Catalog No.
NASA CR-134979		

4. Title and Subtitle	5. Report Date
3-D THRUST CHAMBER LIFE PREDICTION	March 1976
	6. Performing Organization Code

7. Author(s)	8. Performing Organization Report No.
William H. Armstrong and E. W. Brogren	D180-19309-1
	10. Work Unit No.

9. Performing Organization Name and Address	11. Contract or Grant No.
Boeing Aerospace Company (A Division of The Boeing Company) P.O. Box 3999 Seattle, Wasnington 98124	NAS3-19717
	13. Type of Report and Period Covered
12. Sponsoring Agency Name and Address	Final Contractor Report
National Aeronautics and Space Administration Lewis Research Center	14. Sponsoring Agency Code

15. Supplementary Notes

R. J. Quentmeyer, NASA Technical Monitor

16. Abstract

A study was performed to analytically determine the cyclic thermomechanical behavior and fatigue life of three configurations of the NASA/LeRC Plug Nozzle Thrust Chamber. This thrust chamber is a test model which represents the current trend in nozzle design calling for high performance coupled with weight and volume limitations as well as extended life for reusability. The study involved the use of different materials and material combinations to evaluate their application to the problem of low-cycle fatigue in the thrust chamber. The thermal and structural analyses were carried out on a three-dimensional basis.

Results are presented which show plots of continuous temperature histories and temperature distributions at selected times during the operating cycle of the thrust chamber. Computed structural data show critical regions for low-cycle fatigue and the histories of strain within the regions for each operating cycle. Comparisons of data obtained from 2-dimensional and 3-dimensional models show the importance of modeling to prediction of cyclic life in these structures.

17. Key Words (Suggested by Author(s))	18. Distribution Statement
Thrust Chamber, Low-Cycle Fatigue, Heat Transfer, Thermal Analysis, Inelastic, Viscoplastic, Finite-Element Analysis, Copper Alloys	Unclassified - Unlimited

19. Security Classif. (of this report)	20. Security Classif. (of this page)	21. No. of Pages	22. Price*
Unclassified	Unclassified	119	

*For sale by the National Technical Information Service, Springfield, Virginia 22151

TABLE OF CONTENTS

LIST OF FIGURES

LIST OF FIGURES (Contir d)

LIST OF FIGURES (Continued)

LIST OF FIGURES (Continued)

LIST OF FIGURES (Continued)

LIST OF FIGURES (Continued)

LIST OF TABLES

FOREWORD

This report was prepared by the Boeing Aerospace Company, Seattle, Washington, for the Lewis Research Center (LeRC) of the National Aeronautics and Space Administration (NASA). Life analyses of three configurations of the LeRC plug nozzle thrust chamber outer cylinder were conducted in accordance with requirements of Contract NAS3-19717 "3-D Thrust Chamber Life Prediction". The study was under the cognizance of R. J. Quentmeyer of NASA/LeRC.

The analyses and documentation of results were conducted by W. H. Armstrong and E. W. Brogren. The program manager was J. W. Straayer.

1.0 SUMMARY

The objective of this study was to analytically determine the cyclic thermomechanical behavior and fatigue life of three configurations of the NASA/LeRC Plug Nozzle Thrust Chamber. This thrust chamber is a test model which represents the current trend in nozzle design calling for high performance coupled with weight and volume limitations as well as extended life for reusability. The study involves the use of different materials and material combinations to evaluate their application to the problem of low-cycle fatigue in the thrust chamber.

The cyclic heat flow analysis was performed with the Boeing Engineering Thermal Analyzer (BETA) program. BETA is a large capacity digital computer program for computing transient or steady state heat flow in two or three dimensions.

Structural response to applied temperature/pressure loading cycles was determined with the Boeing Plastic Analysis Capability for 3-Dimensional Solids (BOPACE 3-D) digital computer program which provides capability to determine incremental viscoplastic behavior of a structure subjected to large changes in temperature, temperature gradients and pressure loading.

Results are presented which show plots of continuous temperature histories and diagrams of continuous isotherms at selected times during the operating cycle of the thrust chamber. Computed structural data show critical regions for low-cycle fatigue and the histories of strain within the regions for each operating cycle. Comparisons of data obtained from 2-dimensional and 3-dimensional models are presented. The comparisons show the importance of modeling to prediction of cyclic life in these structures.

2.0 INTRODUCTION

The advent of the Space Shuttle has brought a new era in the design and fabrication of rocket nozzles. The requirement of high-performance coupled with weight and volume limitations has resulted in the design of rocket nozzles that operate at chamber pressures in excess of 2000 N/cm^2 (3000 psia). This has elevated the throat heat flux from 3300 W/cm^2 (20 Btu/in^2-sec) for present day high performance rocket nozzles to 16,000 W/cm^2 (100 Btu/in^2-sec) for the Space Shuttle Main Engine. A further requirement for future high performance rocket nozzles is reusability. For example, the nozzle may have the requirement that it be capable of operating for several hundred major thermal cycles.

The combination of high performance and reusability has created major design problems. One of the critical aspects of the nozzle design is the fatigue life analysis. This has become a major design problem since a portion of the nozzle, particularly the throat section, is subjected to cyclic inelastic strain due to the large temperature gradient between the hot inner wall and the relatively cool outer shell during the engine start-stop transients as well as during the sustained burn period. This has a major impact on nozzle life and creates the need to accurately predict when an engine may fail.

An essential part of any life analysis program is the availability of the appropriate physical and mechanical properties which are needed as functions of temperature for the materials used in fabrication of high performance rocket nozzles. Recognizing this need, NASA has initiated programs to obtain the necessary data; in particular LeRC has programs to obtain high temperature material properties for several copper-base alloys. These alloys which show potential application as thrust chamber liners have been fabricated into thrust chamber test specimens so the material can be subjected to a combustion environment The goal of the LeRC research test program is to evaluate the materials for use in full scale engines.

3.0 PLUG NOZZLE THRUST CHAMBER

The structure analyzed during this study is the outer cylinder of a plug type thrust chamber shown in Figure 3.0-1. The overall assembly of the thrust chamber including the centerbody is shown along with the structural details of the outer cylinder.

The basic element of the cylinder assembly is the inner wall which contains seventy-two axial flow coolant channels of constant cross section. Three copper alloys were considered as candidate inner wall materials, and heat-transfer and structural analyses were performed to predict the thermomechanical response of each cylinder to a specified thrust chamber operating cycle. The inner wall materials were Amzirc, 1/2 hard; OFHC copper, fully annealed; and NARloy-Z, wrought; the three cylinders were designated configurations B.1, B.2 and B.3 respectively. The structural closeout wall of all three cylinders was electroformed copper.

The critical region of each cylinder assembly, i.e., the region of maximum operating temperature and strain was expected to be at the throat plane. Cylinder end conditions caused by the relatively massive 1.00-inch thick copper flanges were assumed to have a negligible effect on thermomechanical behavior at the throat. Consequently the three-dimensional (3-D) analyses of the cylinder were limited to a portion exclusive of the flanges. The portion of the cylinders subjected to 3-D analysis is indicated by the shaded region of Figure 3.0-1. This region extends 25.40 mm (1.00 inch) upstream and 20.32 (0.80 inch) downstream from the throat plane. The length of the cylinder between the flanges is 50.55 mm (1.99 inch); the throat plane is located approximately midway between the flanges.

3.1 THRUST CHAMBER MATERIAL PROPERTIES

An essential part of the life analysis study is the data which characterize material behavior in a given range of temperature, strain, and rate-of-strain. These constitutive data are intended to describe

3.1 (Continued)

a limited number of physical phenomena decided at the outset for a given material. Unfortunately, available data did not include all information necessary to characterize the copper alloys of the thrust chambers. For example, stress-strain hysteresis loops necessary for defining cyclic hardening characteristics were not available. Thus, plasticity data had to be developed from static monotonic stress-strain curves rather than material properties derived from laboratory test conditions which more closely simulate the high temperature and high strain rate thrust chamber cycle.

The material properties available for the thermal and structural analyses were taken from Reference 1. These properties define the typical temperature dependent character of density, thermal expansion, specific heat, thermal conductivity, modulus of elasticity, static stress-strain behavior, and low-cycle fatigue life of the thrust chamber materials. These properties are presented in Figures 3.1-1 through 3.1-30.

3.2 THERMOMECHANICAL BOUNDARY CONDITIONS

All thermomechanical parameters which served as cyclic boundary conditions in the heat transfer and structural analyses were furnished by the NASA LeRC Project Manager. The boundary conditions were based on measurements made by the NASA LeRC during tests of the plug nozzle thrust chamber. Conditions previously specified for 2-D models of the cylinder throat plane (References 2 and 3) are shown in Table 3.2-I for comparison with conditions prescribed for the 3-D study.

Operating condition data consisted of heat transfer coefficients on the chamber cylinder hot gas surface and in the cooling channels, hot gas surface adiabatic wall temperatures, coolant bulk temperatures, hot gas surface static wall pressures, and cooling channel static wall pressures. Values were constant during the cooling and heating phases of the engine operating cycle. The boundary values were assumed to vary linearly with time during transition periods between the cooling and

3.2 (Continued)

heating phases. The duration of each transition period as well as the durations of cooling and heating phases were specified and are defined in Table 3.2-I. The conditions for the 2-D analyses are listed on the last line of the table. The axial station-dependent values listed in the main body of the table were used for the 3-D analyses. Average 3-D values were computed for comparison with the 2-D boundary conditions. Heat transfer coefficients at the throat plane (station 5) in the 3-D data indicate slightly greater heating and slightly less cooling than in the 2-D case. All of the average 3-D quantities, however, tend toward less heating and greater or equal cooling relative to the 2-D values. It was expected, therefore that the temperatures from the 3-D heat transfer analyses would be somewhat lower than those from corresponding 2-D results of References 2 and 3.

The strain analyses assumed no external physical restraint or mechanical boundary conditions other than the static pressures listed in Table 3.2-I.

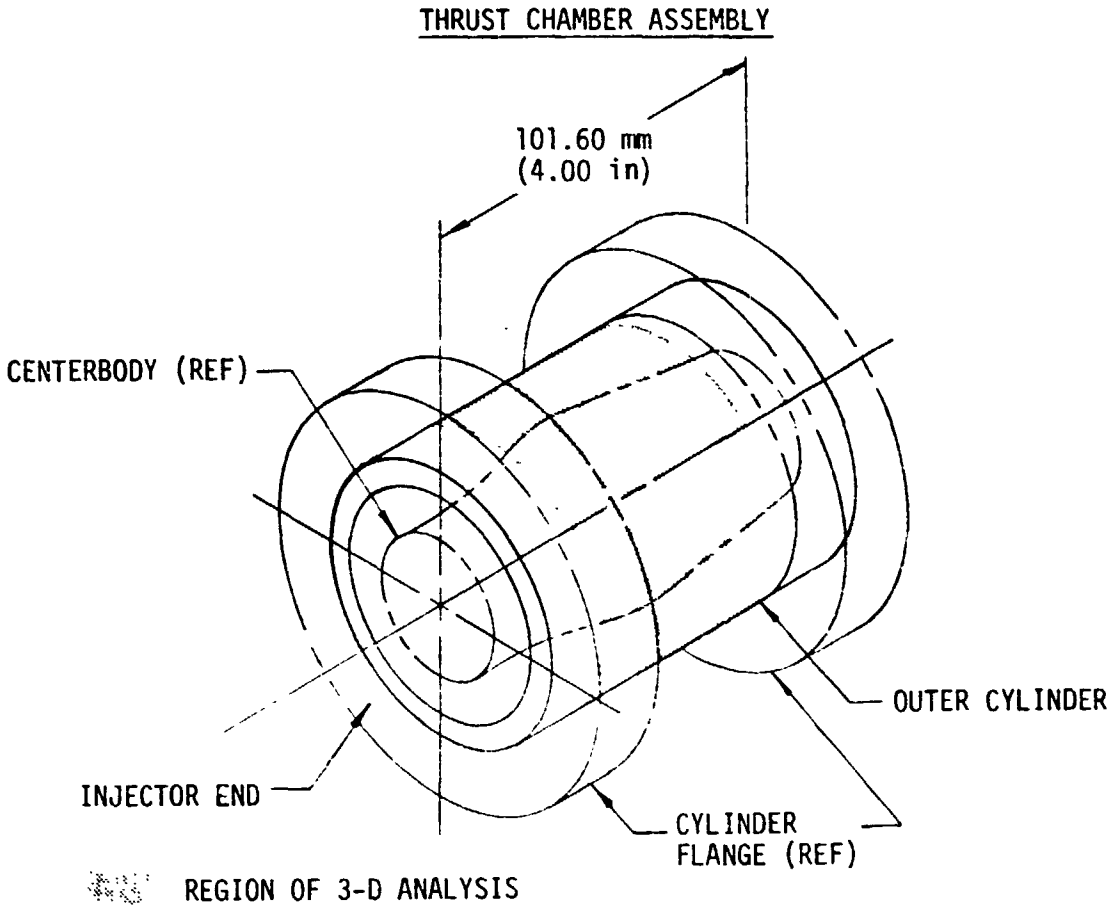

FIGURE 3.0-1 PLUG NOZZLE THRUST CHAMBER GEOMETRY

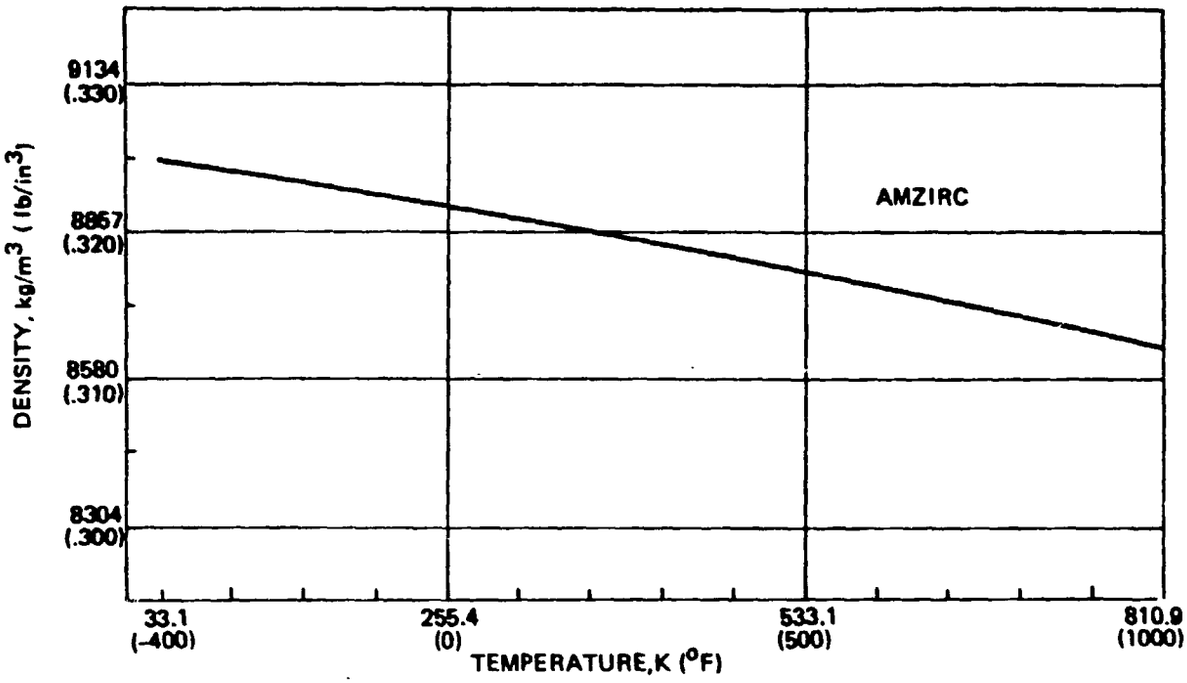

FIGURE 3.1-1 DENSITY VS. TEMPERATURE FOR AMZIRC

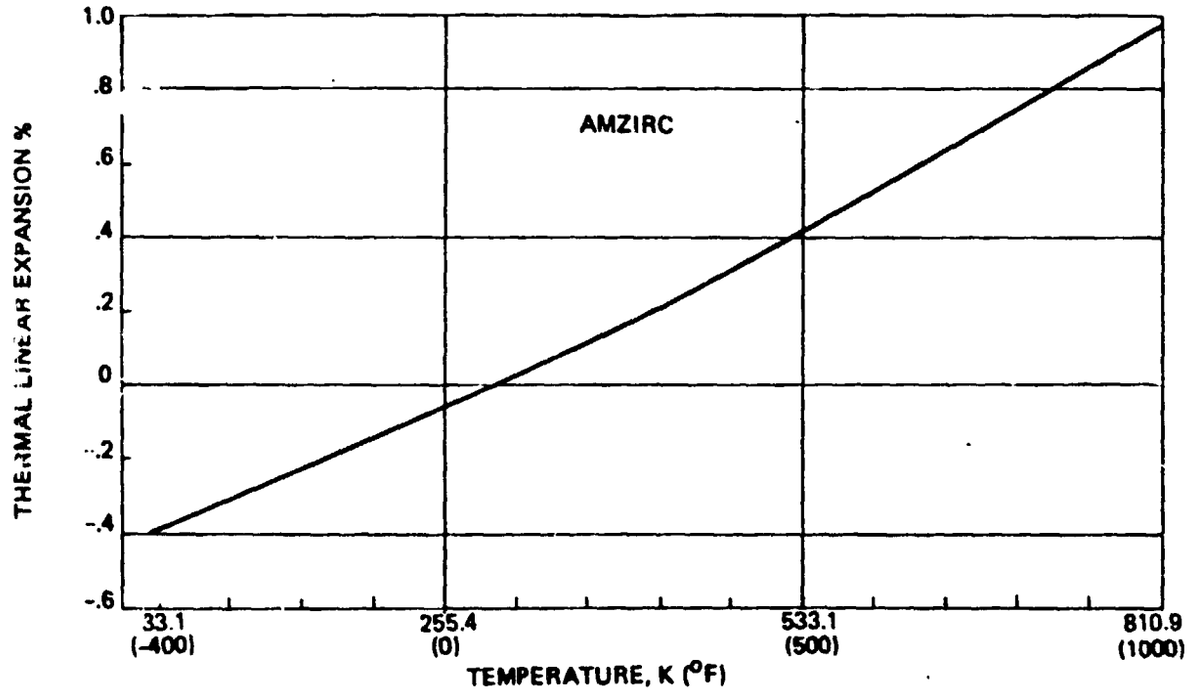

FIGURE 3.1-2 THERMAL LINEAR EXPANSION VS. TEMPERATURE FOR AMZIRC

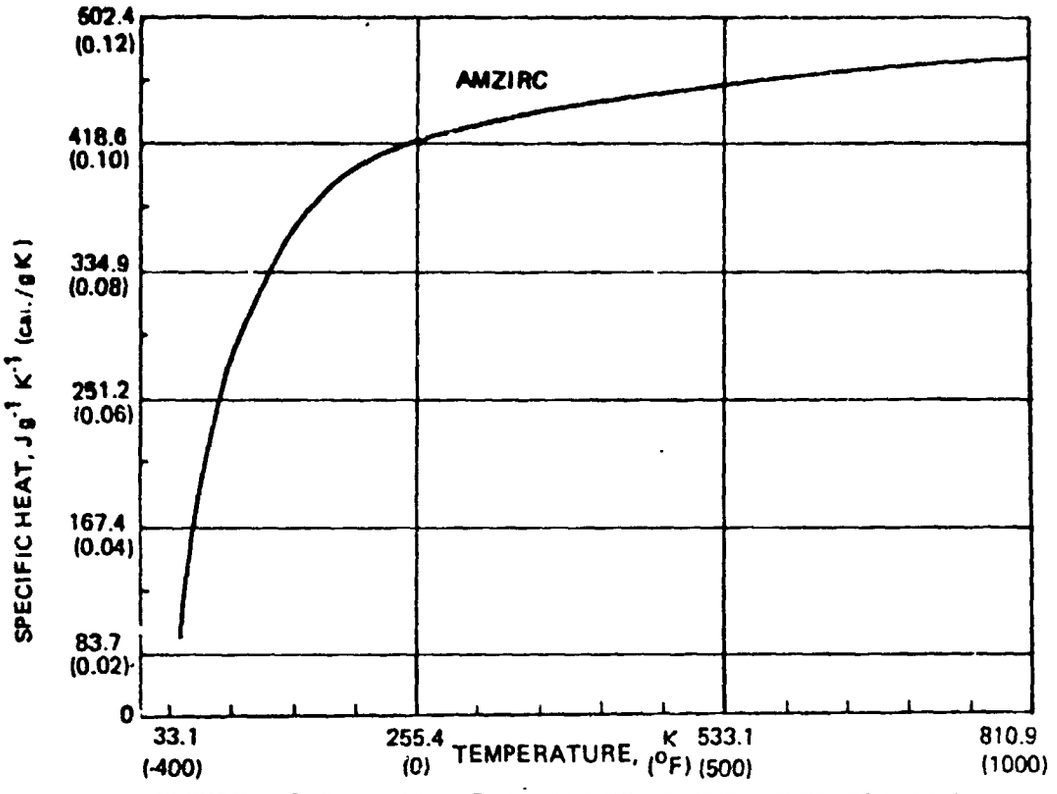

FIGURE 3.1-3 SPECIFIC HEAT VS. TEMPERATURE FOR AMZIRC

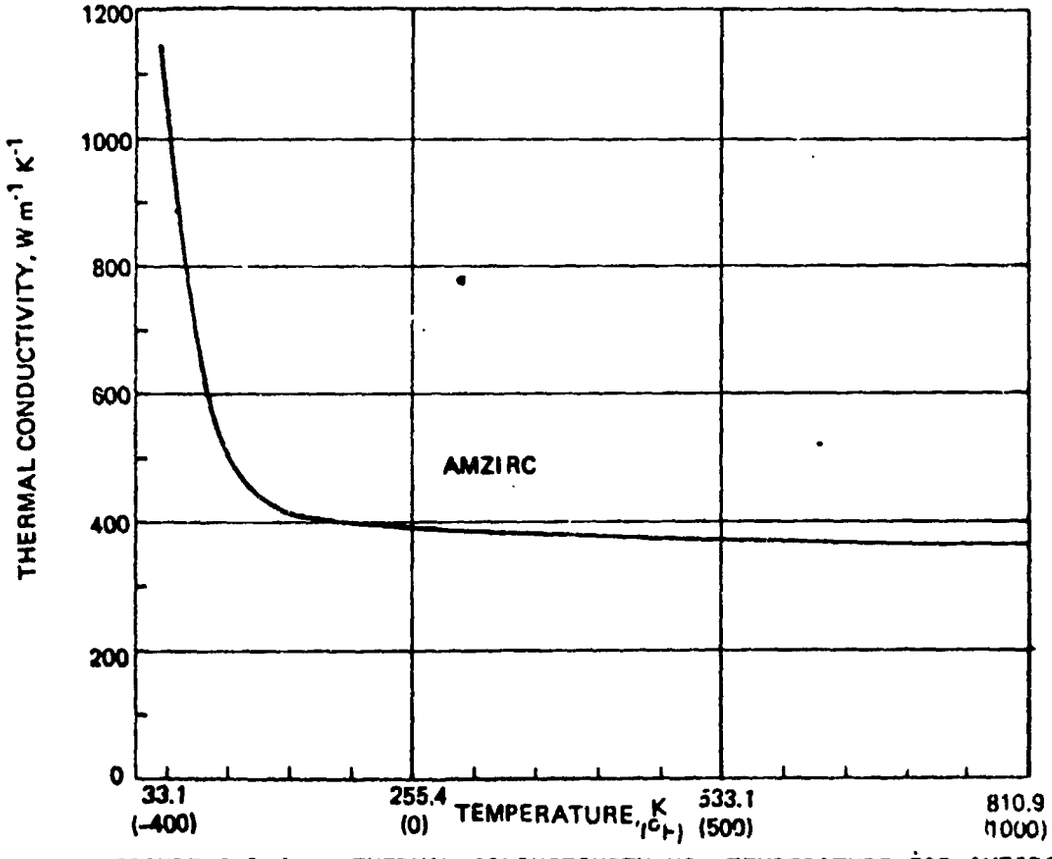

FIGURE 3.1-4 THERMAL CONDUCTIVITY VS. TEMPERATURE FOR AMZIRC

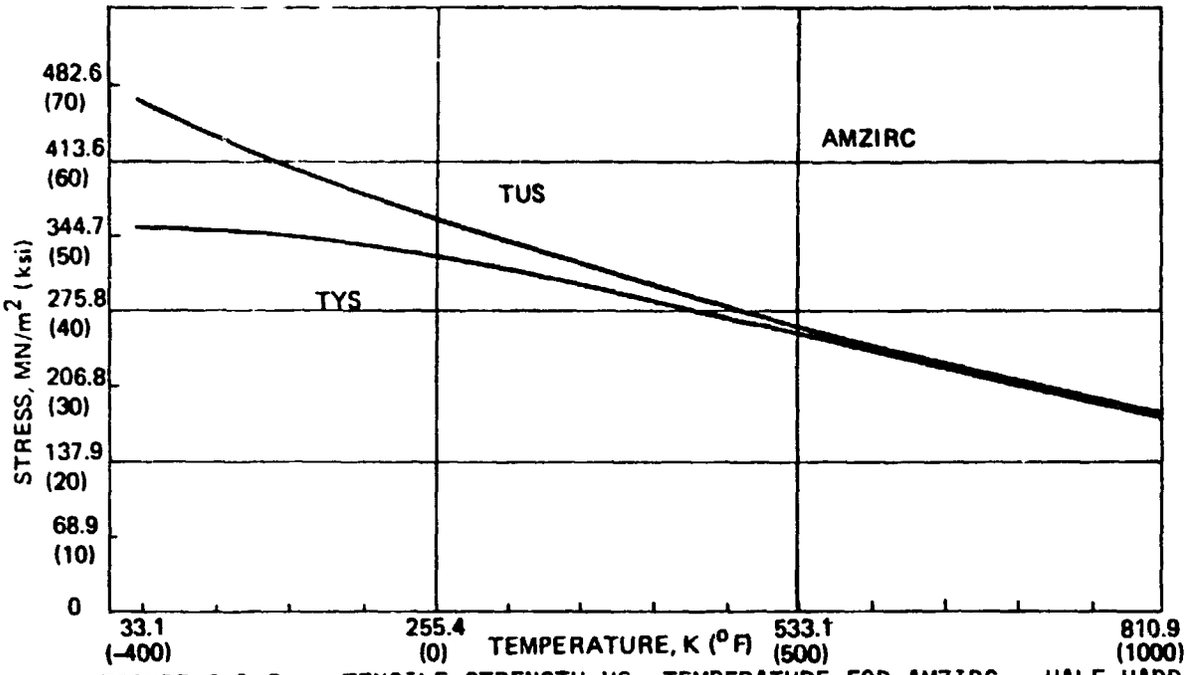

FIGURE 3.1-5 TENSILE STRENGTH VS. TEMPERATURE FOR AMZIRC - HALF HARD

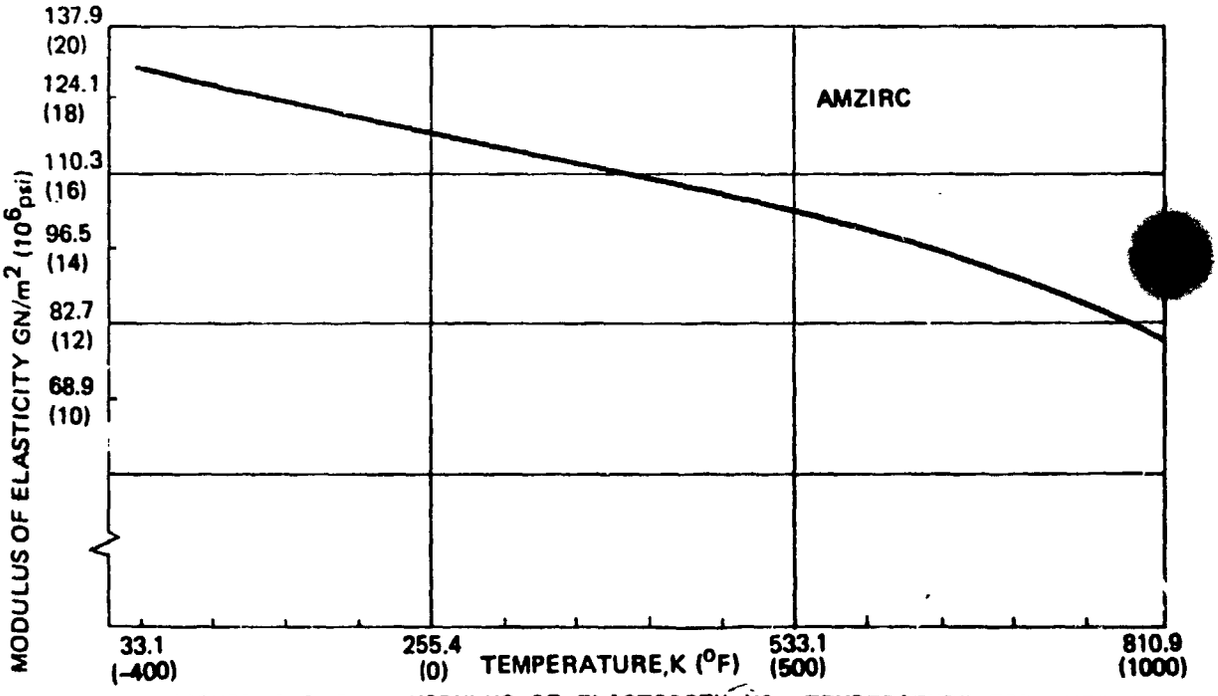

FIGURE 3.1-6 MODULUS OF ELASTICITY VS. TEMPERATURE FOR AMZIRC

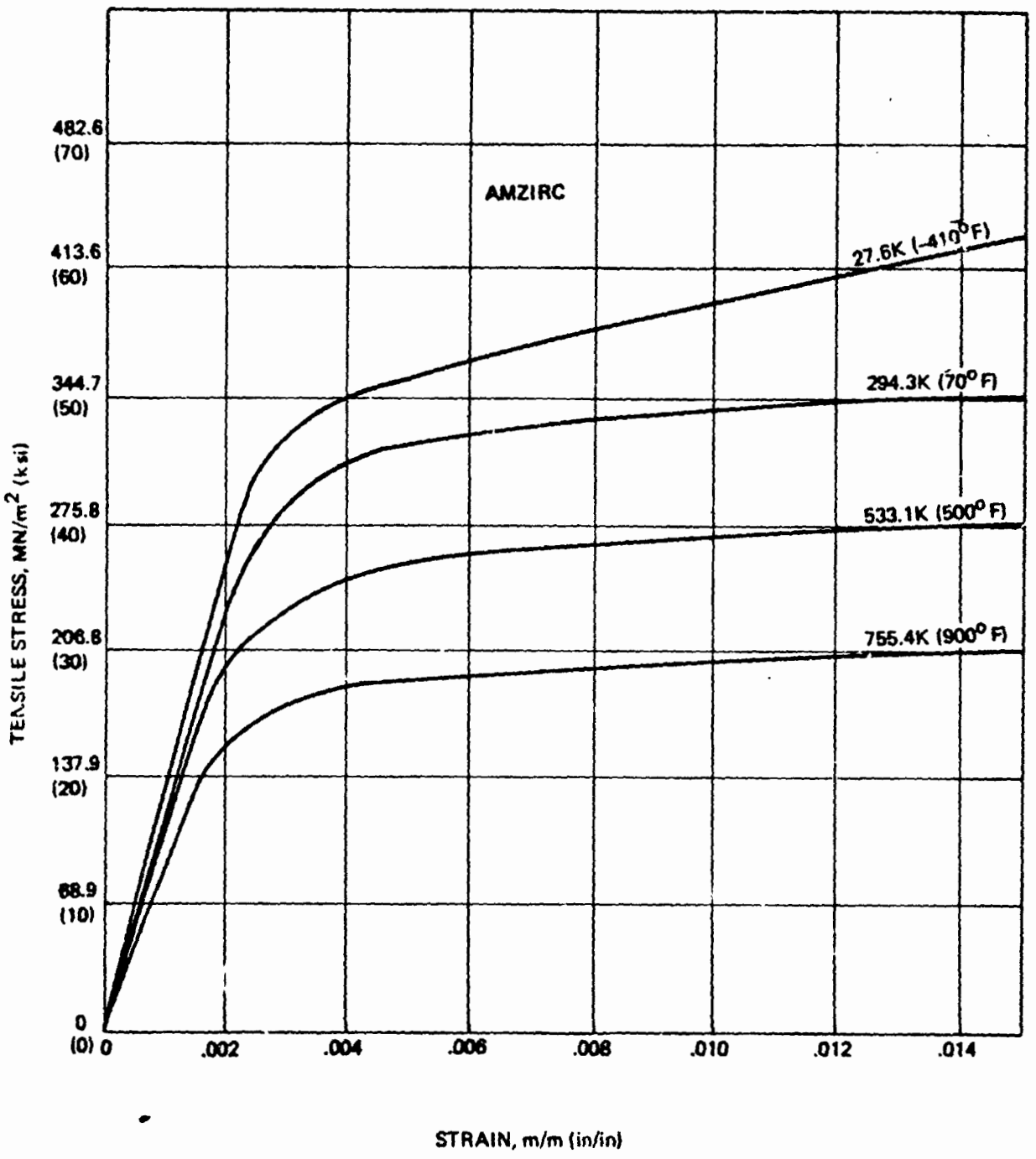

FIGURE 3.1-7 TYPICAL TENSILE STRESS-STRAIN CURVES FOR AMZIRC-HALF HARD CONDITION

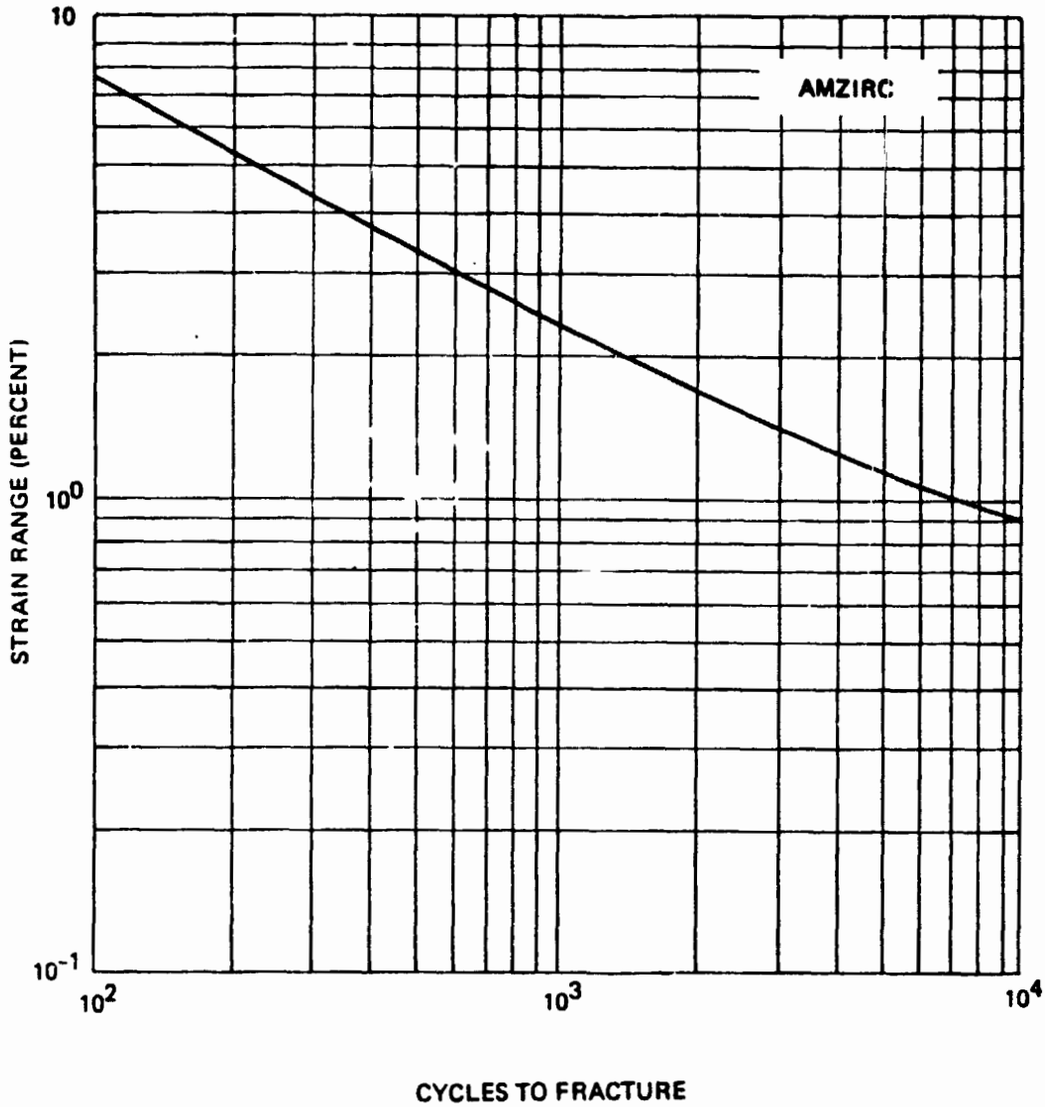

FIGURE 3.1-8 TYPICAL LOW-CYCLE FATIGUE LIFE OF AMZIRC - HALF HARD CONDITION

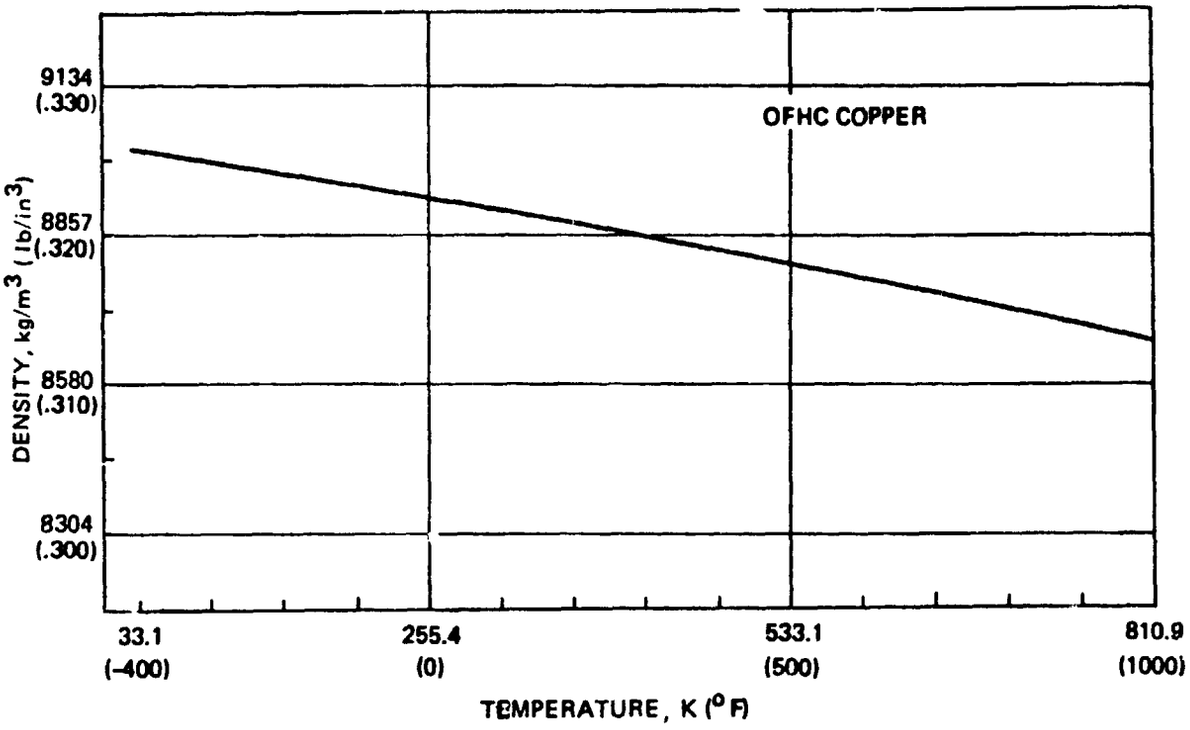

FIGURE 3.1-9 DENSITY VS. TEMPERATURE FOR OFHC COPPER

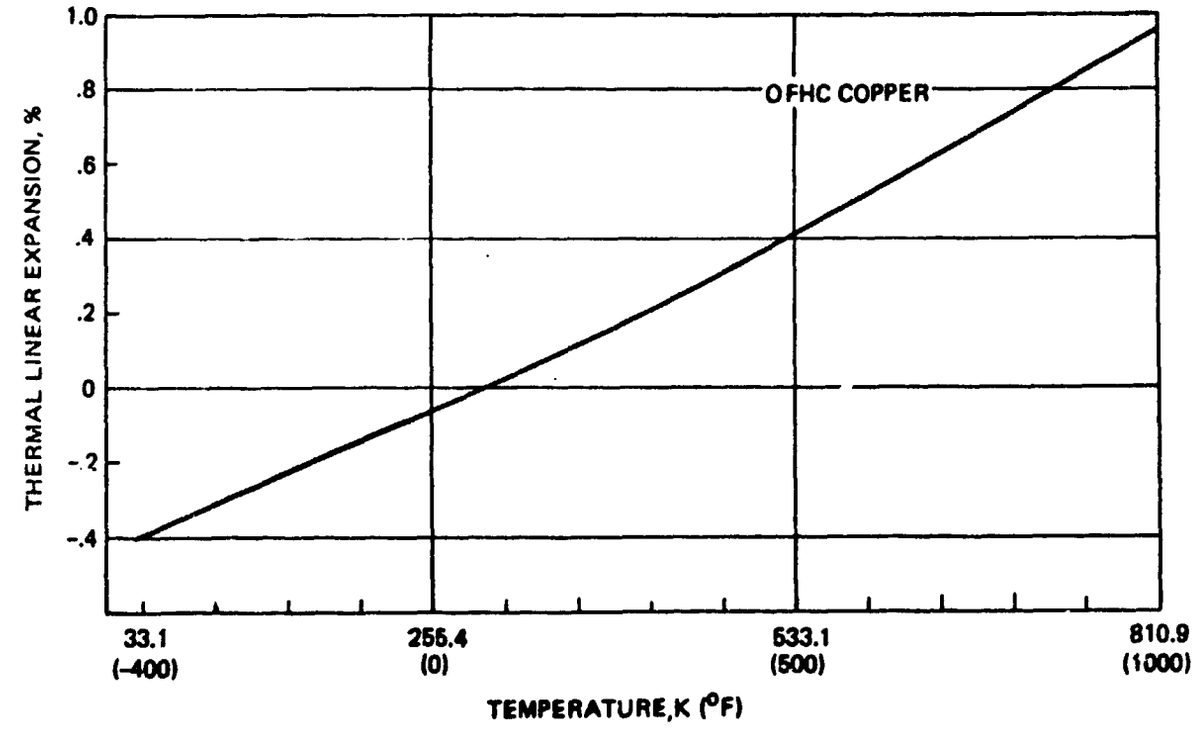

FIGURE 3.1-10 THERMAL LINEAR EXPANSION VS. TEMPERATURE FOR OFHC COPPER

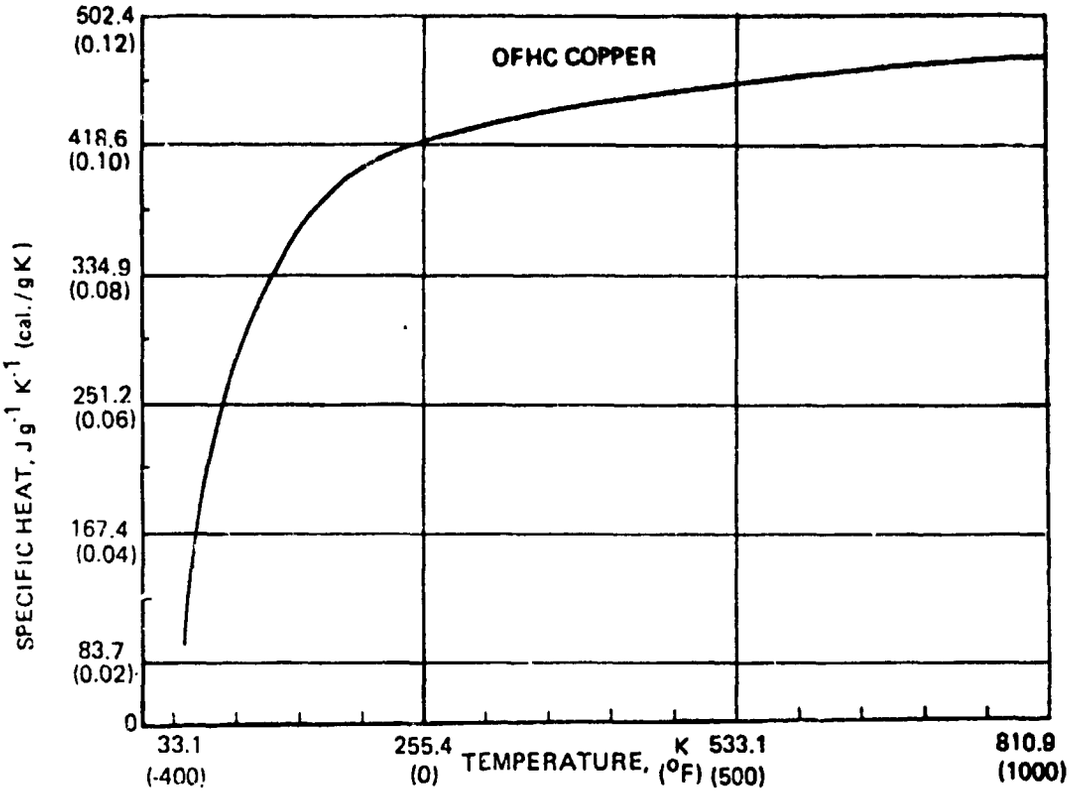

FIGURE 3.1-11 SPECIFIC HEAT VS. TEMPERATURE FOR OFHC COPPER

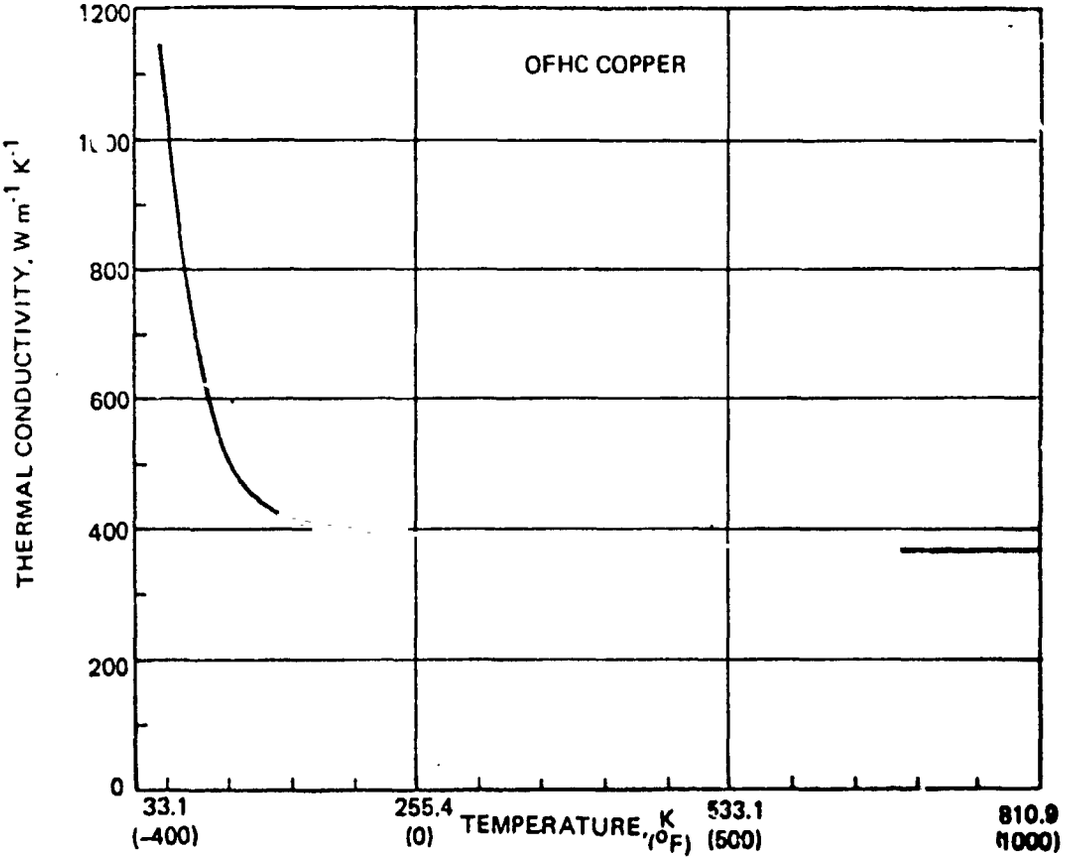

FIGURE 3.1-12 THERMAL CONDUCTIVITY VS. TEMPERATURE FOR OFHC COPPER

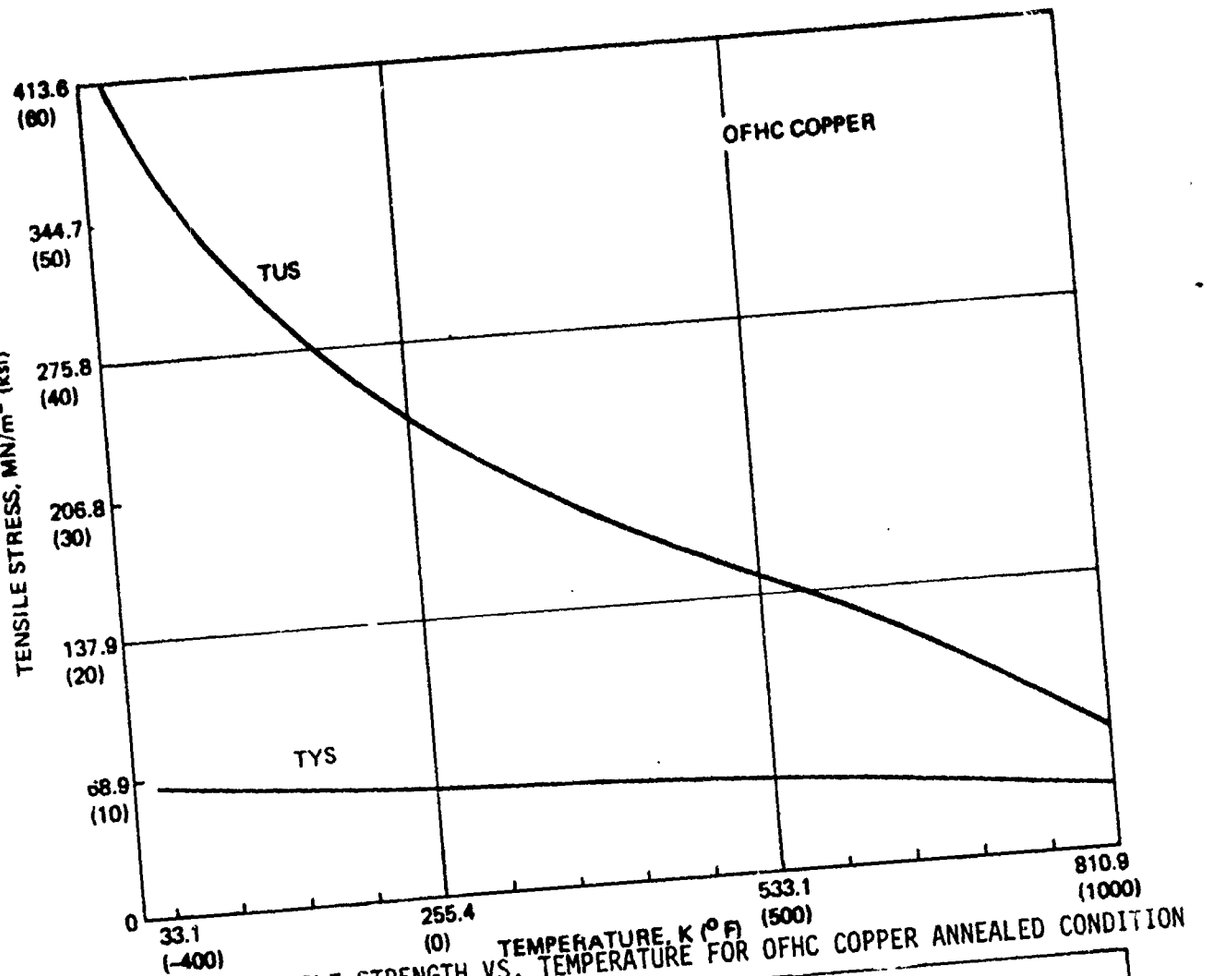

FIGURE 3.1-13 TENSILE STRENGTH VS. TEMPERATURE FOR OFHC COPPER ANNEALED CONDITION

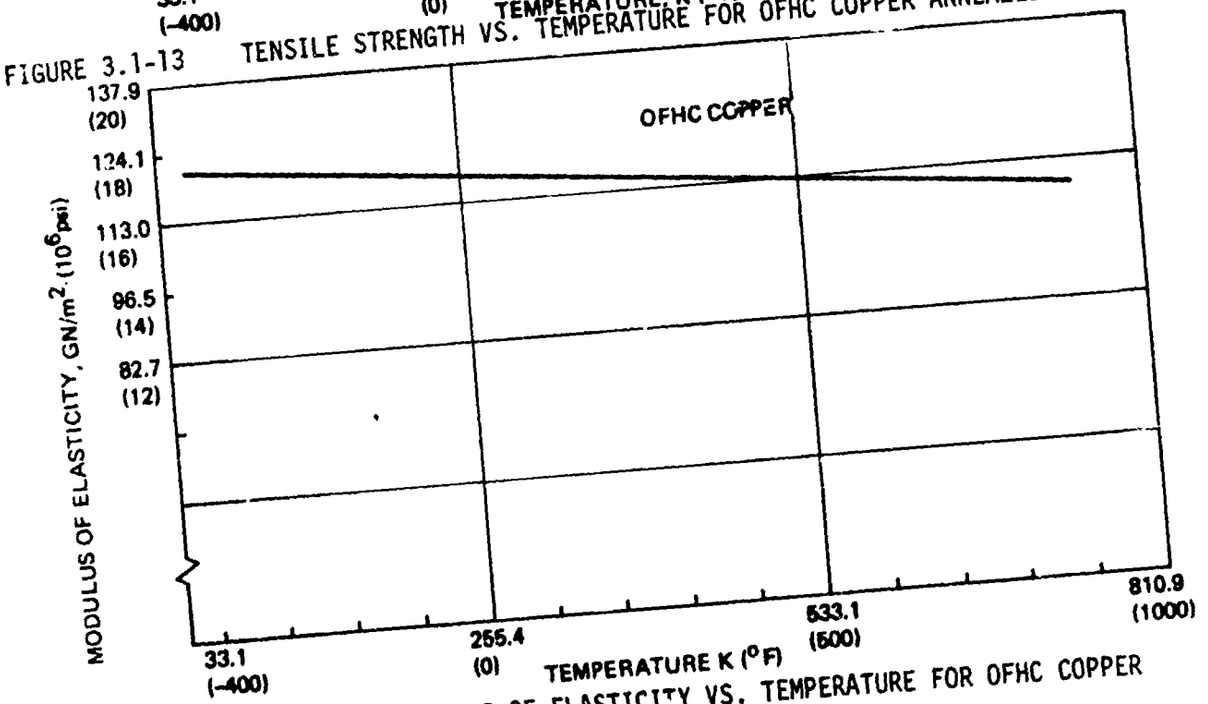

FIGURE 3.1-14 MODULUS OF ELASTICITY VS. TEMPERATURE FOR OFHC COPPER

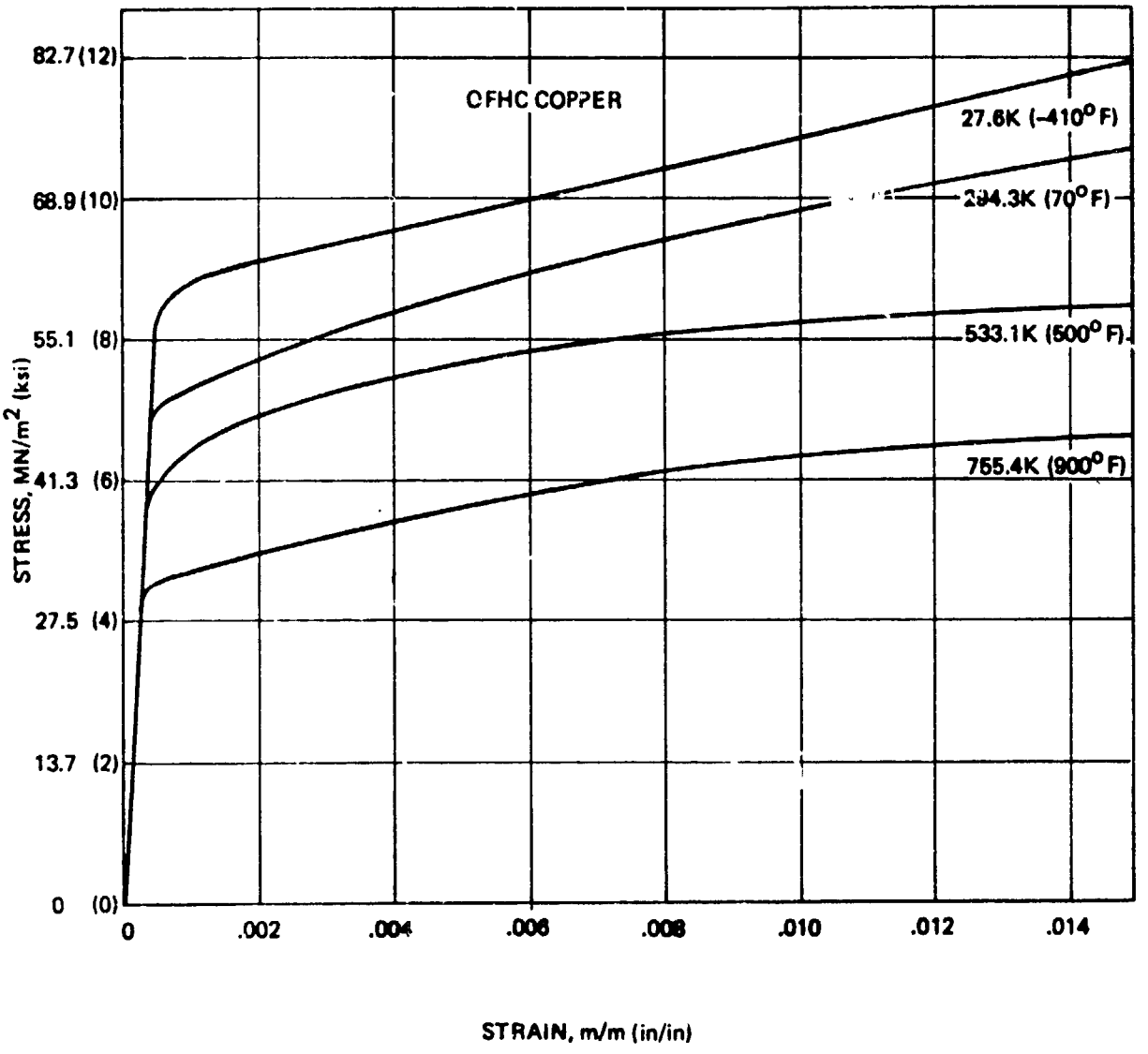

FIGURE 3.1-15 TYPICAL STRESS-STRAIN CURVES FOR OFHC COPPER ANNEALED CONDITION

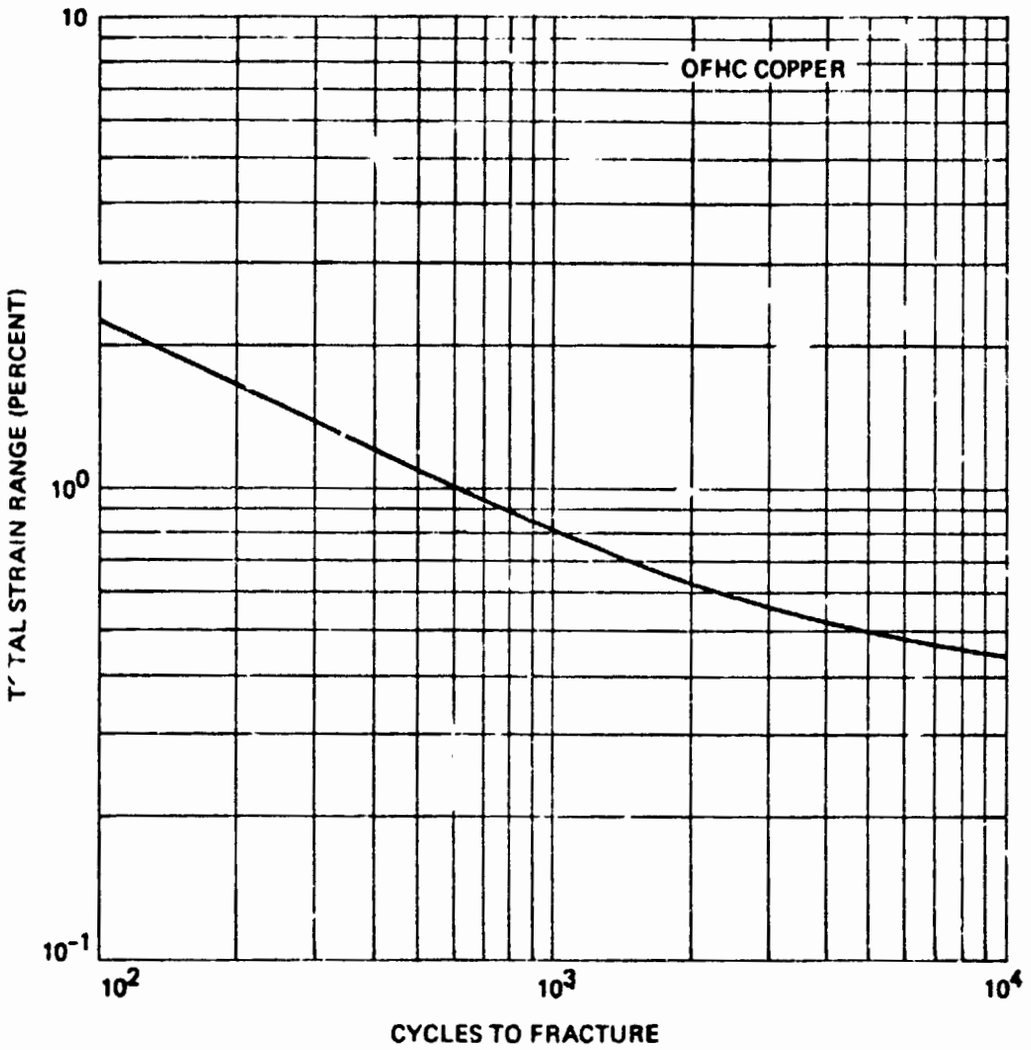

FIGURE 3.1-16 TYPICAL LOW-CYCLE FATIGUE LIFE OF OFHC COPPER ANNEALED CONDITION

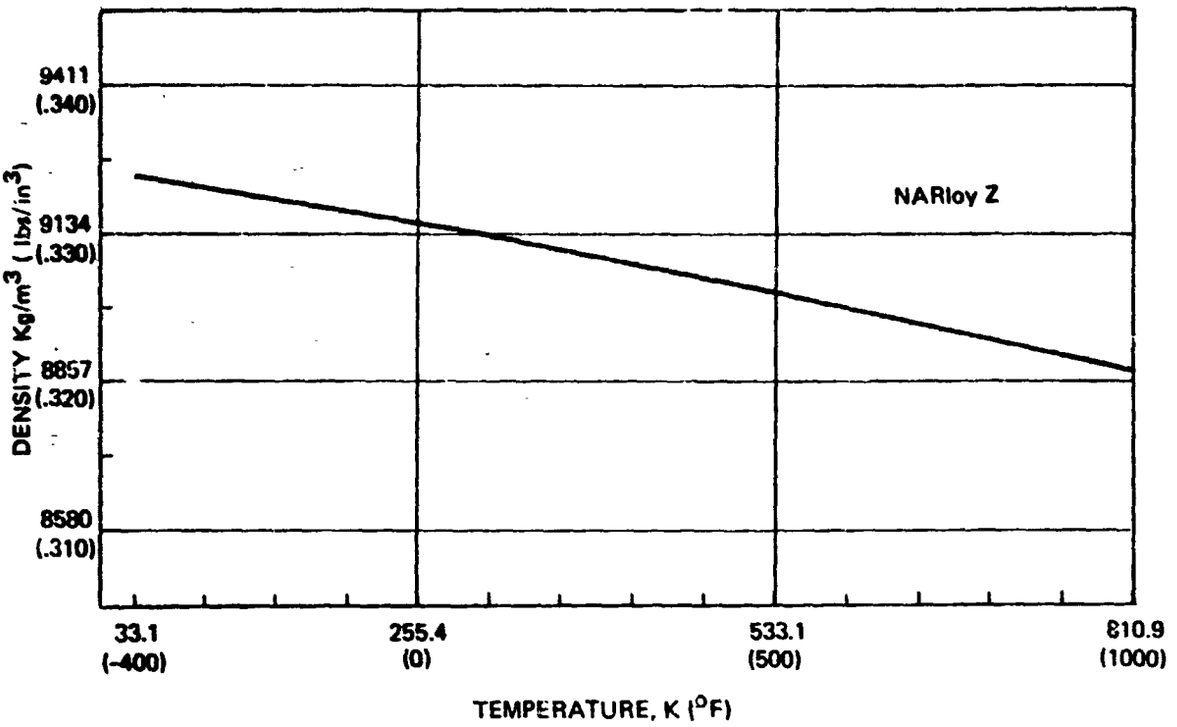

FIGURE 3.1-17 DENSITY VS. TEMPERATURE FOR NARloy Z

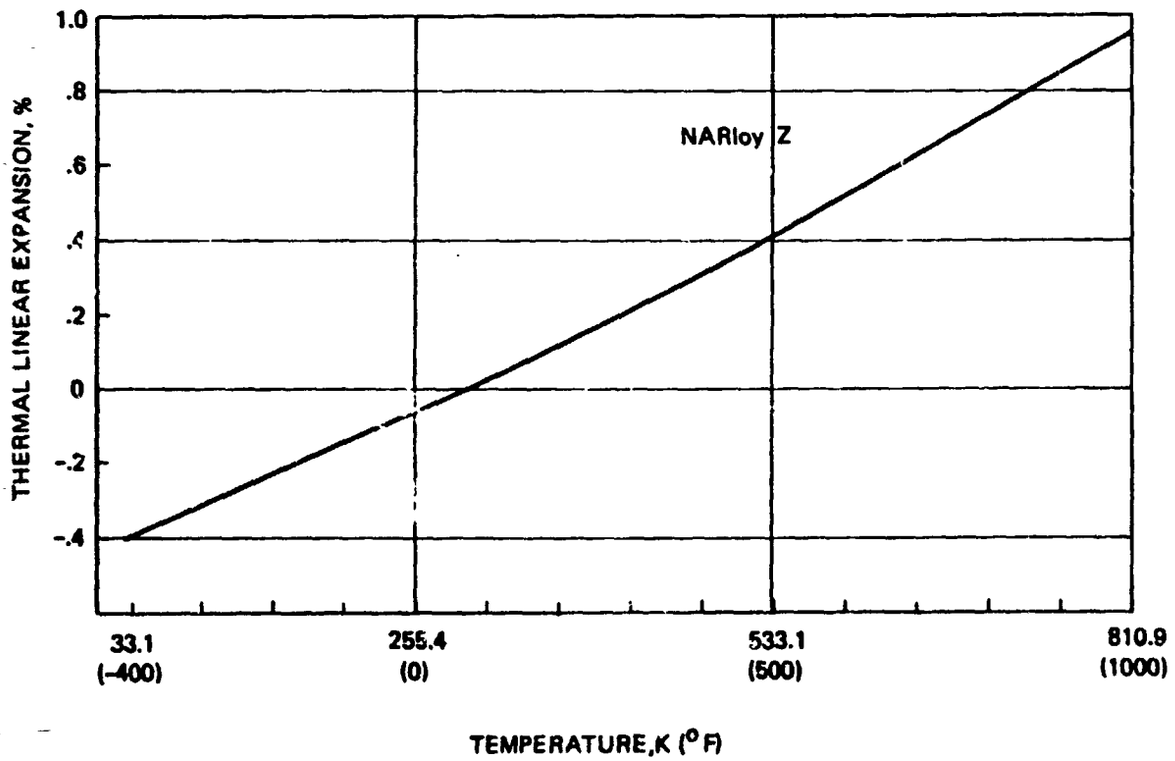

FIGURE 3.1-18 THERMAL LINEAR EXPANSION VS. TEMPERATURE FOR NARloy Z

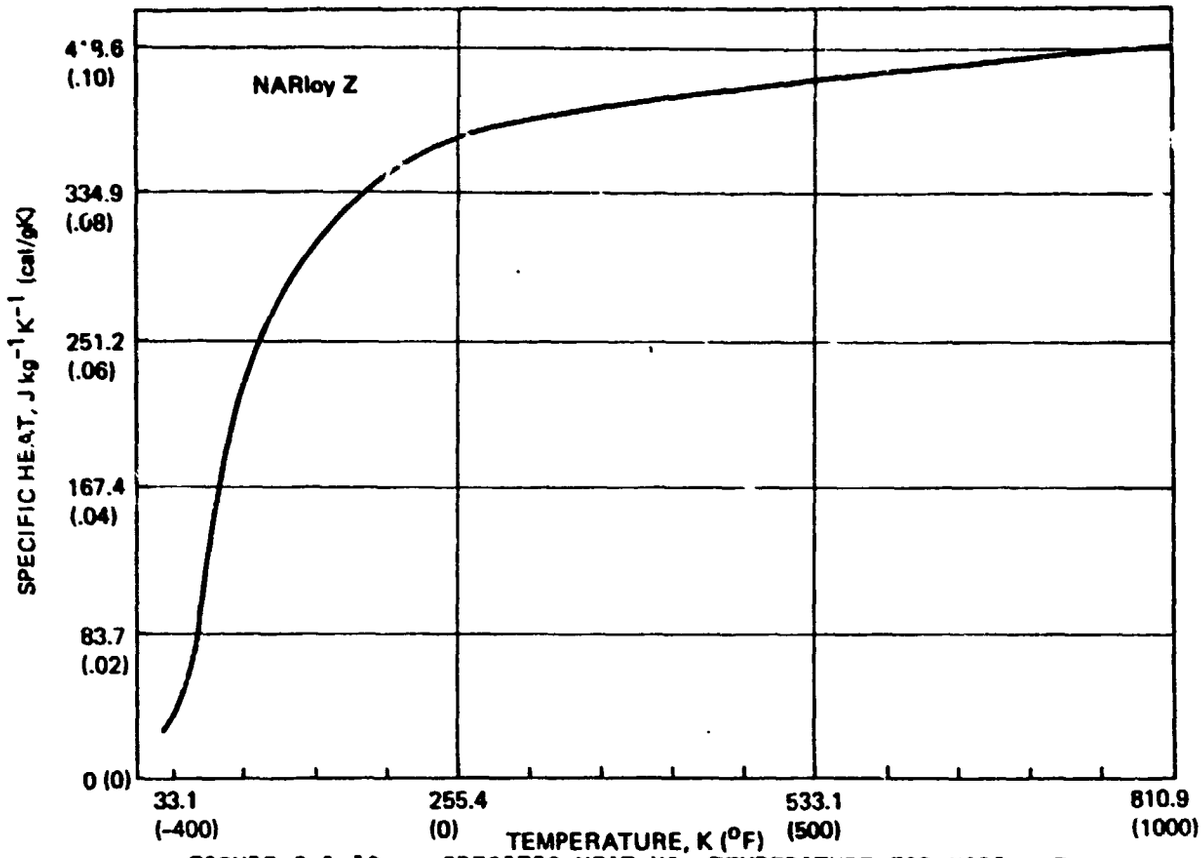

FIGURE 3.1-19 SPECIFIC HEAT VS. TEMPERATURE FOR NARloy Z

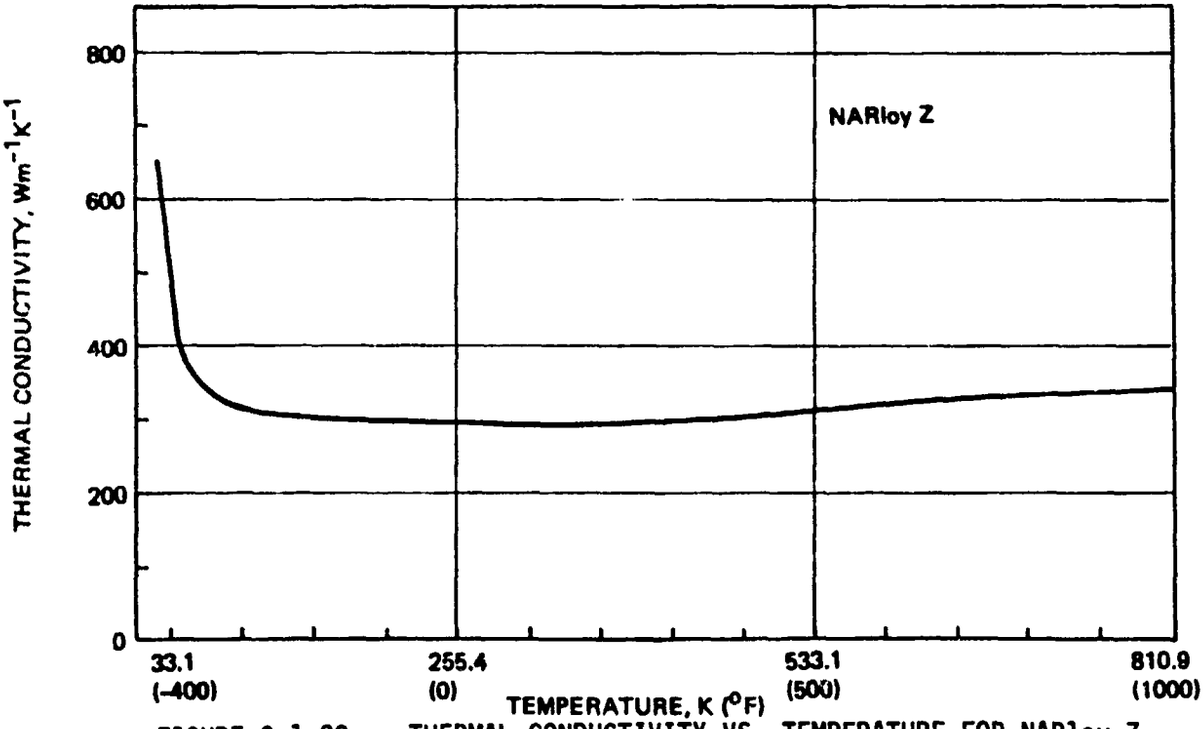

FIGURE 3.1-20 THERMAL CONDUCTIVITY VS. TEMPERATURE FOR NARloy Z

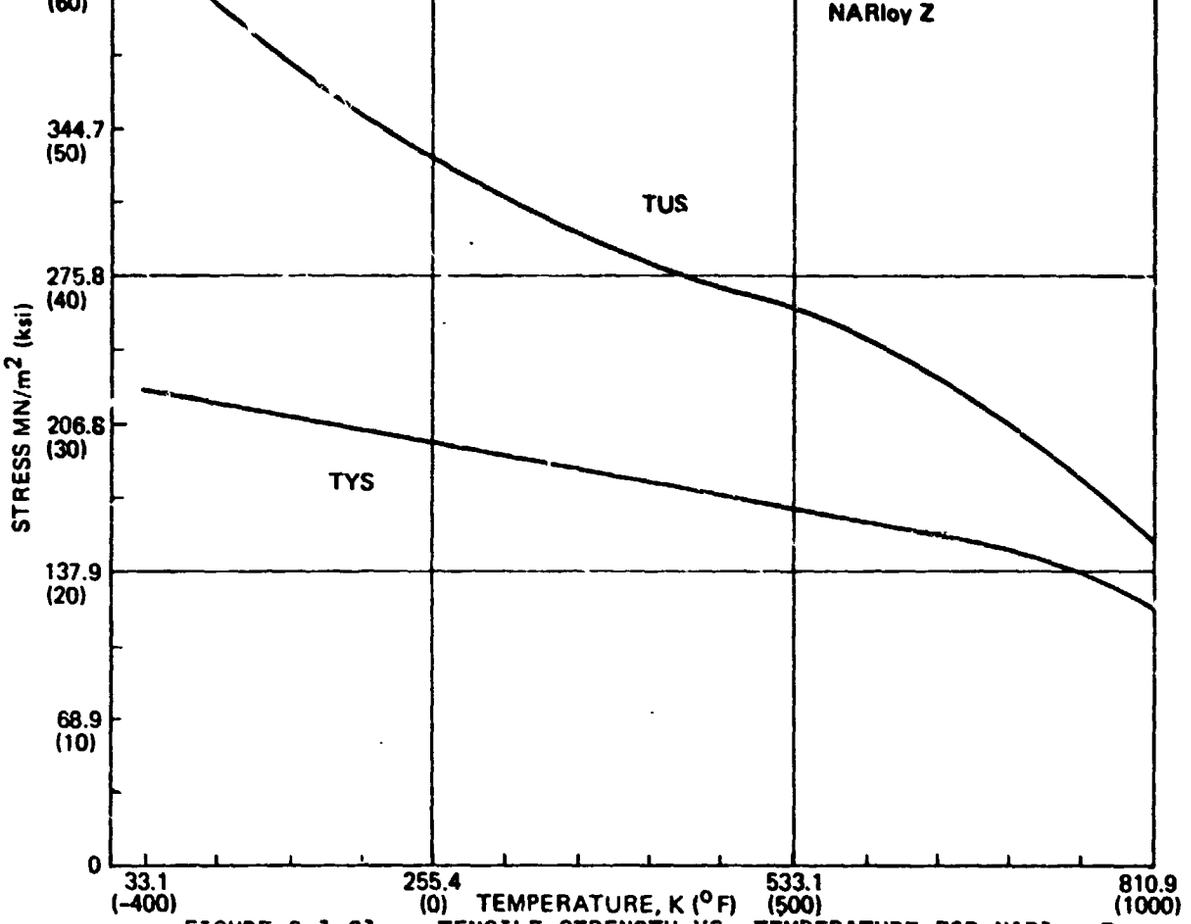

FIGURE 3.1-21 TENSILE STRENGTH VS. TEMPERATURE FOR NARloy Z

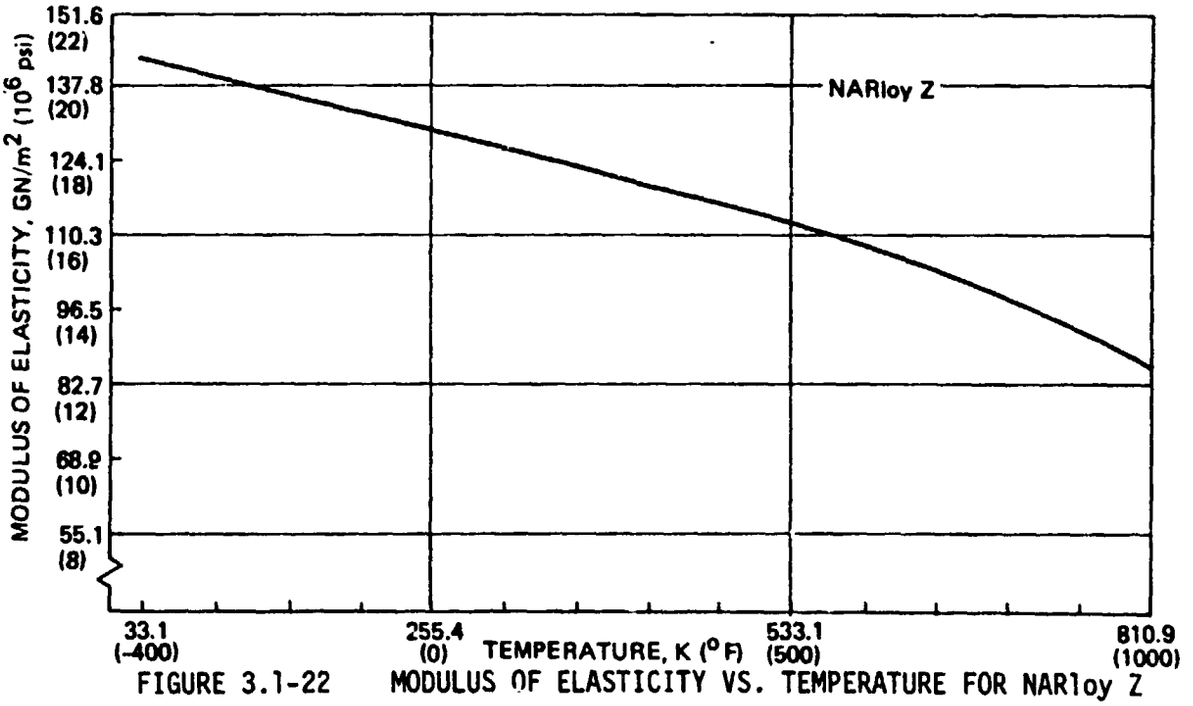

FIGURE 3.1-22 MODULUS OF ELASTICITY VS. TEMPERATURE FOR NARloy Z

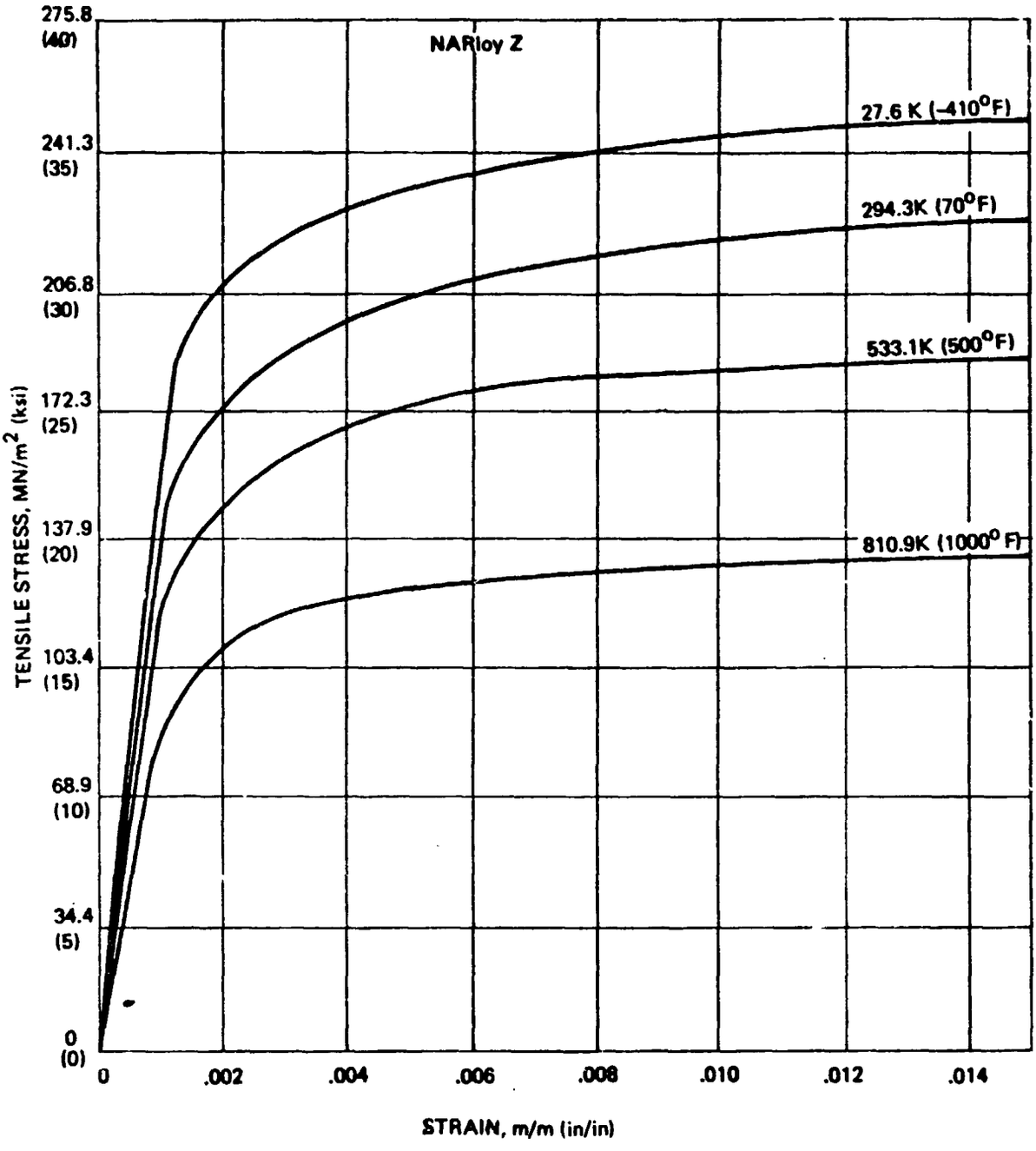

FIGURE 3.1-23 TYPICAL STRESS-STRAIN CURVES FOR NARloy Z

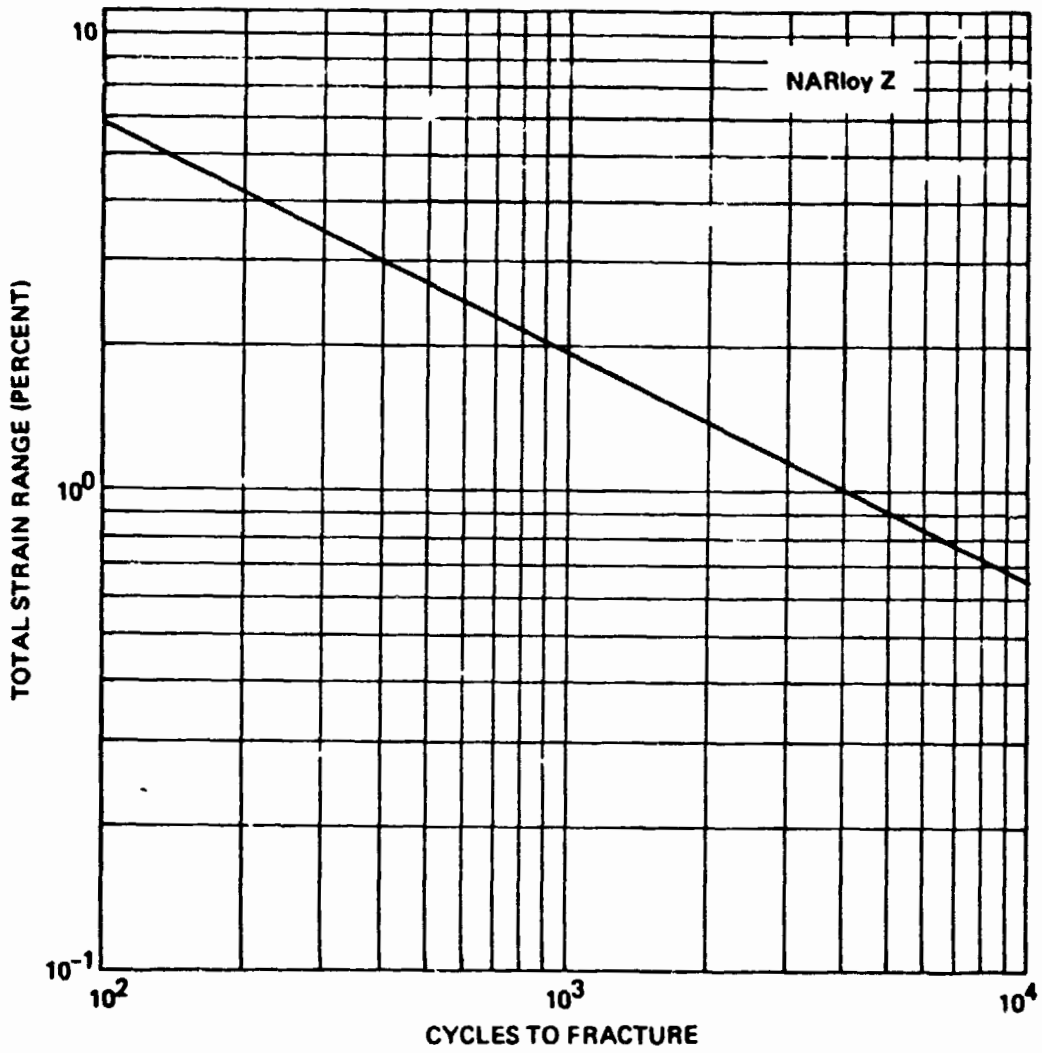

FIGURE 3.1-24 TYPICAL LOW-CYCLE FATIGUE LIFE OF NARloy Z

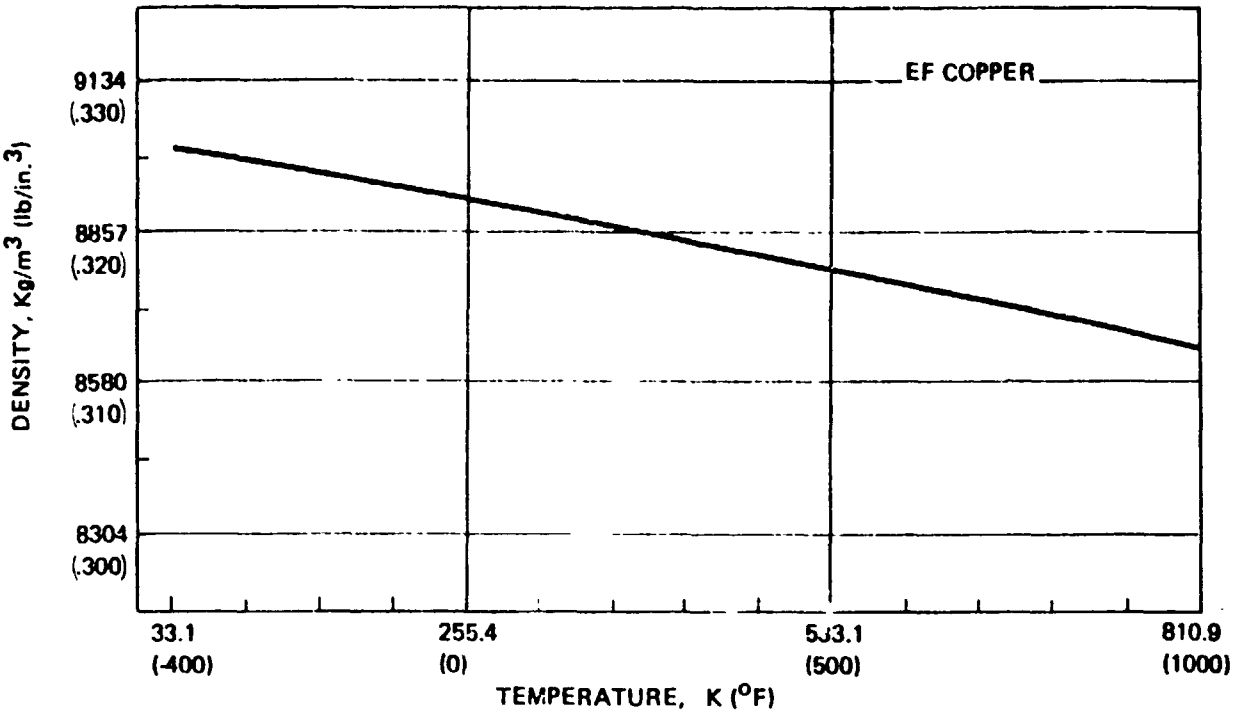

FIGURE 3.1-25 DENSITY VS. TEMPERATURE FOR ELECTROFORMED COPPER

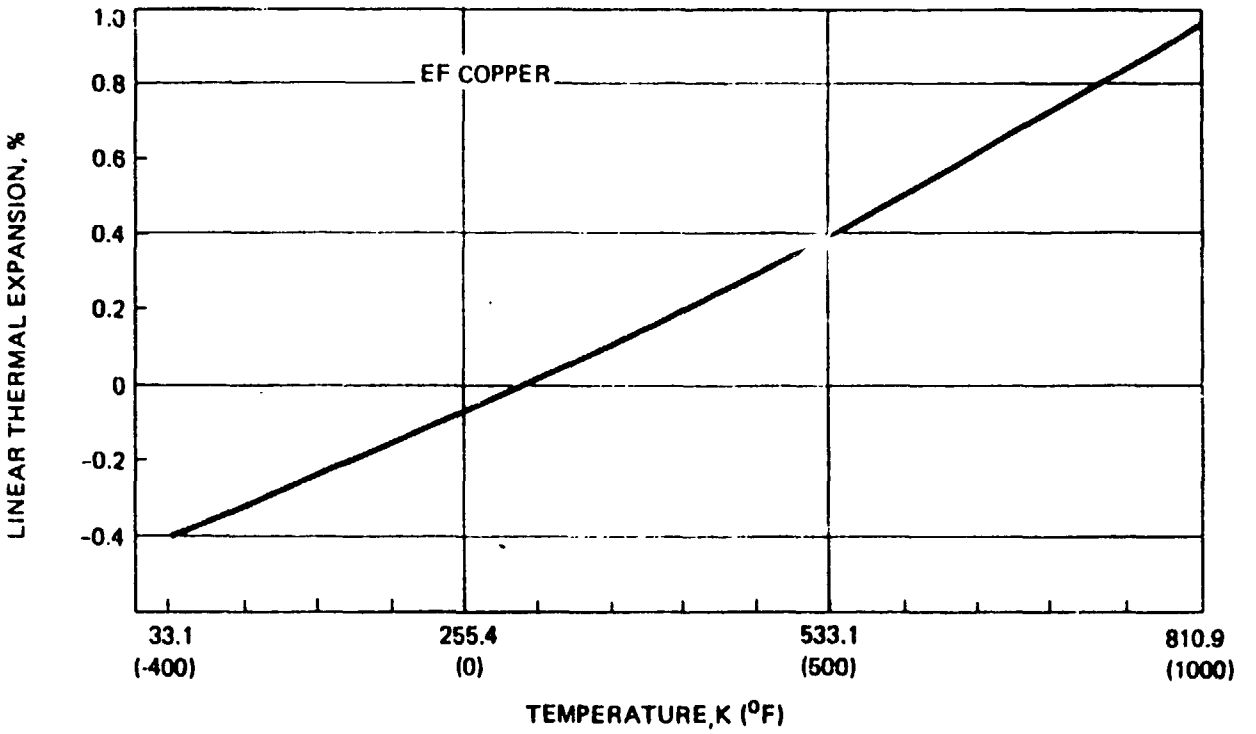

FIGURE 3.1-26 THERMAL LINEAR EXPANSION VS. TEMPERATURE FOR ELECTROFORMED COPPER

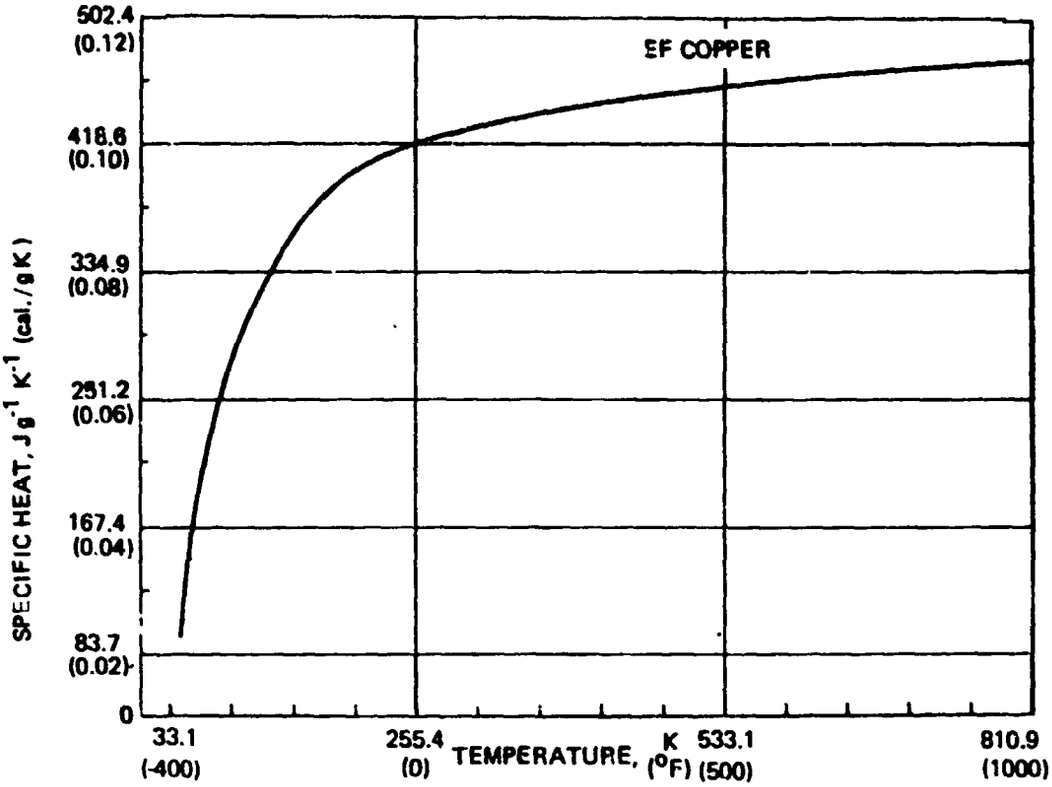

FIGURE 3.1-27 SPECIFIC HEAT VS. TEMPERATURE FOR ELECTROFORMED COPPER

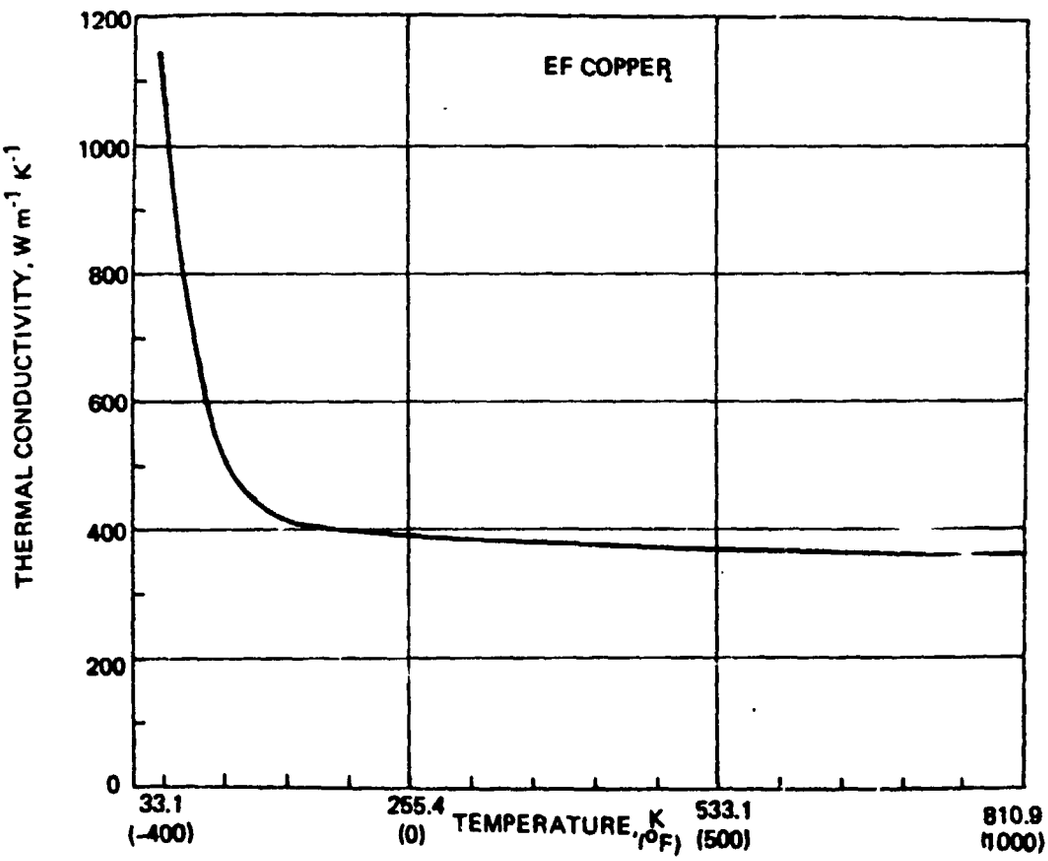

FIGURE 3.1-28 THERMAL CONDUCTIVITY VS. TEMPERATURE FOR ELECTROFORMED COPPER

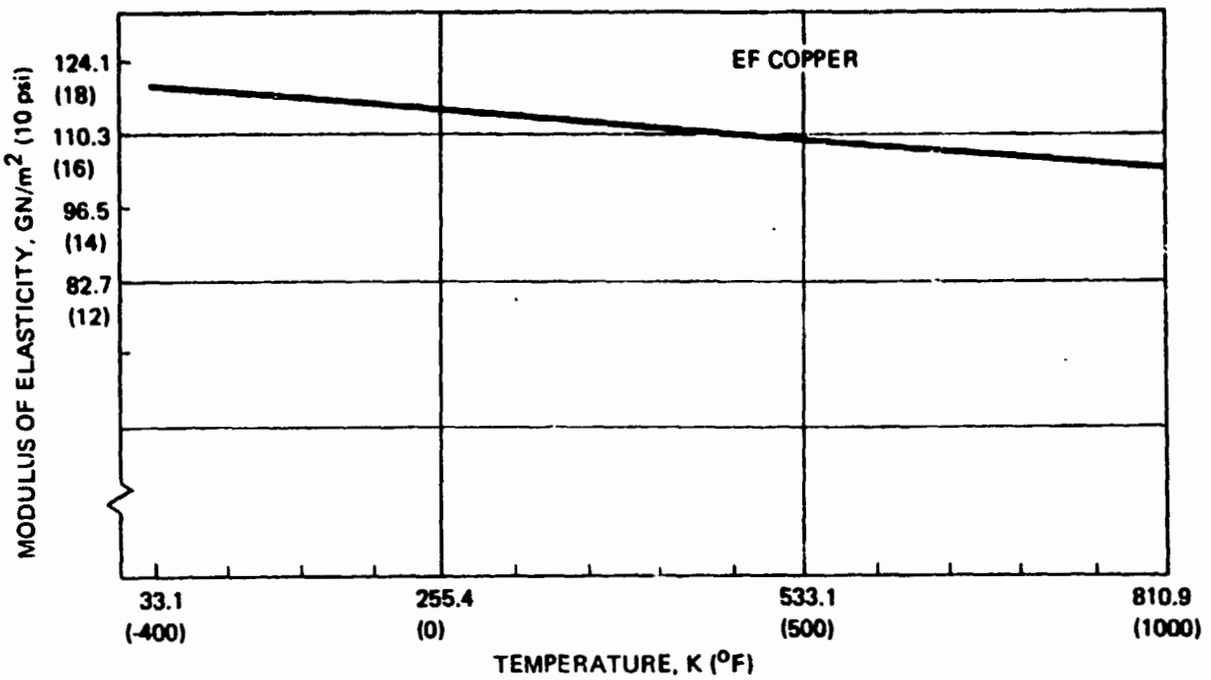

FIGURE 3.1-29 MODULUS OF ELASTICITY VS. TEMPERATURE FOR ELECTROFORMED COPPER

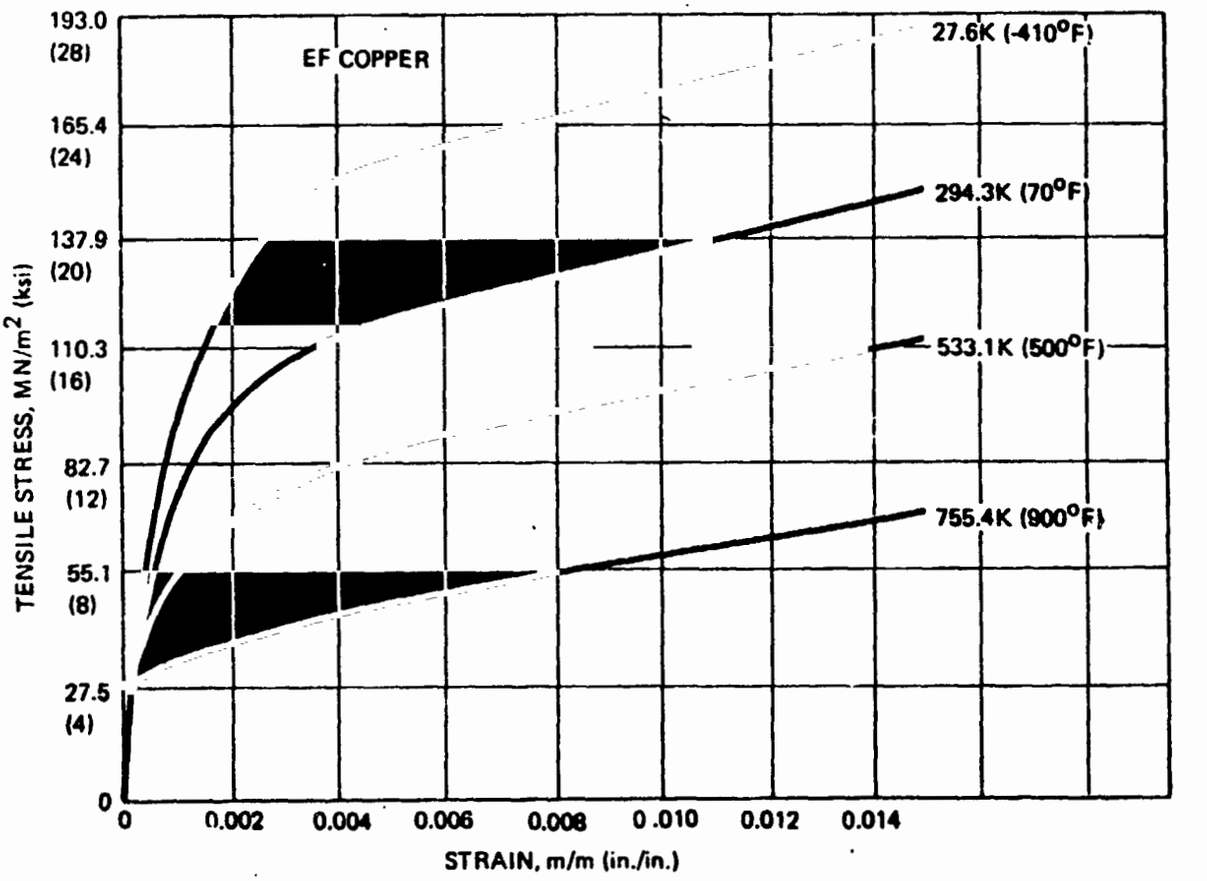

FIGURE 3.1-30 TYPICAL STRESS-STRAIN CURVES FOR ELECTROFORMED COPPER - AS FORMED CONDITION

TABLE 3.2-Ia BOUNDARY CONDITIONS

STATION	Z (cm) (SEE FIG. 4.1-1)	h_G (kW/m^2-K)		h_C (kW/m^2-K)		T_{Gaw} (K)		T_C (K)		P_G (MN/m^2)		P_C (MN/m^2)	
		HEATING	COOLING	HEATING	COOLING	HEATING	COOLING	HEATING	COOLING	HEATING	COOLING	HEATING	COOLING
1	0	6.42	0.0	97.2	102	3351	278	59	28	4.05	.0965	5.57	4.28
2	1.052	10.12	0.0	76.2	102	3342	278	56	28	3.77	.0965	5.99	4.80
3	1.651	15.78	0.0	58.6	102	3327	278	54	28	3.38	.0965	6.25	4.95
4	2.159	19.63	0.0	49.1	102	3308	278	51	28	2.95	.0965	6.49	5.01
5	2.540	20.75	0.0	47.4	102	3289	278	49	28	2.56	.0965	6.65	5.17
6	2.921	19.51	0.0	47.4	102	3267	278	46	28	2.17	.0965	6.80	5.26
7	3.282	17.22	0.0	50.0	102	3243	278	44	28	1.80	.0965	6.92	5.34
8	3.810	13.90	0.0	58.6	102	3214	278	41	28	1.45	.0965	7.06	5.47
9	4.572	10.68	0.0	75.0	102	3185	278	38	28	1.16	.0965	7.22	5.66
AXIAL AVERAGE		14.21	0.0	63.9	102	3287	278	49	28	2.71	.0965	6.49	5.07
2-D (REF. 3)		20.16	0.0	48.3	102	3364	278	50	28	2.78	.0965	6.55	5.10

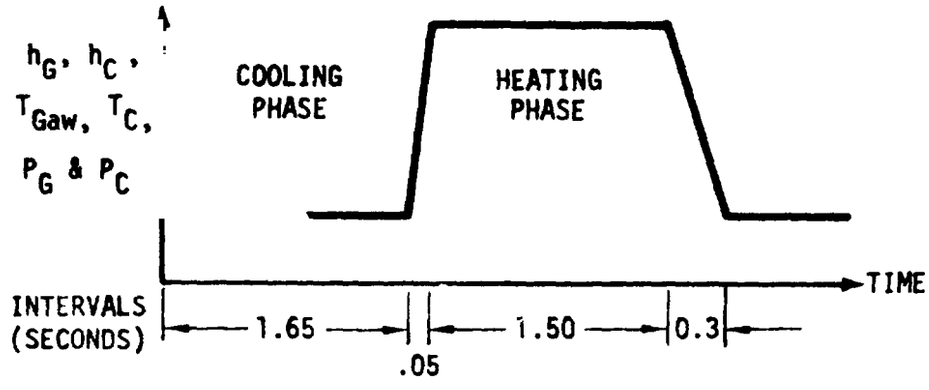

h_G = HOT GAS SIDE HEAT TRANSFER COEFFICIENT

h_C = COOLANT SIDE HEAT TRANSFER COEFFICIENT

T_{Gaw} HOT GAS SIDE ADIABATIC WALL TEMPERATURE

T_C = COOLANT SIDE BULK TEMPERATURE

P_G = HOT GAS SIDE STATIC WALL PRESSURE

P_C = COOLANT SIDE STATIC WALL PRESSURE

TABLE 3.2-Ib BOUNDARY CONDITIONS

STATION	Z (in) (SEE FIG. 4.1-1)	h_G (BTU/in^2-sec-°R)		h_C (BTU/in^2-sec-°R)		T_{Gaw} (°R)		T_C (°R)		P_G (lb/in^2)		P_C (lb/in^2)	
		HEATING	COOLING	HEATING	COOLING	HEATING	COOLING	HEATING	COOLING	HEATING	COOLING	HEATING	COOLING
1	0	.00218	0.0	.0330	.0345	6032	500	106	50	587	14	808	621
2	0.414	.00344	0.0	.0259	.0345	6015	500	101	50	547	14	869	697
3	0.65	.00536	0.0	.0199	.0345	5989	500	97	50	491	14	907	718
4	0.85	.00667	0.0	.0167	.0345	5955	500	92	50	428	14	941	727
5	1.00	.00705	0.0	.0161	.0345	5921	500	88	50	372	14	965	750
6	1.15	.00663	0.0	.0161	.0345	5881	500	83	50	315	14	987	763
7	1.292	.00585	0.0	.0170	.0345	5837	500	80	50	261	14	1004	775
8	1.50	.00472	0.0	.0199	.0345	5785	500	74	50	210	14	1024	794
9	1.80	.00363	0.0	.0255	.0345	5733	500	68	50	168	14	1047	821
AXIAL AVERAGE		.00483	0.0	.0217	.0345	5916	500	89	50	393	14	941	735
2-D (REF. 3)		.00685	0.0	.0164	.0345	6055	500	90	50	403	14	950	740

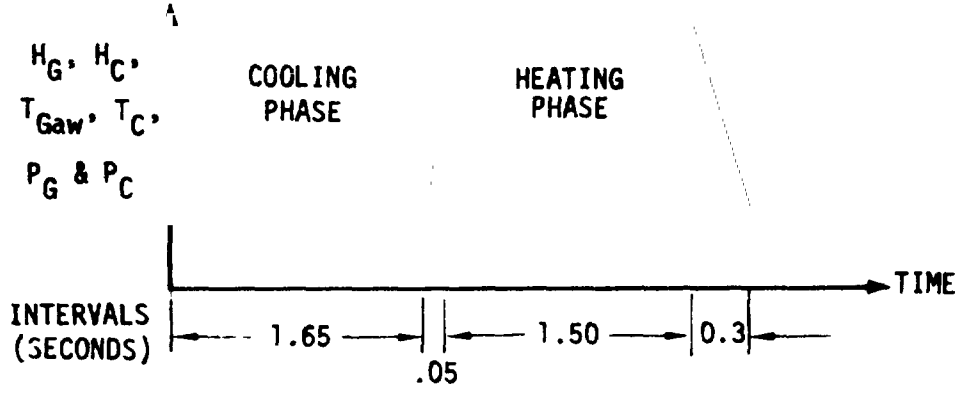

h_G = HOT GAS SIDE HEAT TRANSFER COEFFICIENT

h_C = COOLANT SIDE HEAT TRANSFER COEFFICIENT

T_{Gaw} = HOT GAS SIDE ADIABATIC WALL TEMPERATURE

T_C = COOLANT SIDE BULK TEMPERATURE

P_G = HOT GAS SIDE STATIC WALL PRESSURE

P_C = COOLANT SIDE STATIC WALL PRESSURE

4.0 THERMAL ANALYSIS

The thermal analyses were carried out using the Boeing Engineering Thermal Analyzer (BETA) program. The BETA program is a large capacity digital program for computing transient or steady state heat flow in two or three dimensions. The program performs numerical solutions of the thermal diffusion equations, accounting for solid conduction, thermal capacitance, radiation interchange, convection, and internally produced or absorbed heat, as required. Variation of material properties with temperature or any other variable can be accounted for and a wide variety of boundary conditions can be accommodated.

Execution of the thermal analysis required a set of thermal boundary conditions, defined in Section 3.2, an analytical model, to be described in a following section, and a set of initial temperatures to facilitate starting the computations. In the laboratory tests of the plug nozzle engine the cyclic firings are preceded by an initial chill-down at conditions equivalent to the cooling phase of operation. Thermal and strain analyses of Reference 2 indicated that response of the thrust chamber to the initial chilldown had no significant contribution to subsequent strain accumulation or engine life. It was concluded that a simple linear variation of temperatures from initial room temperature to a uniform chilled condition at the coolant bulk temperature provided an adequate estimate of initial chilldown thermal response. It was also found in the work of References 2 and 3 and confirmed in the present analyses that the cooling phase of engine operation was of adequate duration for the chamber to return to a uniform condition at the coolant bulk temperature on each cycle. Thus it was seen that each cooling-heating cycle produced the same temperature response and that thermal analysis of a single cycle accurately represented any cycle during the life of a thrust chamber.

4.1 THERMAL ANALYSIS MODELS

The 3-D thermal analysis model is illustrated in Figure 4.1-1. The properties of symmetry were exploited in order to treat the smallest representative segment of the chamber, thus maximizing the practical modeling detail and resulting analysis accuracy. Thermal nodes (locations where thermal capacitance and convecting surface areas were assumed concentrated) were positioned at each intersection of line segments of the figure. The line segments represent thermal connectors (paths of thermal conductance between nodes). Nodes and connectors representing driving (boundary) temperatures and convective conductors, respectively, were also part of the model but are not shown in the illustration. Exact locations and the identifying number system for model body nodes are shown in Figure 4.1-2. In the analyses, temperatures were evaluated for each node at preselected time intervals.

The analytical model represents a compromise between accuracy of predicted temperatures and economical use of computer time. A very fine nodal mesh can produce detailed and accurate results but generally requires excessive machine time. This was the case in the thrust chamber model where the very high thermal diffusivity of the materials and small element sizes demanded very small time steps to avoid computational instabilities.

The validity of the selected 3-D model was checked by comparing results of a 2-D analysis of the 43-node throat plane section (Station 5) of the 3-D mesh of Configuration B.1 with the temperature results for the 136-node 2-D model of the same cylinder presented in Reference 3. The conditions used in these two analyses were the 2-D boundary conditions of Table 3.2-1. A sample of the comparison is shown in Figure 4.1-3. The agreement between corresponding nodal temperatures was considered satisfactory to support the adoption of the 3-D model. Actually, perfect agreement was not expected from such a comparison, since although the corresponding nodes are located identically, they do not represent equal regions. Nodal temperatures must be interpreted

4.1 (Continued)

as average temperatures for the area or volume of the elements defined by the nodes and thus, in general, will differ for different element dimensions.

An earlier 189-node 3-D model, with a 21-node throat plane section, did not yield satisfactory agreement with detailed 2-D model results. Another model, with 567 total nodes and 63 section nodes, required an impractical amount of computer time.

The selected 3-D thermal model was further checked by performing a full 3-D analysis with axially-constant boundary conditions equal to the 2-D values for configuration B.1. Results in which temperature distributions at each cross section exactly duplicated those from the 2-D analysis of the 43 node mesh were taken as verification of correctly input nodal and connector properties.

4.2 THERMAL ANALYSIS RESULTS

The working output data from the thermal analyses were recorded on tape directly from the computer executing the BETA program. From this tape, cards were automatically punched for input into the interpolater program which evaluated temperatures at the times and locations required for the structural analyses. A complete print-out of BETA data was generated and used to monitor output but was considered too voluminous to reproduce in this report. Samples of the thermal analysis results are presented in order to illustrate the magnitudes of the temperatures and the character of the temperature distributions computed.

Figures 4.2-1 and 4.2-2 show histories of temperatures at selected throat plane nodes for Configurations B.1 and B.2 and Configuration B.3, respectively. The origin of the time scale, i.e., time = 0.0, on these plots and on subsequent plots of thermal data is the beginning of the cooling phase, consistent with the diagram accompanying Table 3.2-I.

4.2 (Continued)

The NARloy-Z inner wall of Configuration B.3 has lower thermal conductivity than the Amzirc or OFHC copper used for Configurations B.1 and B.2. The effects of this difference in conductivity can be seen in comparing the curves of Figure 4.2-1 and 4.2-2, wherein the lower conductivity (Figure 4.2-2) causes temperatures to be higher in high temperature regions and lower in low temperature regions of Configuration B.3.

Figures 4.2-3 through 4.2-8 show axial variations of temperature at selected points in the high temperature region for both configurations. Times selected for these plots were near the beginning of the heating phase (1.8 sec.), the end of the heating phase (3.2 sec), and the end of the heating-to-cooling transient (3.5 sec.). (The above times correspond respectively to 0.15, 1.55, and 1.85 seconds after engine start for each operating cycle). Maximum axial temperatures were found to occur very near the throat plane for all locations and times. Maximum axial gradients occurred at roughly one-fourth of the chamber length from each end. The lack of axial gradients at the ends of the chambers is consistent with the assumption of adiabatic boundaries at those planes.

4.3 COMPARISON OF 2-D AND 3-D THERMAL ANALYSIS

One form of comparison between characteristics of the 3-D analysis model and the previously analyzed detailed 2-D model was shown in Figure 4.1-3. That comparison was for a 2-D test case, and not for analysis results to be used for thrust chamber life predictions. It should be recognized, however, that the effects of differences in nodal model mesh size, such as those seen in Figure 4.1-3, will be present and may influence any comparisons between 2-D and 3-D thermal results derived from analyses of the represented models.

4.3 (Continued)

Figure 4.3-1 shows temperature histories for selected throat plane nodes from 3-D analysis of Configurations B.1 and B.2 and temperatures for corresponding nodes from the analysis of Reference 3. The most obvious difference between the two sets of curves is the generally lower temperatures from the 3-D analysis. This difference is regarded as largely due to the differences between the corresponding boundary conditions and was anticipated upon examination of the axial averages of the 3-D thermal boundary conditions. Aside from the difference in temperature levels, the 2-D and 3-D temperature histories show very similar characteristics, particularly in the strain-critical high temperature region.

Figure 4.3-2 shows selected temperature histories from the 3-D analysis of Configuration B.3 compared with corresponding histories from the 2-D analysis of the same configuration from Reference 2. The two sets of histories compare the same way as those in Figure 4.3-1: generally lower 3-D temperatures due to boundary condition differences and otherwise very similar characteristics.

The 3-D and 2-D analysis results were also compared by examining isotherms drawn for throat plane sections. Two such comparisons, for Configurations B.1 and B.2, at two times during the heating phase, are shown as Figures 4.3-3 and 4.3-4. The conclusions from isotherm comparisons parallel those from temperature history comparisons: lower temperatures from the 3-D analysis due to boundary condition differences but very similar temperature gradient characteristics.

The isotherm plots for the 3-D model illustrate an effect of that model's relatively coarse nodal mesh. Isotherms were located on the drawings by linear interpolation between nodal temperatures. This practice applied to the finite node spacings resulted in discontinuities in the indicated temperature gradients. This effect is most clearly seen in Figure 4.3-3 where, in the Configuration B.1, B.2 isotherm plot, a noticable difference in isotherm spacing exists between those lines immediately above the 450K isotherm and those immediately below that isotherm.

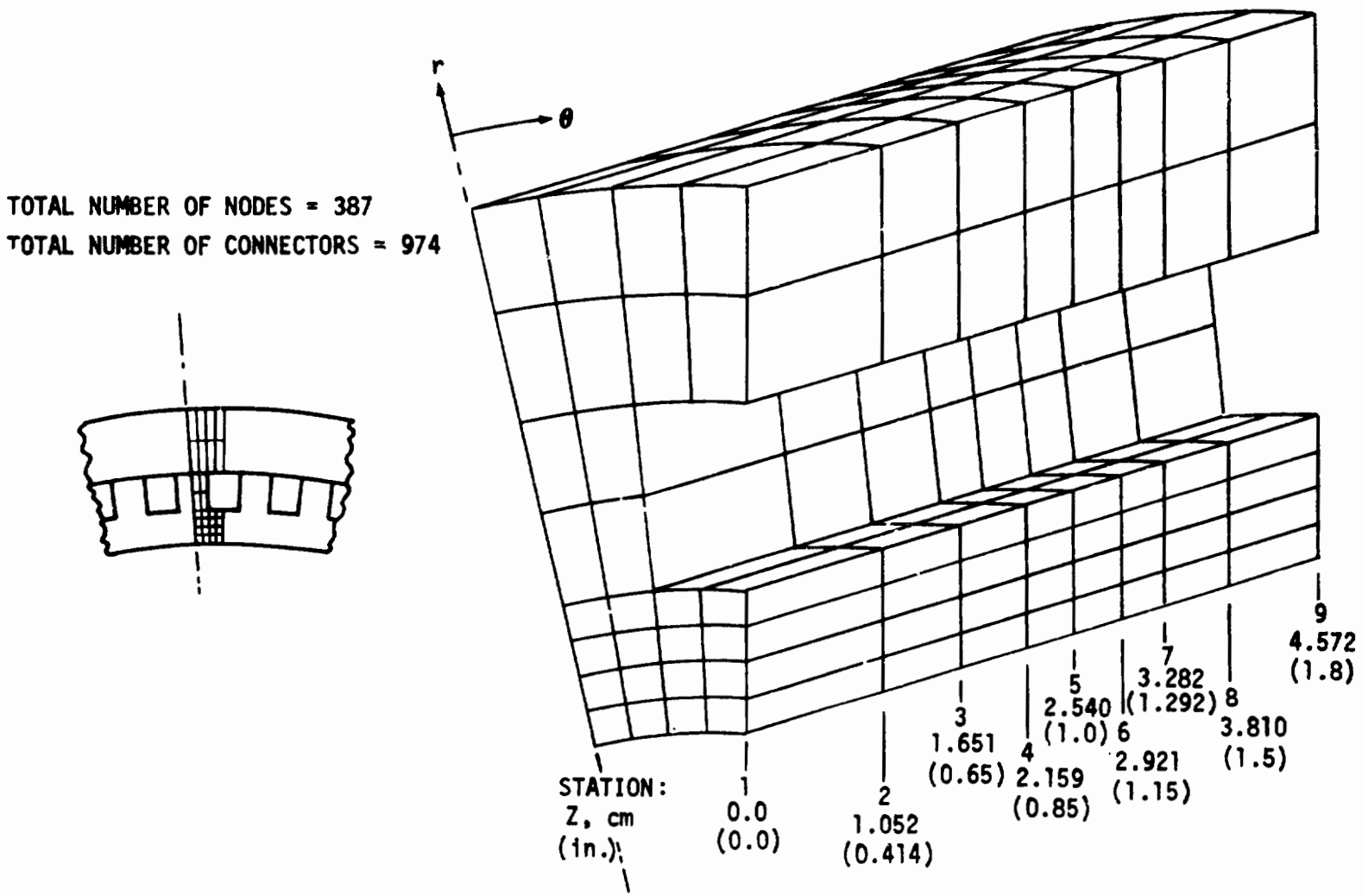

FIGURE 4.1-1 THREE-DIMENSIONAL THERMAL ANALYSIS MODEL

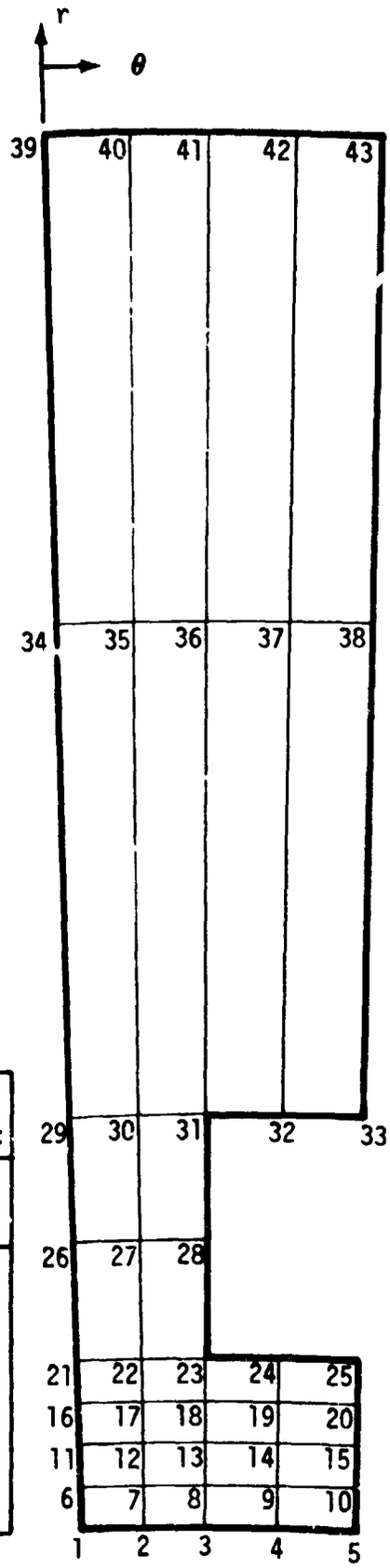

FOR OTHER AXIAL STATIONS:	
Z (cm)	NODE NUMBER
0	n + 250
1.052	n + 300
1.651	n + 350
2.159	n + 400
2.540	n
2.921	n + 50
3.282	n + 100
3.810	n + 150
4.572	n + 200

NODE NUMBERS AND LOCATIONS FOR Z = 2.54 cm.		
NODE (n)	r (cm)	θ (mrad.)
1	3.3020	0
2	3.3020	9.460
3	3.3020	19.919
4	3.3020	31.276
5	3.3020	43.633
6	3.3242	0
7	3.3242	9.460
8	3.3242	18.919
9	3.3242	31.276
10	3.3242	43.633
11	3.3465	0
12	3.3465	9.460
13	3.3465	18.919
14	3.3465	31.276
15	3.3465	43.633
16	3.3687	0
17	3.3687	9.460
18	3.3687	18.919
19	3.3687	31.276
20	3.3687	43.633
21	3.3909	0
22	3.3909	9.460
23	3.3909	18.919
24	3.3909	31.276
25	3.3909	43.633
26	3.4544	0
27	3.4544	9.6866
28	3.4544	19.3644
29	3.5179	0
30	3.5179	9.9135
31	3.5179	19.8095
32	3.5179	31.7301
33	3.5179	43.633
34	3.7719	0
35	3.7719	9.9135
36	3.7719	19.8095
37	3.7719	31.7301
38	3.7719	43.633
39	4.0259	0
40	4.0259	9.9135
41	4.0259	19.8095
42	4.0259	31.7301
43	4.0259	43.633

FIGURE 4.1-2a THERMAL ANALYTICAL MODEL - NODE LOCATIONS

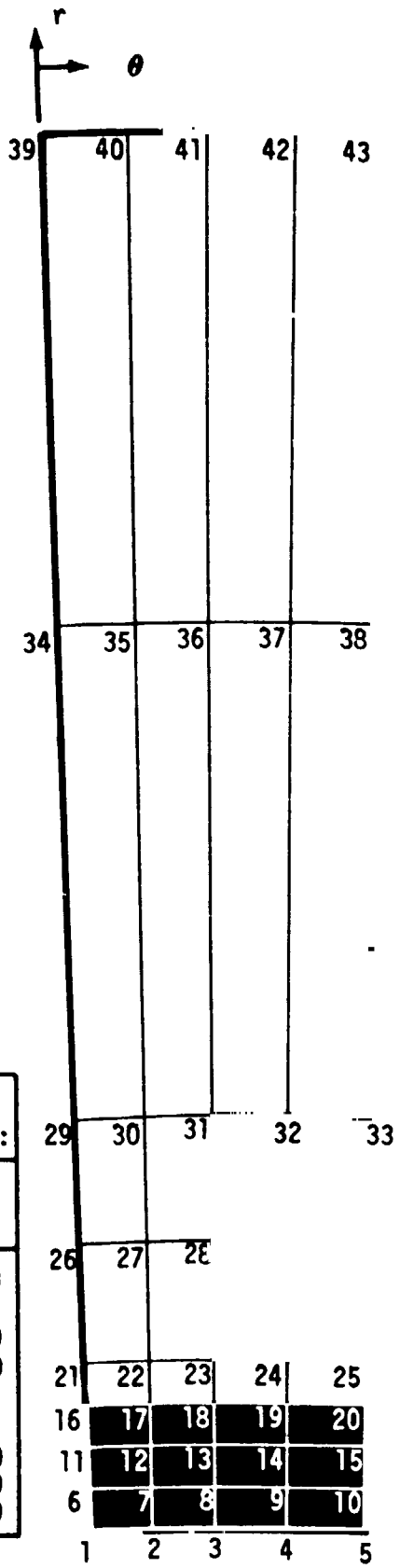

FOR OTHER AXIAL STATIONS:	
Z (in.)	NODE NUMBER
0	n + 250
0.414	n + 300
0.65	n + 350
0.85	n + 400
1.00	n
1.15	n + 50
1.292	n + 100
1.5	n + 150
1.8	n + 200

NODE NUMBERS AND LOCATIONS FOR Z = 1.0 in.		
NODE (n)	r (in.)	θ (deg.)
1	1.3000	0
2	1.3000	0.542
3	1.3000	1.084
4	1.3000	1.792
5	1.3000	2.500
6	1.3085	0
7	1.3085	0.542
8	1.3085	1.084
9	1.3085	1.792
10	1.3085	2.500
11	1.3175	0
12	1.3175	0.542
13	1.3175	1.084
14	1.3175	1.792
15	1.3175	2.500
16	1.32625	0
17	1.32625	0.542
18	1.32625	1.084
19	1.32625	1.792
20	1.32625	2.500
21	1.3350	0
22	1.3350	0.542
23	1.3350	1.084
24	1.3350	1.792
25	1.3350	2.500
26	1.3600	0
27	1.3600	0.555
28	1.3600	1.1095
29	1.3850	0
30	1.3850	0.568
31	1.3850	1.135
32	1.3850	1.818
33	1.3850	2.500
34	1.4850	0
35	1.4850	0.568
36	1.4850	1.135
37	1.4850	1.818
38	1.4850	2.500
39	1.5850	0
40	1.5850	0.568
41	1.5850	1.135
42	1.5850	1.818
43	1.5850	2.500

FIGURE 4.1-2b THERMAL ANALYTICAL MODEL - NODE LOCATIONS

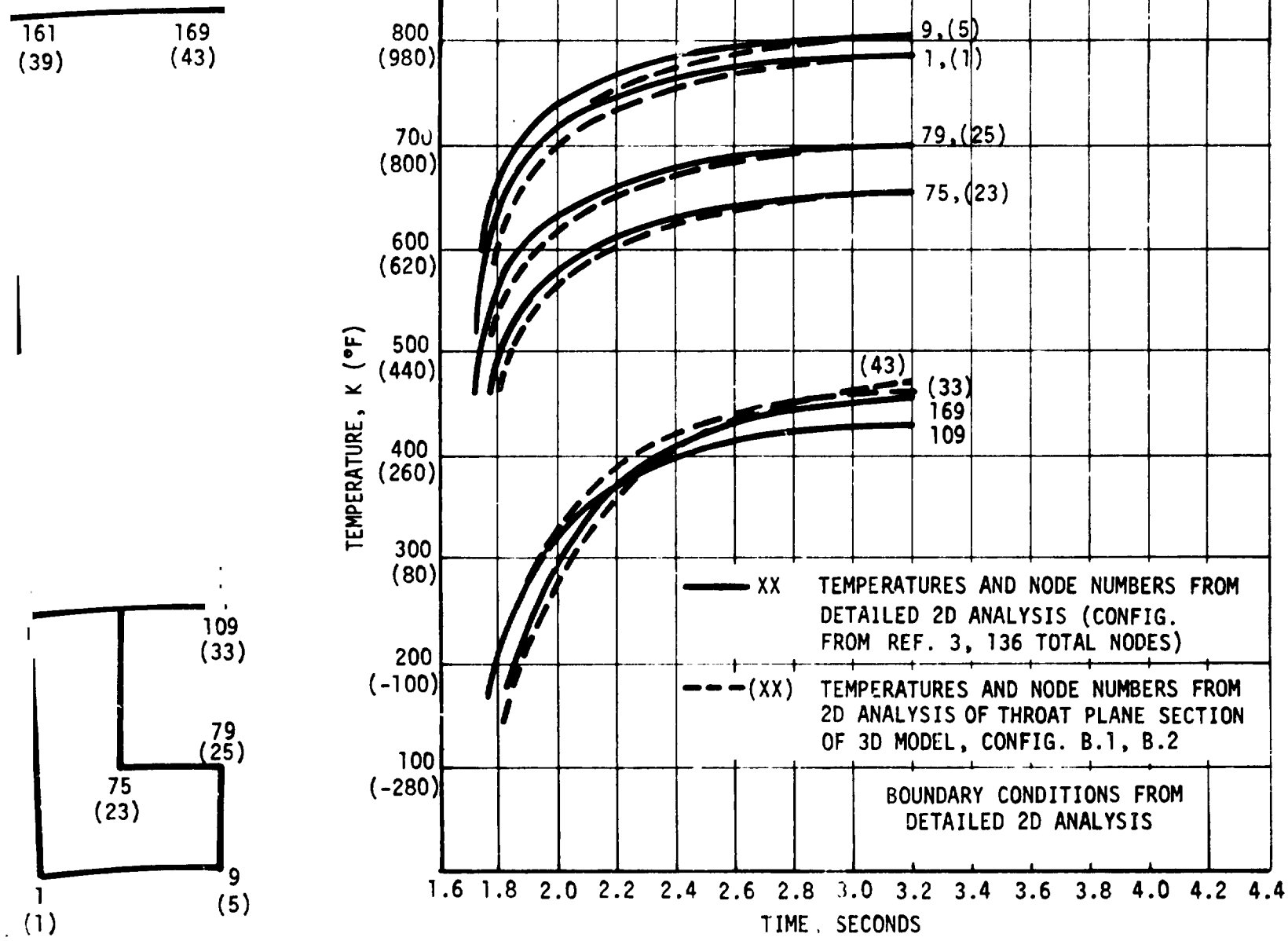

FIGURE 4.1-3 TEMPERATURE COMPARISONS - 2D SECTION THROUGH 3D MODEL VS. DETAILED 2D MODEL

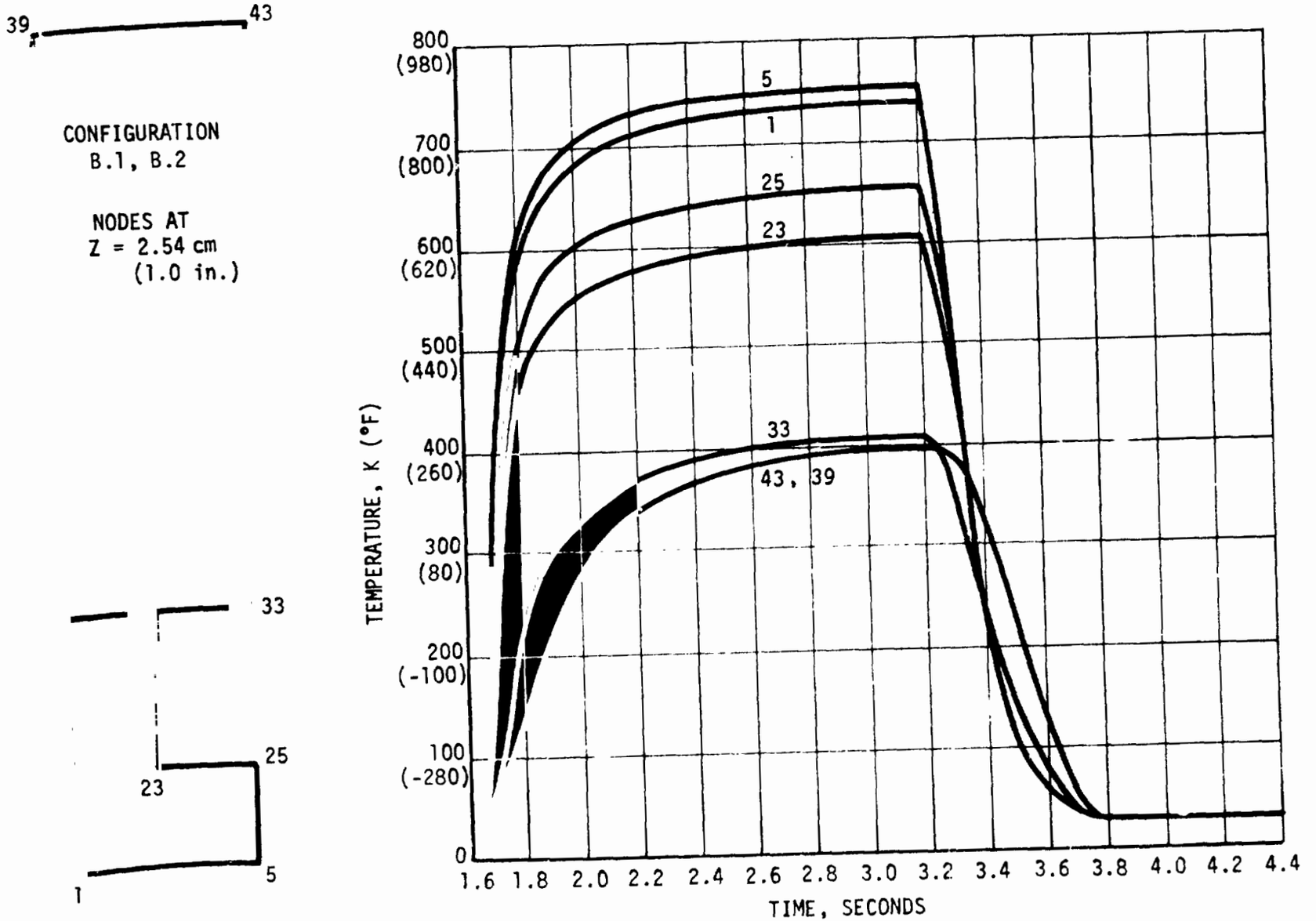

FIGURE 4.2-1 REPRESENTATIVE TEMPEATURE HISTORIES - CONFIGURATION B.1 & B.2

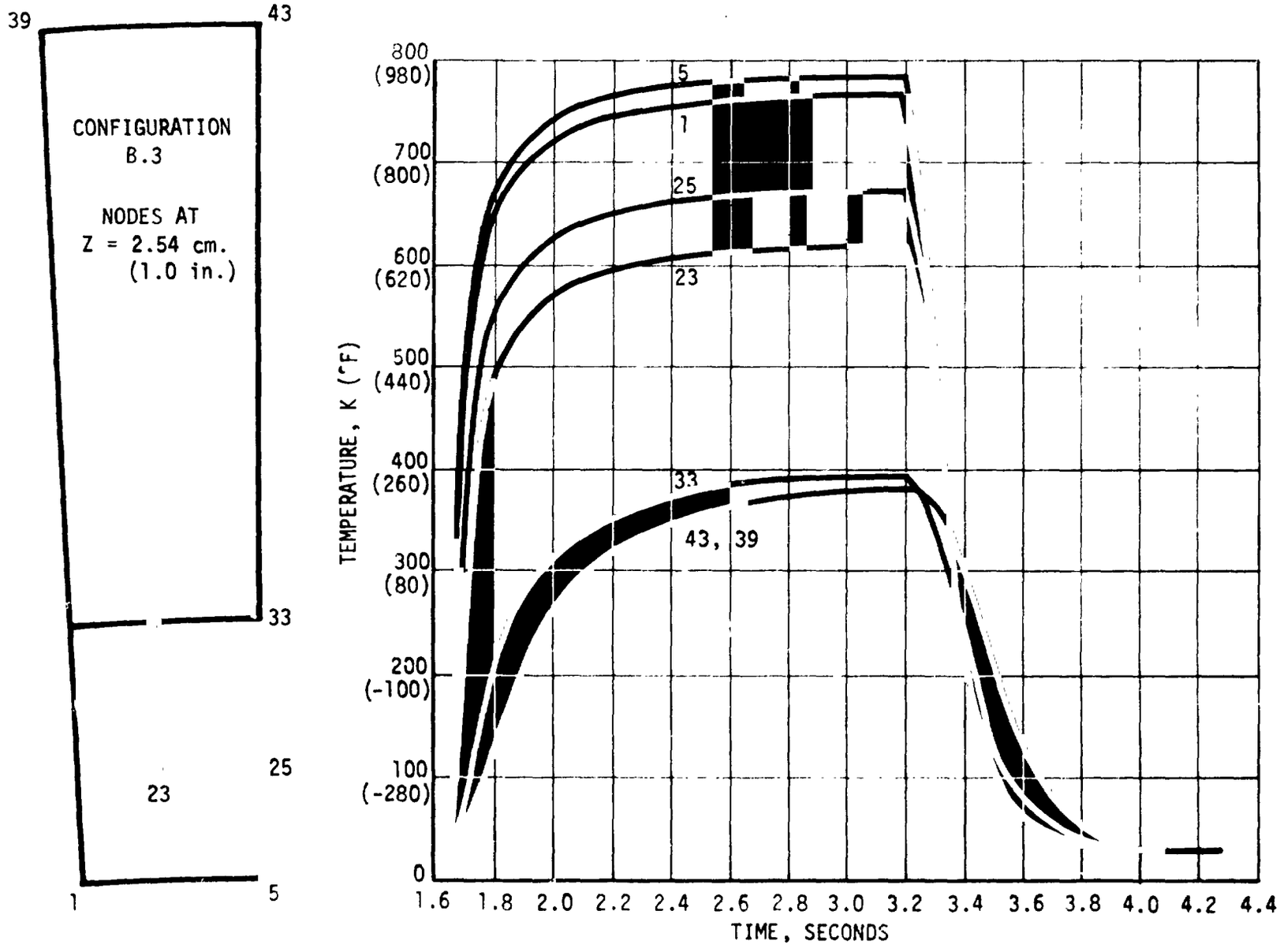

FIGURE 4.2-2 REPRESENTATIVE TEMPERATURE HISTORIES - CONFIGURATION B.3

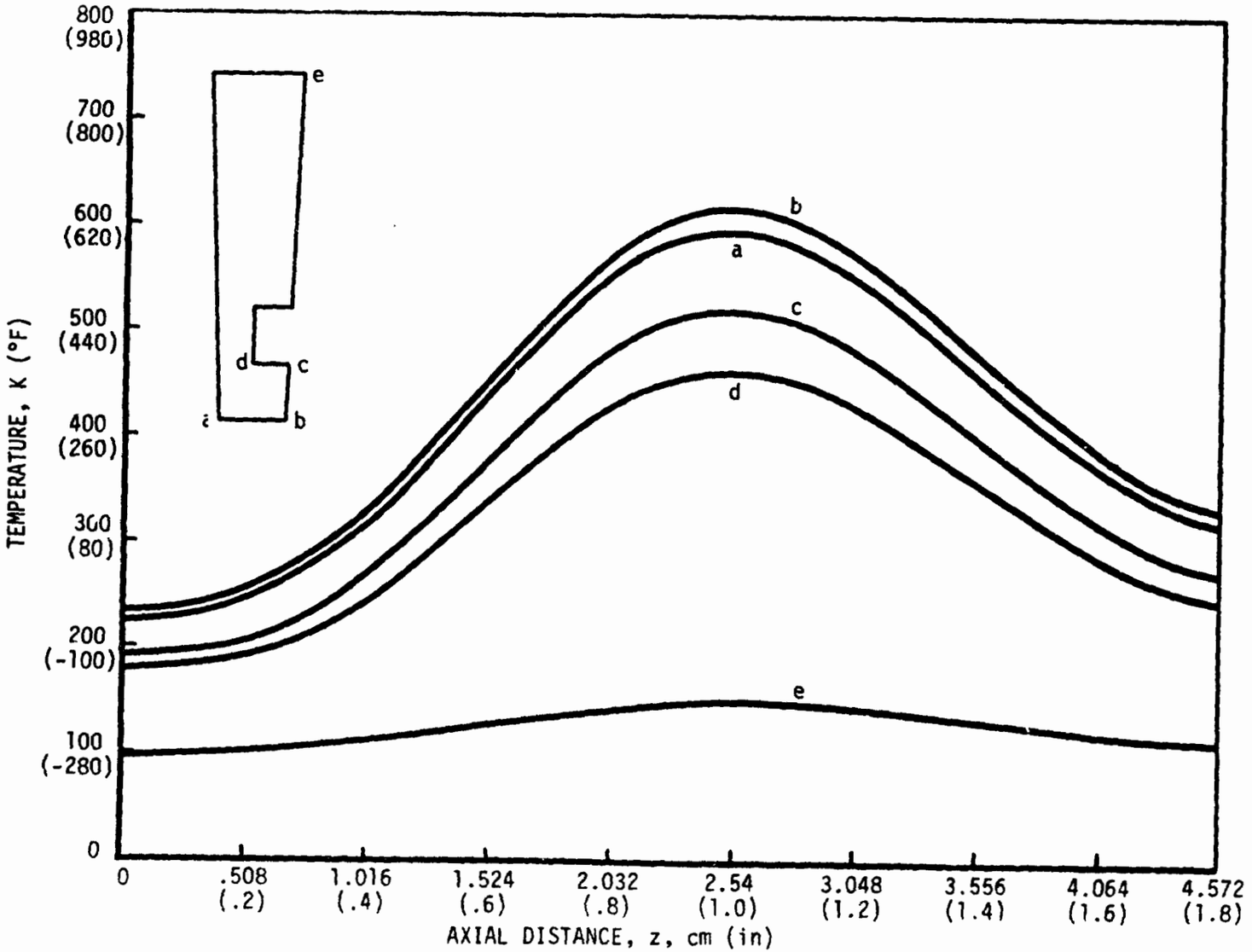

FIGURE 4.2-3 REPRESENTATIVE AXIAL TEMPERATURE DISTRIBUTIONS - CONFIGURATION B.1, B.2 AT t = 1.8 SEC

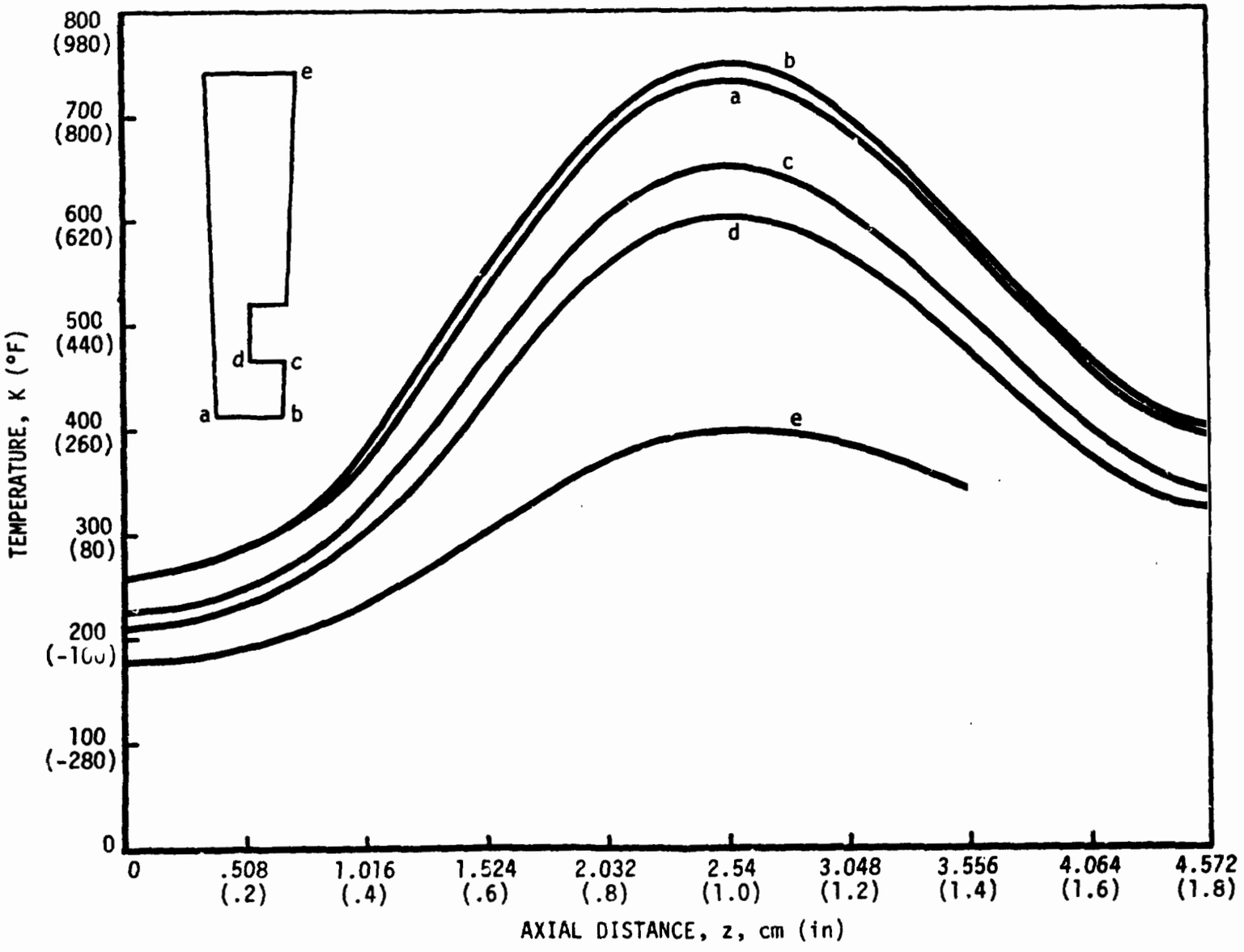

FIGURE 4.2-4 REPRESENTATIVE AXIAL TEMPERATURE DISTRIBUTIONS - CONFIGURATION B.1, B.2 AT t = 3.2 SEC

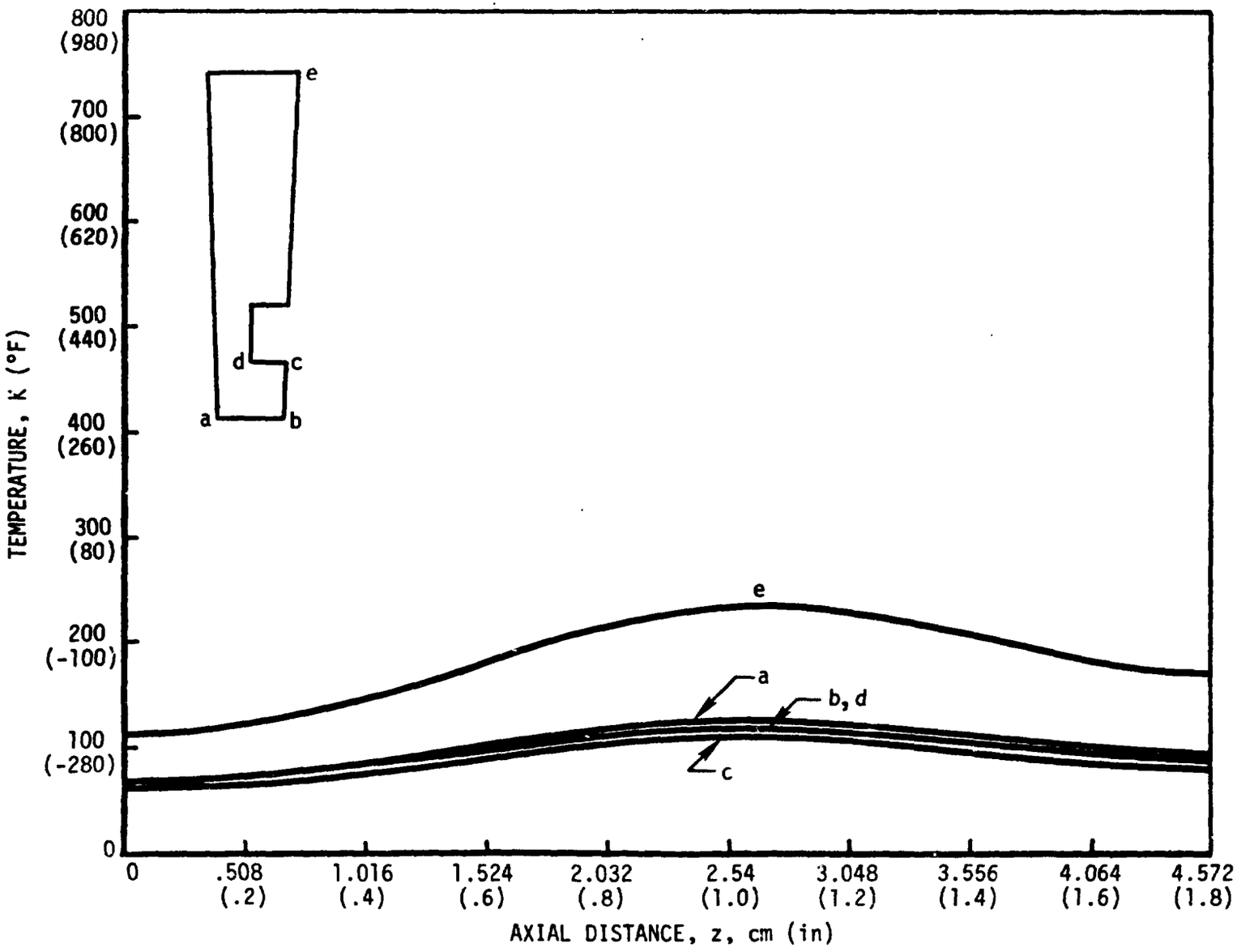

FIGURE 4.2-5 REPRESENTATIVE AXIAL TEMPERATURE DISTRIBUTIONS - CONFIGURATION B.1, B.2 AT t = 3.5 SEC

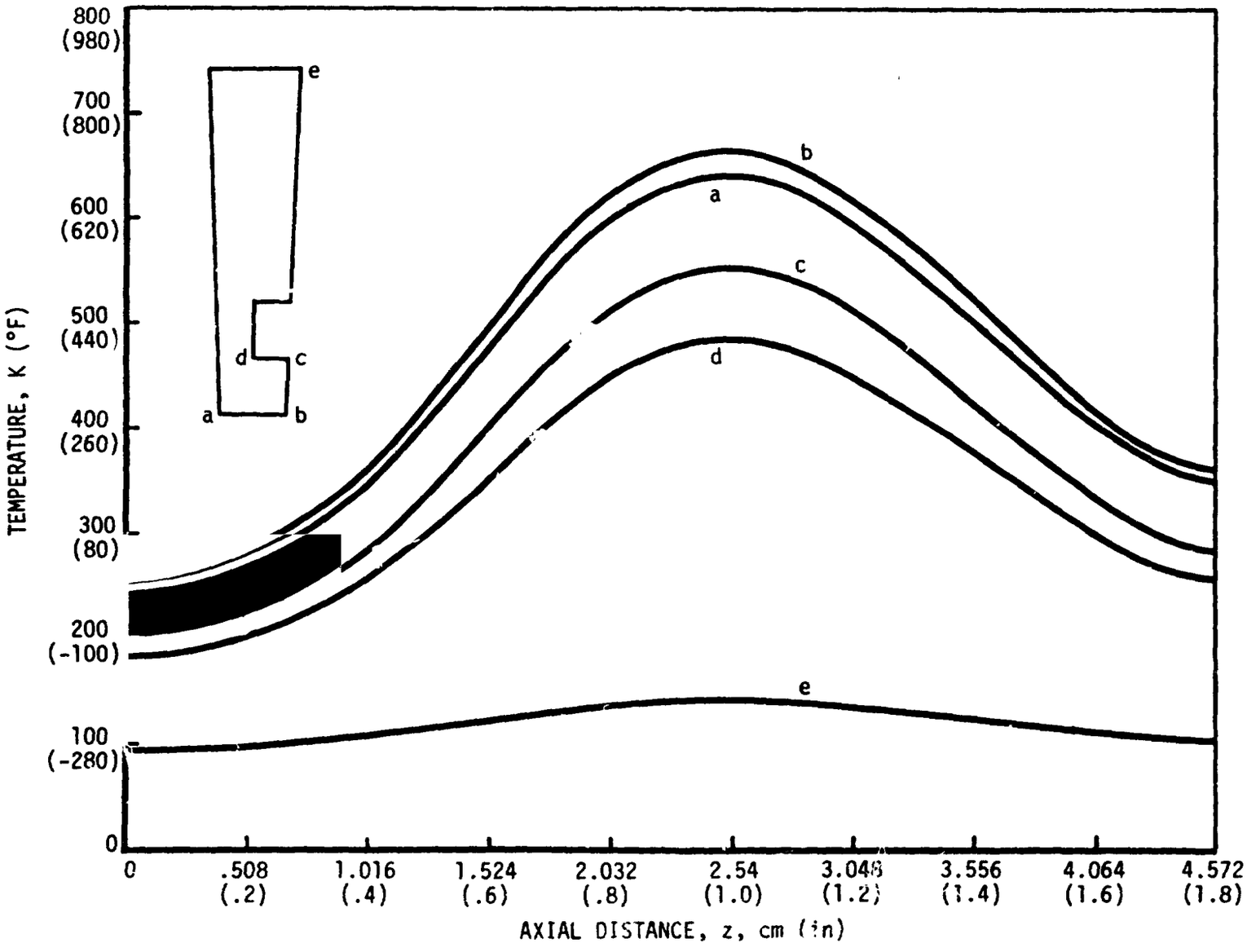

FIGURE 4.2-6 REPRESENTATIVE AXIAL TEMPERATURE DISTRIBUTIONS - CONFIGURATION B.3 AT t = 1.8 SEC

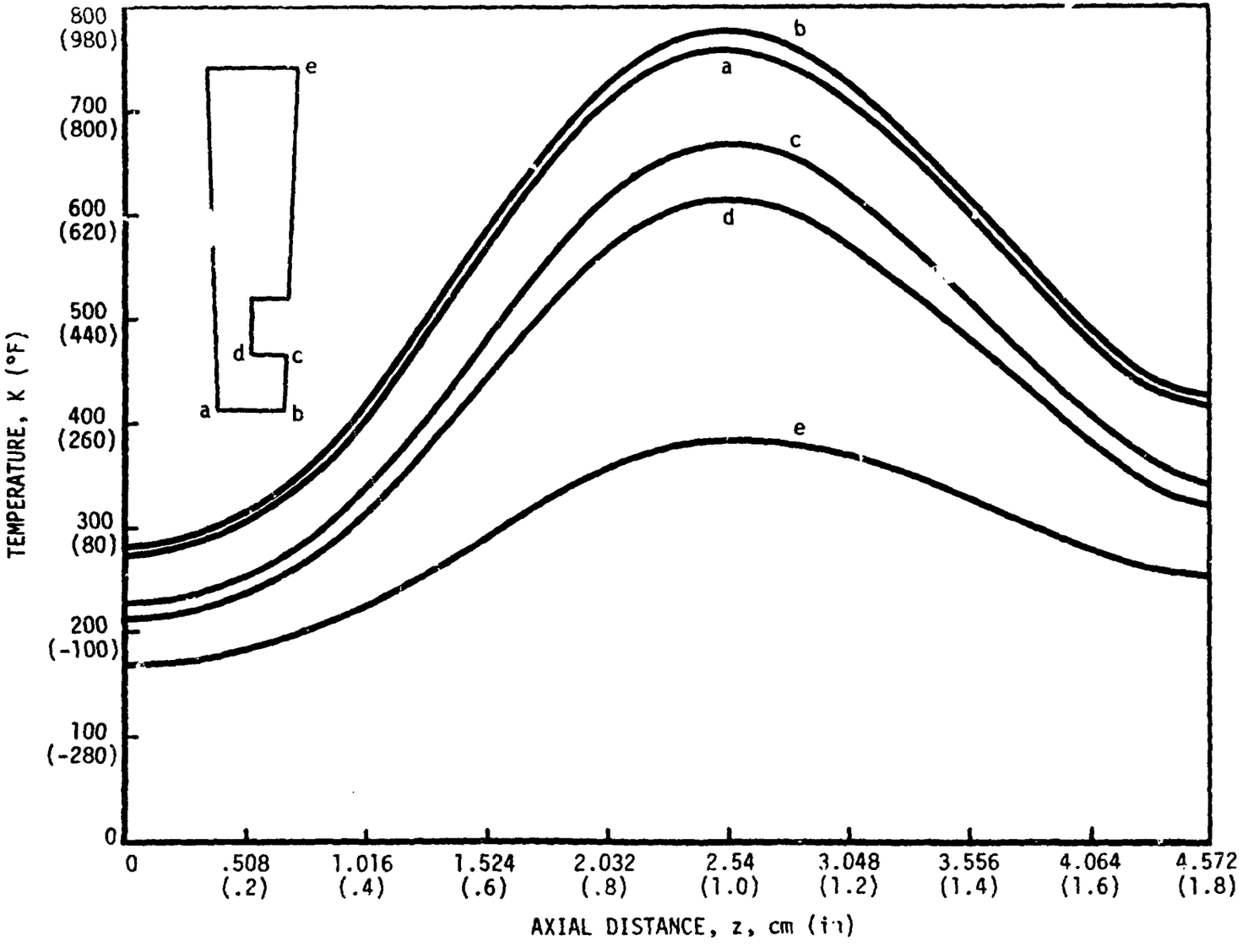

FIGURE 4.2-7 REPRESENTATIVE AXIAL TEMPERATURE DISTRIBUTIONS - CONFIGURATION B.3 AT t = 3.2 SEC

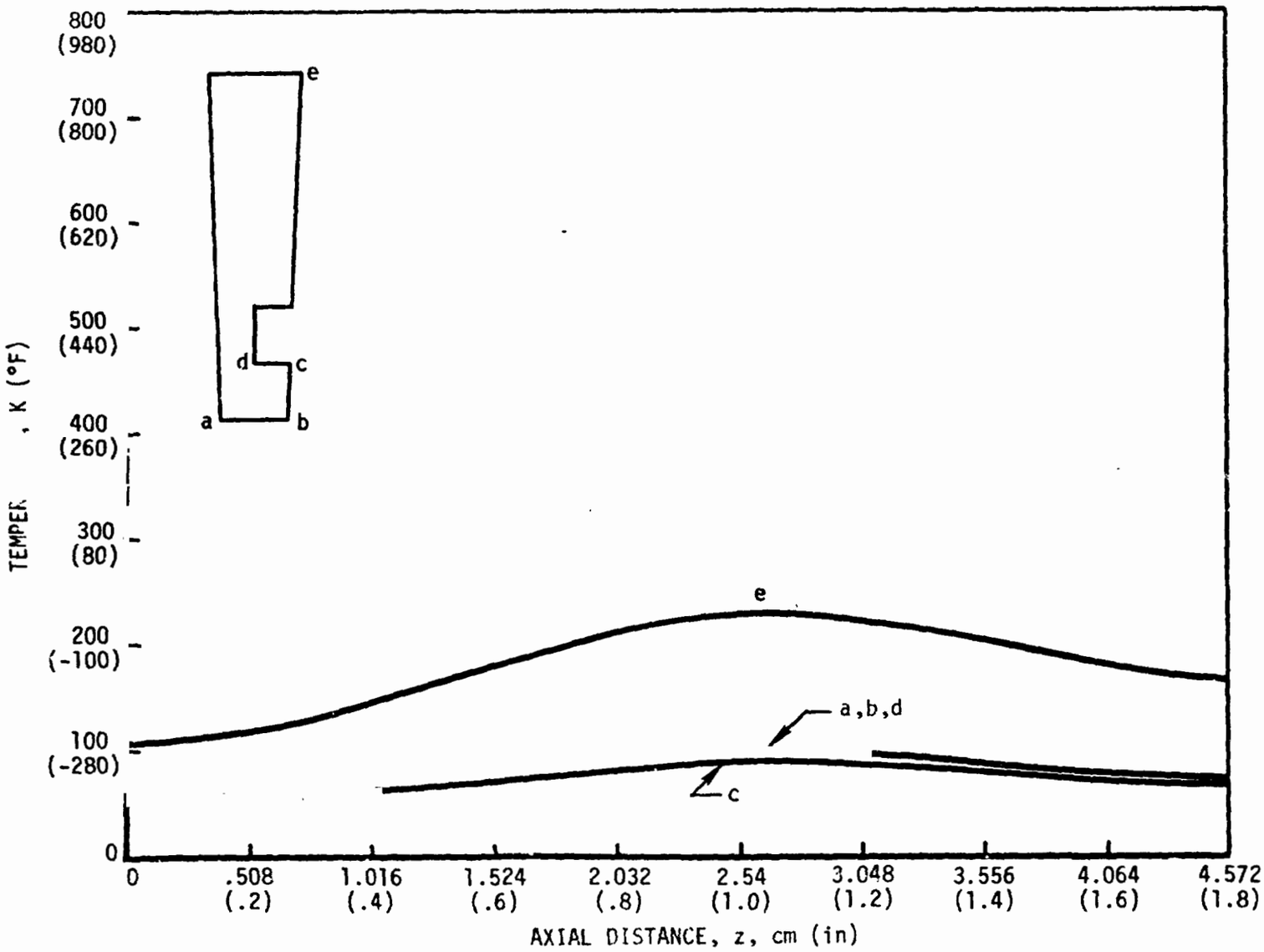

FIGURE 4.2-8 REPRESENTATIVE AXIAL TEMPERATURE DISTRIBUTIONS - CONFIGURATION B.3 AT t = 3.5 SEC

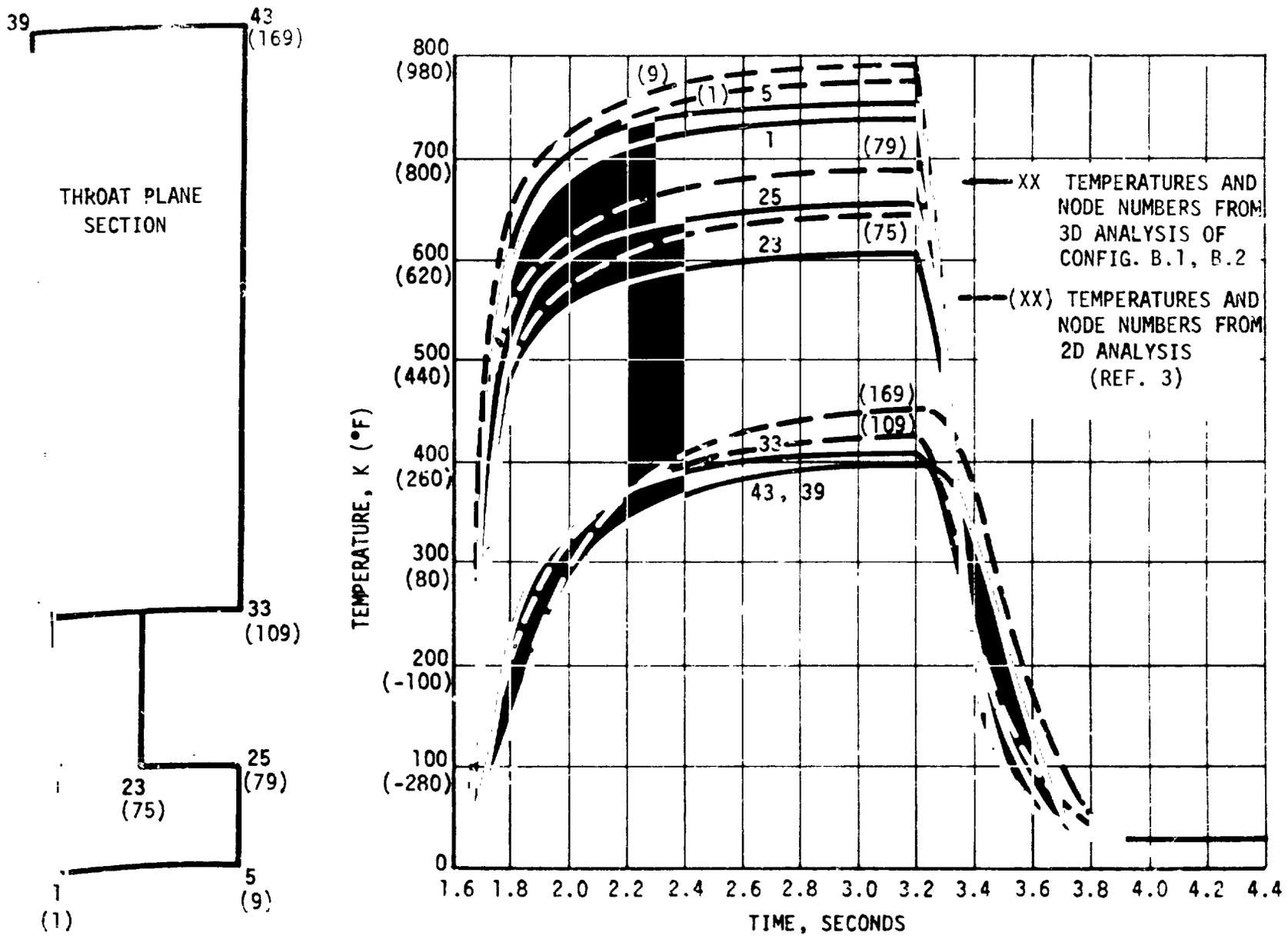

FIGURE 4.3-1 SAMPLE TEMPERATURE HISTORY COMPARISONS - 2D CONFIGURATION VS. 3D CONFIGURATION B.1, B.2

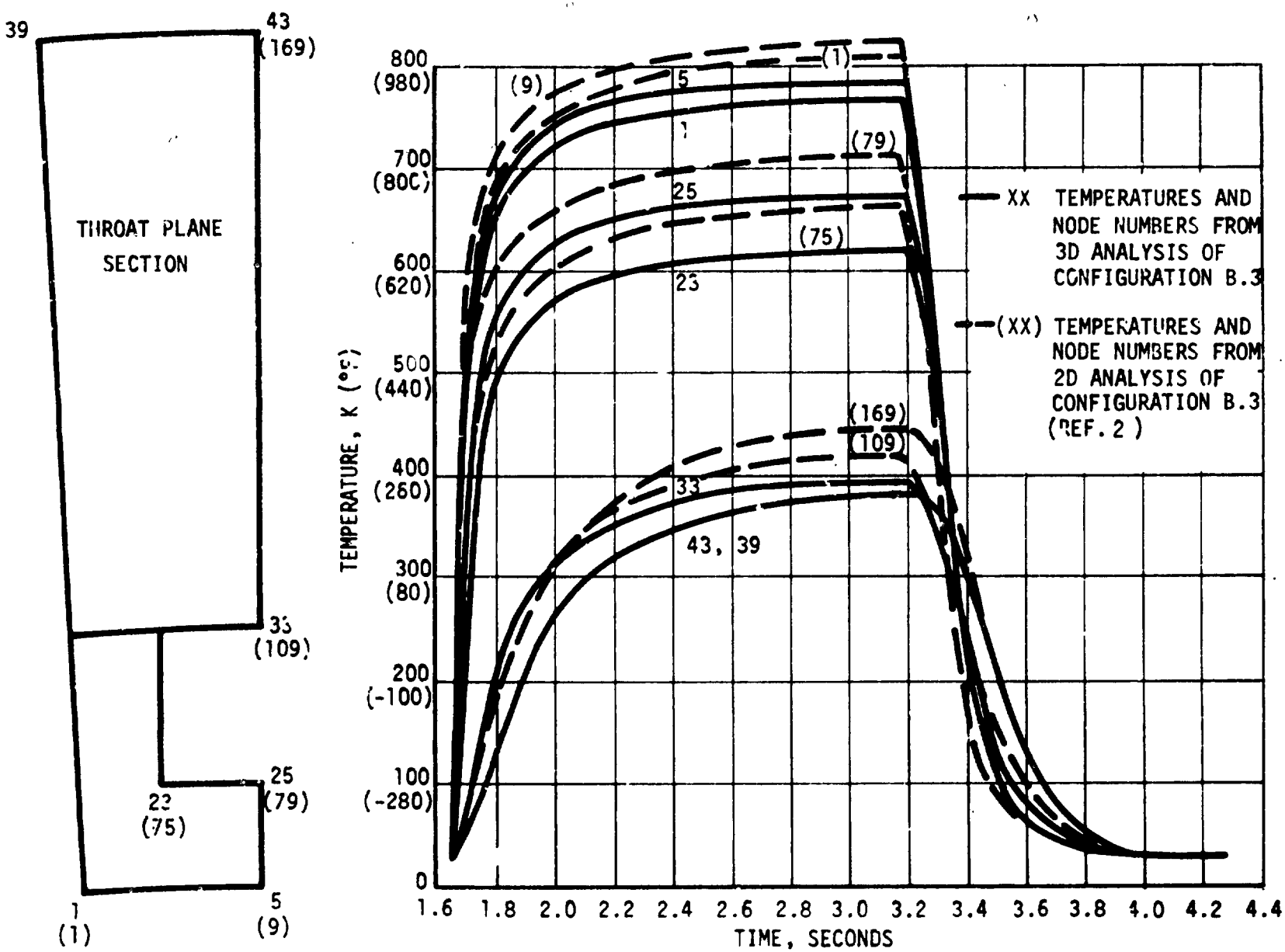

FIGURE 4.3-2 SAMPLE TEMPERATURE HISTORY COMPARISONS - 2D CONFIGURATION B.3 VS. 3D CONFIGURATION B.3

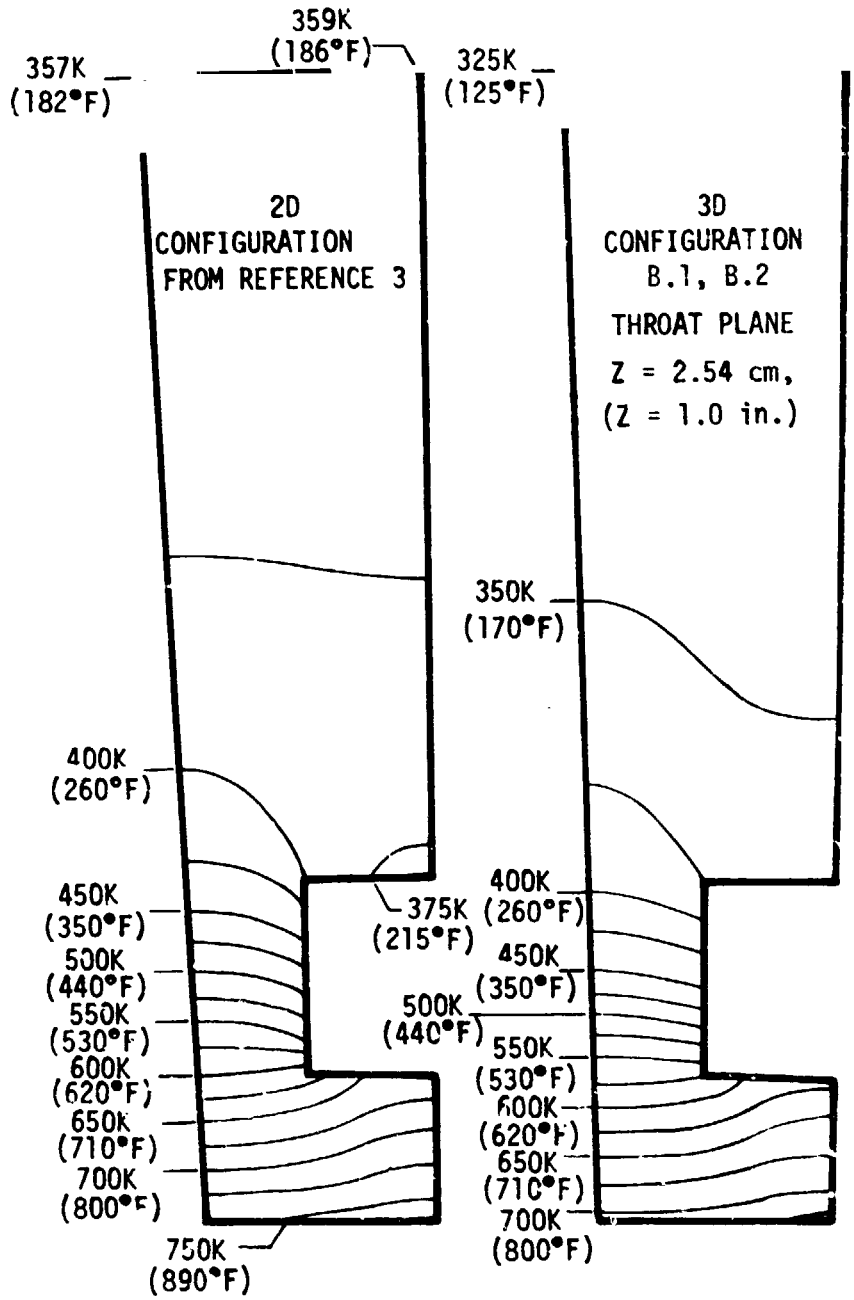

TEMPERATURES EARLY IN HEATING PHASE

(t = 2.15 SECONDS)

FIGURE 4.3-3 SAMPLE ISOTHERM COMPARISONS - TWO-DIMENSIONAL & THREE DIMENSIONAL ANALYSES (2.15 SECONDS)

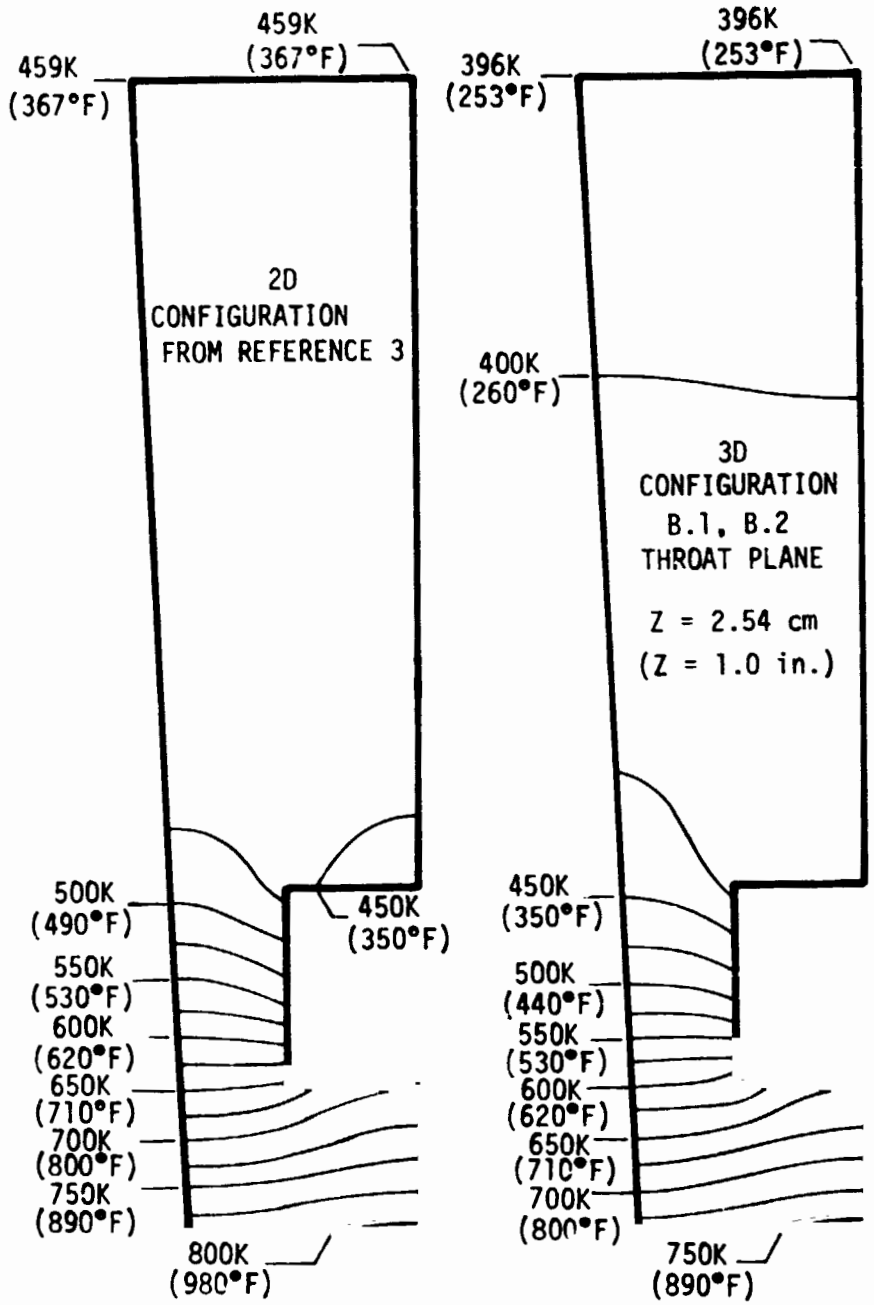

TEMPERATURE AT END OF HEATING PHASE (t = 3.2 SECONDS)

FIGURE 4.3-4 SAMPLE ISOTHERM COMPARISONS - TWO-DIMENSIONAL & THREE-DIMENSIONAL ANALYSES (3.2 SECONDS)

5.0 STRUCTURAL ANALYSIS

The structural analysis was performed with the aid of the BOPACE finite-element computer program for 3-dimensional analysis of problems in thermoviscoplasticity. The program accounts for, in an incremental manner, effects of variable amplitude cyclic loads and temperatures. In addition, nonlinear variations of material properties with temperature, mechanically or thermally induced plasticity, and combinations of creep and stress relaxation are incorporated in the program.

Three-dimensional solids are efficiently analyzed with the complex isoparametric elements provided in BOPACE 3-D. Convergence is achieved with a considerable reduction in mesh complexity when compared to simplex (linear) models used in other formulations. For example, it is shown in Section 5.1 that 9 complex elements replaced 281 simple triangles in a plane-strain analysis of the effects of initial chill-down and start transient phases of the thrust chamber operating cycle conditions at the cylinder throat plane.

Data from the 3-D thermal analysis were used to define thermal and mechanical loading in the form of cyclic histories of temperatures and forces applied to appropriate nodes of the BOPACE structural models. Output from BOPACE provides histories of stress and strain components and their effective values (i.e., equivalent uniaxial values). Strains are also decomposed into thermal, elastic, creep, and plastic parts and provided in the output.

Previous work in this area (Reference 2) utilized a 2-dimensional version of BOPACE to predict plane-strain cyclic behavior at the throat plane of the cylinders. The same operating cycle was used in the 3-D Thrust Chamber Life Prediction Study to: (1) re-examine the problem which is actually 3-dimensional in nature because there is nothing to constrain axial displacements of the cylinders during operation, (2) predict cyclic structural behavior and identify the location and time of occurrence of maximum strain during cyclic loading of each cylinder and (3) predict low-cycle fatigue life of the copper alloys which comprise the inner wall of the 3 cylinder configurations.

5.1 STRUCTURAL ANALYSIS MODEL

A previous life prediction study (Reference 2) required a highly detailed 2-dimensional model to accurately evaluate cyclic loading effects at the cylinder throat plane. The 2-D model consisted of 281 constant-strain-triangle elements and a plane-strain assumption at the throat. Results of that 2-D analysis provided the basis for determining mesh requirements of the 3-D model.

The approach to 3-D model development was to formulate several cylinder throat plane models from 3-D elements limited to plane-strain deformation; apply the 2-D pressures and temperatures for the initial chilldown and start transient phases of the cycle; and compare the 3-D model results with the 2-D data. Axisymmetric properties of the problem were used to model the smallest representative region with maximum practical detail. The most efficient 3-D element mesh was then selected to define the total 3-D cylinder model.

A comparison of characteristics of models used in the convergence evaluation is shown in Figure 5.1-1. The 281-element 2-D model along with 11-element, 9-element and 7-element 3-D-element models are shown. The 3-D(11) model performed satisfactorily, but this was expected since the number of degrees of freedom was almost the same as the 2-D(281) model. The 3-D(7) model was developed to decrease solution time, but evaluation of the results showed the 3-D(7) model could not converge to the required results. A third 3-D element model comprised of 9-elements was designed to achieve proper convergence in less solution time than required by the 3-D(11). Results presented in Table 5.1-I show that the 3-D(9) model compares favorably with the 2-D(281) and 3-D(11). A comparison of solution times showed that the 3-D(9) performed in approximately 75 percent of the time required by the 3-D(11).

The 3-D cylinder model subsequently developed from the 3-D(9) mesh is shown in Figure 5.1-2. The model consists of 72 elements, 452 nodes, and 1356 degrees-of-freedom. Gauss integration points located within each element

5.1 (Continued)

and near each corner node provide for output in the form of stresses and strains at those locations for each increment of loading during the cycle. Thus, cyclic stress-strain data were computed at 576 locations in the model. Twelve (12) elements which comprise the inner wall throat plane region (6 elements either side of the throat plane) provided 96 data points for the 3-D life analysis of this region. (The 2-D plane strain model required 139 data points for analysis of the same region).

Input data used to characterize the temperature dependent nonlinear material properties for BOPACE analysis were developed from the data in Section 3.1. Several assumptions were made in order to use the data for life analysis of the thrust chamber cylinders.

For example, fixed-strain-range hysteresis loops are generally used to estimate material hardening at temperature. Very little hysteresis data were available (Reference 1) for the copper alloys which comprise the outer cylinders. The hysteresis characteristics that were available were obtained from unpublished test data for Amzirc and NARloy-Z at temperatures in the range of 290°K to 900°K, strain ranges up to 3 percent, and rates of strain up to 1 percent per second. (The anticipated rate-of-strain in the inner wall was expected to be on the order of magnitude of 10 percent per second during transient phases of the cycle). The cyclic test data for Amzirc and NARloy-Z indicated that copper alloys are strain rate sensitive. At strain rates approaching 1 percent per second, the materials appeared to stabilize within fewer than 10 cycles of loading and then exhibited no isotropic hardening or softening. Also, the test data indicated no measurable change in kinematic hardening after initial loading of a specimen. Thus, it was assumed for this study that typical strain stabilized behavior of the various materials could be characterized by no isotropic hardening and no change in yield with reversal of strain. What this means is that the monotonic stress-strain curves of Section 3.1 were assumed to constitute both tensile and compressive behavior of the materials with no change in size of the hysteresis loop or yield point during the operating cycle.

5.2 STRAIN AND FATIGUE LIFE ANALYSIS RESULTS

Results of the structural analyses were summarized by the histories of effective strains at the critical location in each cylinder configuration. The critical location is defined as the node exhibiting the maximum effective strain range during the operating cycle. Strain histories for radial, circumferential, and axial strain components are also shown. Values of shear strain were computed but were used only in determining the effective strain values because predicted shearing strains were 1-to 2-orders-in-magnitude smaller than the direct components; no plots of shear strain histories are presented.

Effective strains were used in predicting cyclic damage because the curves (reference Section 3.1) used to predict low-cycle fatigue life were all developed from uniaxial test specimens. The total effective strain (equivalent uniaxial strain) was computed from the equation

$$\varepsilon_{eff} = \sqrt{2/3} \quad \sqrt{e_r^2 + e_\theta^2 + e_z^2 + 2\,(\gamma_{r\theta}^2 + \gamma_{rz}^2 + \gamma_{\theta z}^2)} \qquad (5.2\text{-}1)$$

where subscripts r, θ, and z denote radial, circumferential, and axial directions respectively, and e and γ denote direct and shearing deviatoric strain components. The direct deviatoric strains are defined in the usual manner as

$$\begin{aligned} e_r &= \varepsilon_r - \varepsilon \\ e_\theta &= \varepsilon_\theta - \varepsilon \\ e_z &= \varepsilon_z - \varepsilon \end{aligned} \qquad (5.2\text{-}2)$$

where

$$\varepsilon = (\varepsilon_r + \varepsilon_\theta + \varepsilon_z)/3 \qquad (5.2\text{-}3)$$

is the dilatational strain. The predicted direct and shear strain components are composed of the elastic, inelastic, and thermal quantities. For example,

5.2 (Continued)

$$\varepsilon_r = \varepsilon_r^e + \varepsilon_r^p + \varepsilon_r^c + \varepsilon_r^T \qquad (5.2\text{-}4)$$

where superscripts e, p, c, and T denote elastic, plastic, creep, and thermal strain.

The critical strain data for the cylinders are presented in Figures 5.2-1 through 5.2-10. The location of critical strain was at the throat plane on the heated surface of the rib centerline. This location coincides with node identification number 209 in the 3-D finite-element model. Values of strain at node 209 were determined by interpolation of BOPACE computed strains at Gauss integration points on each side of the throat plane. The time origin of the strain histories is the beginning of the start transient phase of the cycle, and the histories of total strain were assumed to be repetitive throughout the life of the structure.

A summary of predicted low-cycle fatigue life based on the 3-D thermal and structural analyses is presented in Table 5.2-I. This data shows that 1/2-hard Amzirc is the best of the three materials considered for extending the fatigue life of the thrust chamber liner. Amzirc, with a life expectancy of 3000 cycles, has a predicted life 2.3 times greater than NARloy-Z and 20 times greater than OFHC copper.

3-D Analysis of Cylinder Configuration B.1

Histories of critical strains and their effect on life of configuration B.1 are presented in Figures 5.2-1, 5.2-2 and 5.2-3. The maximum effective strain, 1.3 percent, occurred at approximately 0.2 second after engine start. The condition at the critical location for this time point was a plane-strain condition, i.e., there was zero axial strain at this point in the cycle. The predicted temperature at the critical location at this time was 600 °K, and the chamber and coolant channel pressures at the throat were 2.56 MN/m^2 and 6.65 MN/m^2 respectively.

5.2 (Continued)

The component strains showed a slight increase during the remainder of the heating phase and there was a small decrease in total effective strain during this period. The predicted temperature at the end of the heating phase (time = 1.55 seconds) was 760°K; pressures were the same as at 0.2 second.

The shutdown caused a reversal in strains and resulted in a residual effective strain of 0.1 percent at approximately 2.1 seconds after engine start. The predicted temperature was stable and uniform at 28°K and chamber and coolant channel pressures at the throat were 0.1 MN/m^2 and 5.2 MN/m^2.

The total effective strain range obtained by summing the maximum values predicted during the heating and cooling phases of the cycle was 1.4 percent. It was observed that a relatively high strain range condition was predicted for the inner wall of the thrust chamber in a region shown by the shaded area in Figure 5.2-11. The average value of effective strain range in this region was 1.3%. The maximum and average strain range values were applied to the typical fatigue life curves as shown in Figure 5.2-3. The predicted cycles to fracture was 3000 cycles for the maximum effective strain range and 3500 cycles for the average value of strain range in the inner wall.

3-D Analysis of Cylinder Configuration B.2

The critical strains for configuration B.2 are presented in Figures 5.2-4 and 5.2-5. The predicted temperatures and pressures were the same as for configuration B.1 because the boundary conditions and typical thermal material properties were the same for both cylinders. It was observed however, that the maximum effective strain, approximately 1.7 percent, occurred at about 0.4 second after beginning of the heating phase in B.2. The predicted temperature at this time was approximately 670°K.

5.2 (Continued)

A plane-strain condition existed at 0.4 second, but it should be noted that the axial strain component was small ($\leq$ 0.1 percent) during the major portion of the heating phase. This indicates that a 2-D plane-strain assumption should provide a good approximation of conditions at the throat of the B.2 cylinder during the heating phase.

The residual effective strain was approximately 0.2 percent. The residual condition was again reached at approximately 2.1 seconds into the cycle. Thus, a maximum effective strain range of 1.9 percent was predicted for B.2. The maximum strain occurred at node 209, but the average strain in the inner wall region was 1.6 percent. These effective strain range values were applied to the fatigue life curve presented in Figure 5.2-6. The predicted cycles to fracture which correspond to the maximum and average strain range values were 150 and 210 cycles respectively.

Typical creep behavior for the three cylinder configurations is represented by the curve in Figure 5.2-7. This figure shows the first cycle effective creep strain history at node 209 of configuration B.2. The values predicted at other node locations were slightly smaller, but all effective creep strains were the same order of magnitude throughout the throat plane of the inner wall. Configuration B.2 was selected to show time dependent strain behavior because its predicted values of effective creep strain were highest of the three configurations. The significant factor in the plot of first cycle creep is that the total effective strain is approximately 500 times greater than the effective creep. Thus creep is not a significant damage mechanism in low-cycle fatigue of the cylinders. Also, creep strain is expected to remain almost constant after the first cycle because of hardening and the fact that unloading during the shutdown transient happens so rapidly that measurable creep reversal will not occur.

5.2 (Continued)

3-D Analysis of Cylinder Configuration B.3

The critical strains for configuration B.3 are presented in Figures 5.2-8 and 5.2-9. The maximum effective strain, approximately 1.6 percent, occurred at 0.3 second after engine start which also coincides with a plane-strain condition at the critical location. The predicted temperature at the critical location at this time was approximately 670°K. Pressures in the chamber and coolant channel were 2.56 MN/m^2 and 6.65 MN/m^2 respectively. The pressures were constant during the remainder of the heating phase, but temperatures at the critical location increased to 770°K. Thus temperatures for B.3 were slightly higher than for B.1 and B.2, but pressure loading was the same in all cases.

The residual effective strain at the end of shutdown transient conditions was approximately 0.1 percent. The total effective strain range obtained by adding maximum values during the heating and cooling phases was approximately 1.7 percent. The average strain within the shaded region of Figure 5.2-11 was 1.6 percent. A comparison of predicted cycles to fracture using maximum and average effective strain ranges in the inner wall of B.3 is shown in Figure 5.2-10; the predicted low-cycle fatigue life for the maximum and average strain range was 1300 and 1500 cycles respectively.

Effective Strain Range Distribution

The effective strain range predicted at the throat plane defined a region of high strain extending diagonally across the inner wall of all three configurations. This "band" of high strain is indicated by the diagonal of the shaded areas in Figure 5.2-11. The distributions also show that the effective strain range within the shaded areas was almost uniform, and although maximum values of effective strain range were observed at the lower left hand

5.2 (Continued)

corner (node 209) of each figure, it's more reasonable to assume that fracture would occur in the thin section near the centerline of the channel. This failure mode is even more likely if any measurable change in geometry (such as thinout and bulging under pressure) occurs due to plastic flow during the cyclic life. It is suggested that the predicted life of the cylinders will be in a range of cycles corresponding to the maximum and minimum values of effective strain range within the shaded region. Further, it is suggested that the typical life of each cylinder will correspond to the values predicted by the average value of effective strain range.

Distribution of effective strain range along the axis of the cylinder was evaluated to verify the throat plane inner wall as the critical region. These strain distributions are presented in Figures 5.2-12, 5.2-13, and 5.2-14.

5.3 COMPARISON OF 2-D AND 3-D STRUCTURAL ANALYSIS

A previous analysis (Reference 2) of the thrust chambers was performed with the use of the BOPACE computer program. The model used in Reference 2 was the 2-D plane-strain model comprised of 281 constant strain triangles (see Figure 5.1-1). Results of the 2-D analysis are presented in Figures 5.3-1 through 5.3-6 in the form of strain histories at locations which coincide with the critical locations of the 3-D model. In general, these data show that the 2-D radial strains were approximately the same as the 3-D radial components during the heating phase, but the magnitudes of the 2-D radial strains were larger during the cooling phase. The circumferential strain components exhibit the opposite characteristics during the cycle. It should be noted that the 2-D results were obtained from the cycle specified for the 2-D thermal analysis and resulted in slightly higher temperatures (< 50°C) than predicted for 3-D models during the heating phase. The temperature difference apparently had a negligible effect on difference in structural behavior of the 2-D and 3-D models.

5.3 (Continued)

Comparisons of the 2-D and 3-D effective strain histories show that the effective strain range computed with the 2-D model was larger for configurations B.1 and B.3 but was approximately the same in both models of configuration B.2. This may be due to the fact that 3-D axial strains in B.2 were smaller in magnitude than in the other two configurations and more closely approached the plane-strain condition assumed for the 2-D analyses.

The effective strain range distribution obtained from the 2-D data is shown in Figure 5.3-7. The values are shown for locations which coincide with the locations shown in Figure 5.2-11. The shaded area defines the region of greatest damage in the inner wall and is the same as the critical region in the 3-D models. It was also observed that the maximum values of effective strain range occurred generally along the diagonal boundary of the shaded area.

A comparison of the values presented in Figures 5.2-11 and 5.3-7 shows that 2-D strains were generally higher than corresponding 3-D results. Only three locations shown for the 2-D model of configuration B.2 had strains less than those computed in the 3-D model of B.2. Thus the life predictions based on 2-D results tended to be lower. It was also observed that critical locations in B.1 and B.3 were at the channel centerline rather than the rib centerline of the 3-D models. A summary of the 2-D and 3-D comparisons is presented in Table 5.3-I.

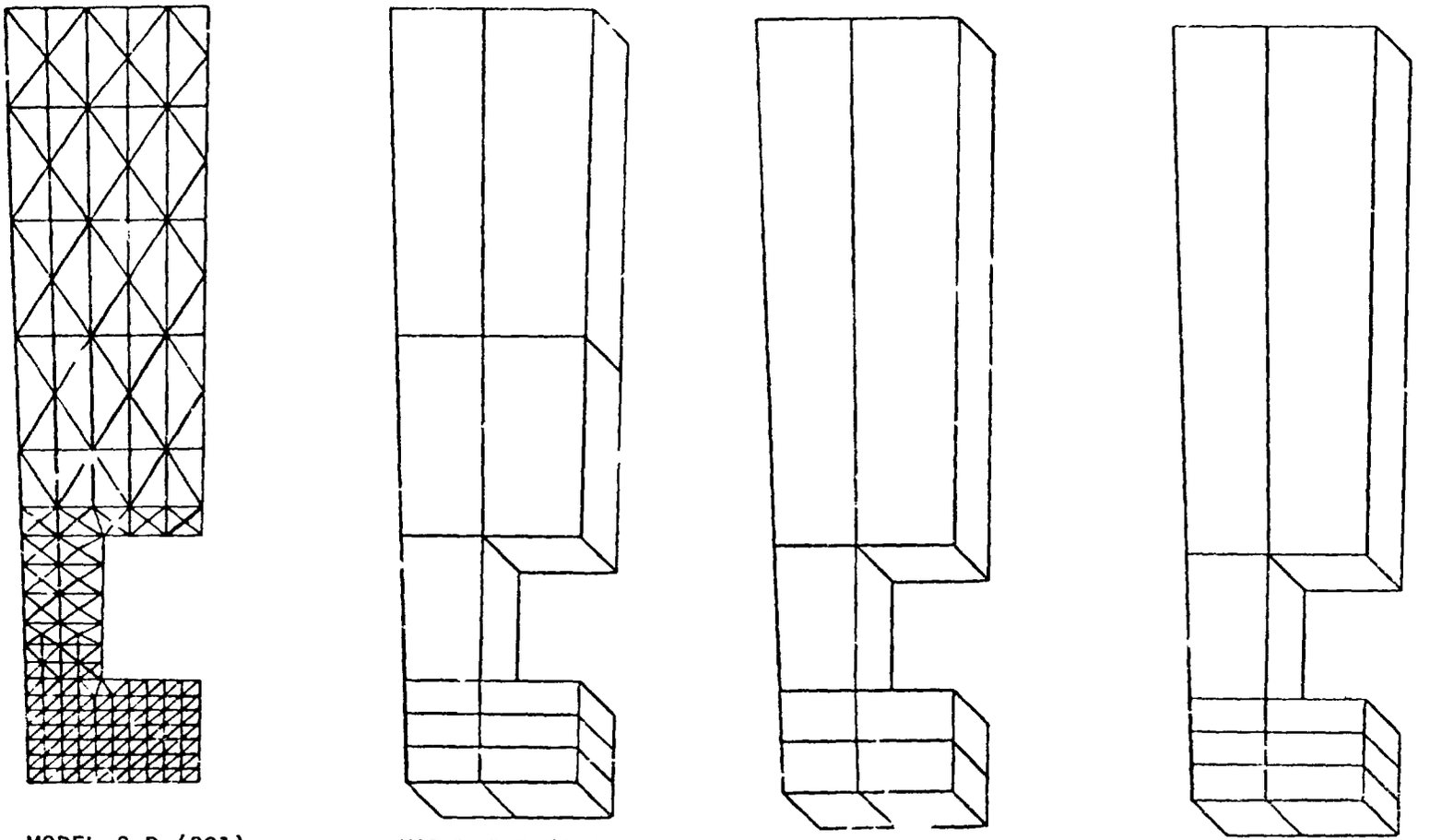

MODEL 2-D (281)
TOTAL ELEMENTS = 281
TOTAL NODES = 174
TOTAL FREEDOMS = 348

MODEL 3-D (11)
TOTAL ELEMENTS = 11
TOTAL NODES = 111
TOTAL FREEDOMS = 333

MODEL 3-D (7)
TOTAL ELEMENTS = 7
TOTAL NODES = 73
TOTAL EDOMS = 219

MODEL 3-D(9)
TOTAL ELEMENTS = 9
TOTAL NODES = 95
TOTAL FREEDOMS = 285

FIGURE 5.1-1 3-D FINITE ELEMENT MODEL DEVELOPMENT - COMPARISON OF MODEL CHARACTERISTICS

TABLE 5.1-I 3-D FINITE-ELEMENT MODEL DEVELOPMENT - COMPARISON OF EFFECTIVE STRAINS

TIME* (sec)	MODEL	EFFECTIVE STRAIN (PERCENT) 1	2	3	4
0.00	2-D(281)	0.37	0.37	0.37	0.37
	3-D(11)	0.37	0.37	0.37	0.37
	3-D(7)	0.37	0.37	0.37	0.37
	3-D(9)	0.37	0.37	0.37	0.37
0.05	2-D(281)	0.67	0.48	0.52	0.43
	3-D(11)	0.62	0.46	0.52	0.43
	3-D(7)	0.56	0.44	0.47	0.37
	3-D(9)	0.62	0.46	0.53	0.43

REGIONS USED FOR STRAIN COMPARISON

*TIME MEASURED FROM BEGINNING OF START TRANSIENT PHASE OF OPERATING CYCLE FOR 2-D ANALYSES. TIME 0.00 REPRESENTS CONDITION AT END OF INITIAL CHILLDOWN TO UNIFORM TEMPERATURE OF 27.8°K (50°R).

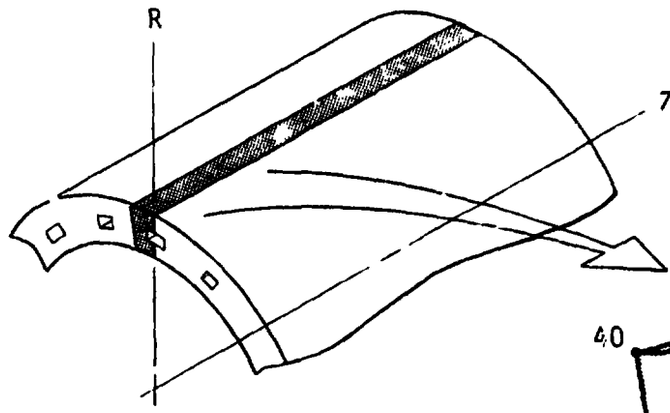

NOTES:

1. Forty-four (44) nodes are used on each plane identified by Z-dimensions.
2. Seven (7) nodes are used midway between planes to allocate consistent nodal forces for chamber and coolant channel pressures.
3. Throat plane nodes are numbered consecutively 209 through 252.
4. Node identification (I.D.) numbers run from 1 through 460; most node numbers ommitted for clarity.
5. Total elements = 72.
6. Total nodes = 452.
7. Total freedoms = 1356.

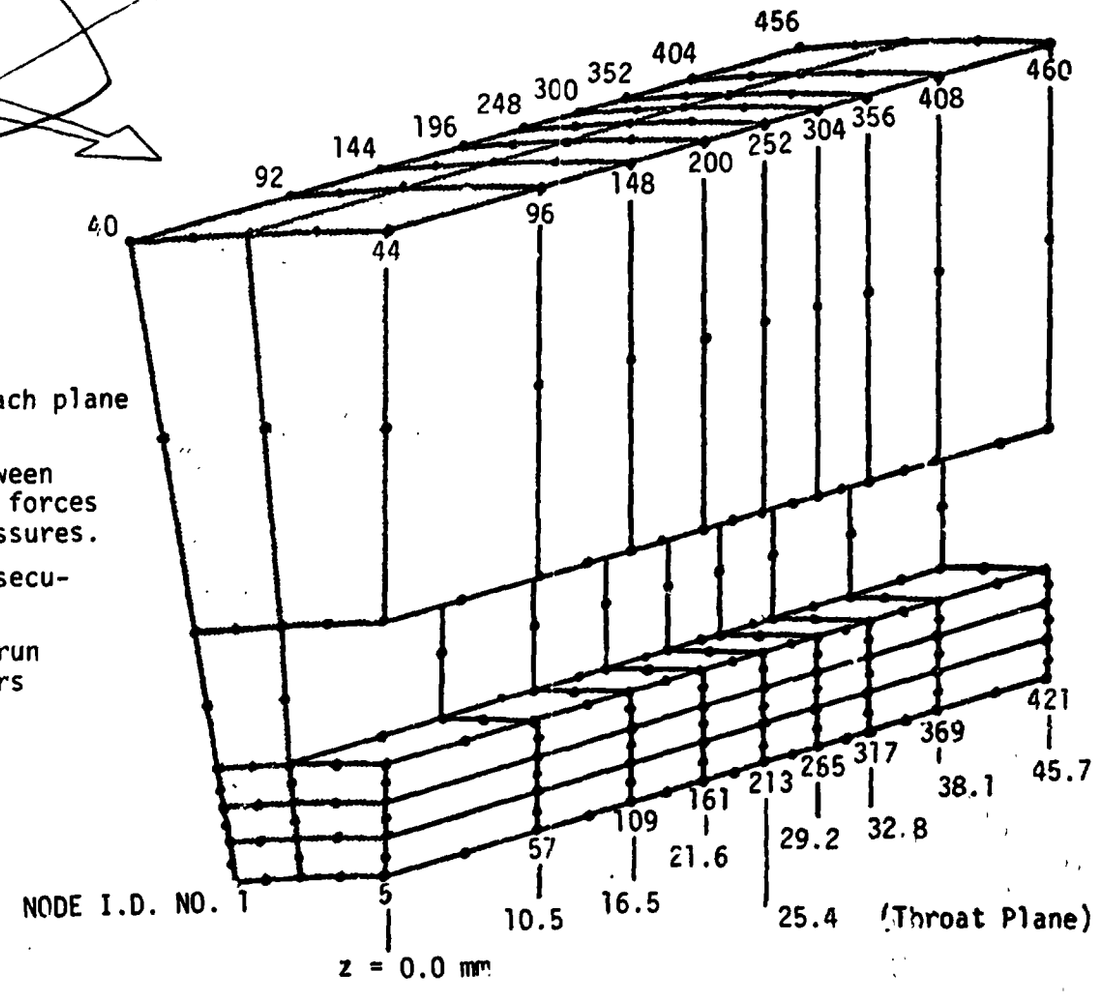

FIGURE 5.1-2 3-DIMENSIONAL FINITE ELEMENT MODEL

TABLE 5.2-I 3-D THRUST CHAMBER LIFE PREDICTION SUMMARY

CONFIGURATION	MAXIMUM EFFECTIVE STRAIN RANGE (%)	MAXIMUM TEMPERATURE (°R)	PREDICTED LIFE (CYCLES)
B.1	1.4	1360	3000
B.2	1.9	1360	150
B.3	1.7	1410	1300

THE LOCATION OF MAXIMUM EFFECTIVE STRAIN RANGE IS NODE 209 WHICH IS LOCATED AT INTERSECTION OF THROAT PLANE, CENTERLINE OF RIB, AND HEATED SURFACE OF INNER WALL.

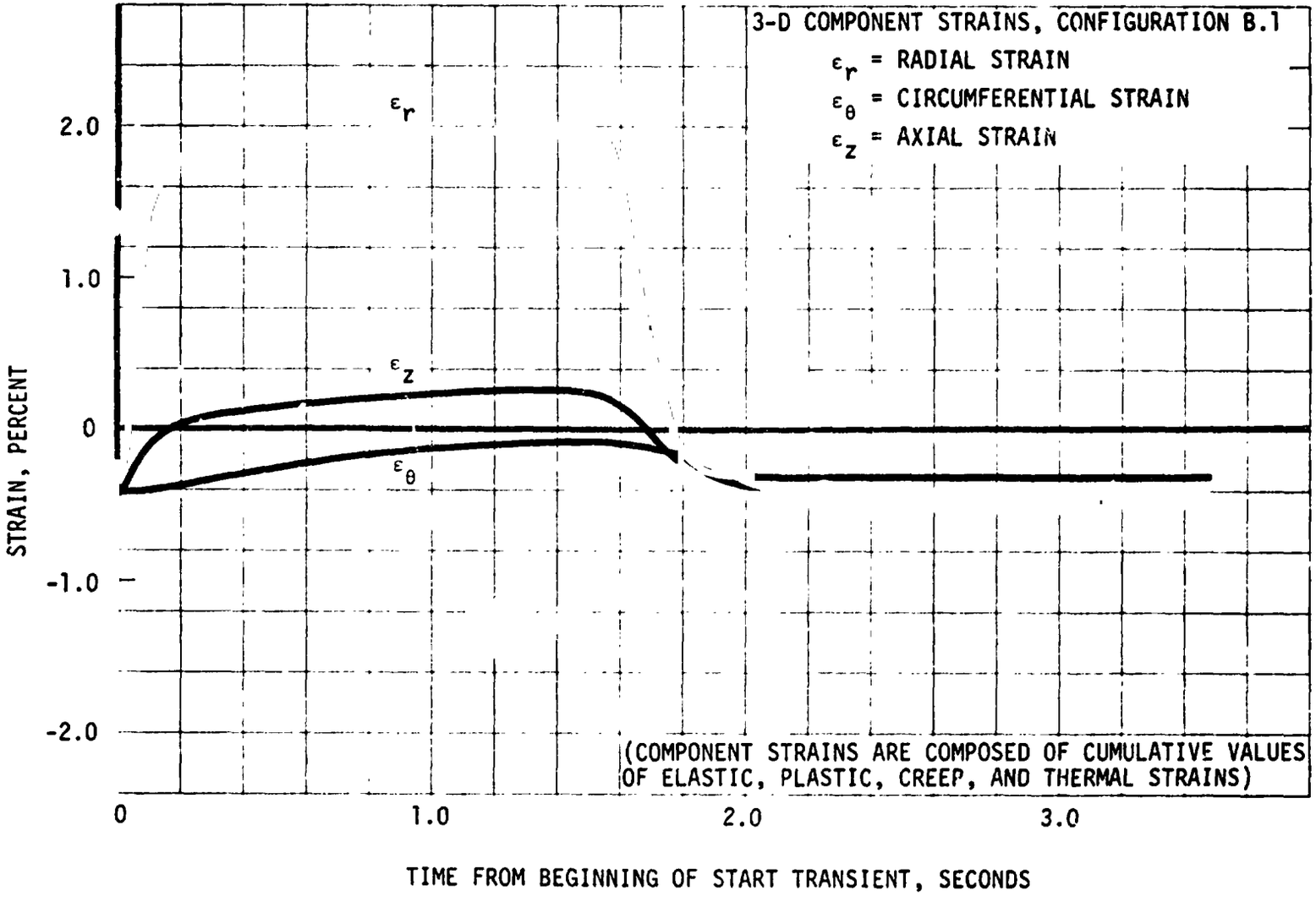

FIGURE 5.2-1 3-D CYCLIC STRAIN ON INNER WALL HEATED SURFACE AT RIB CENTERLINE, CONFIGURATION B.1 THROAT PLANE

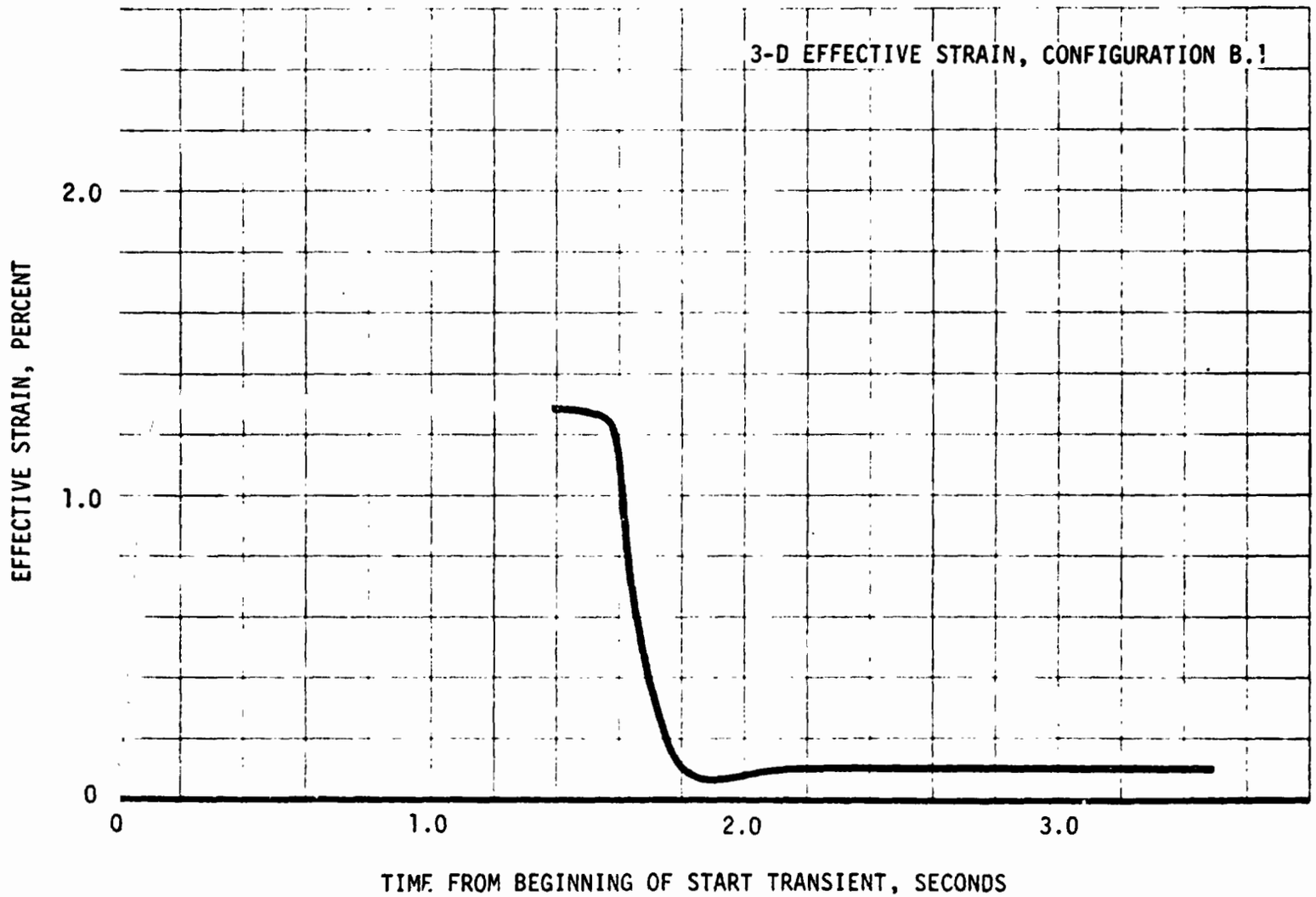

FIGURE 5.2-2 3-D CYCLIC EFFECTIVE STRAIN ON INNER WALL HEATED SURFACE AT RIB CENTERLINE, CONFIGURATION B.1 THROAT PLANE

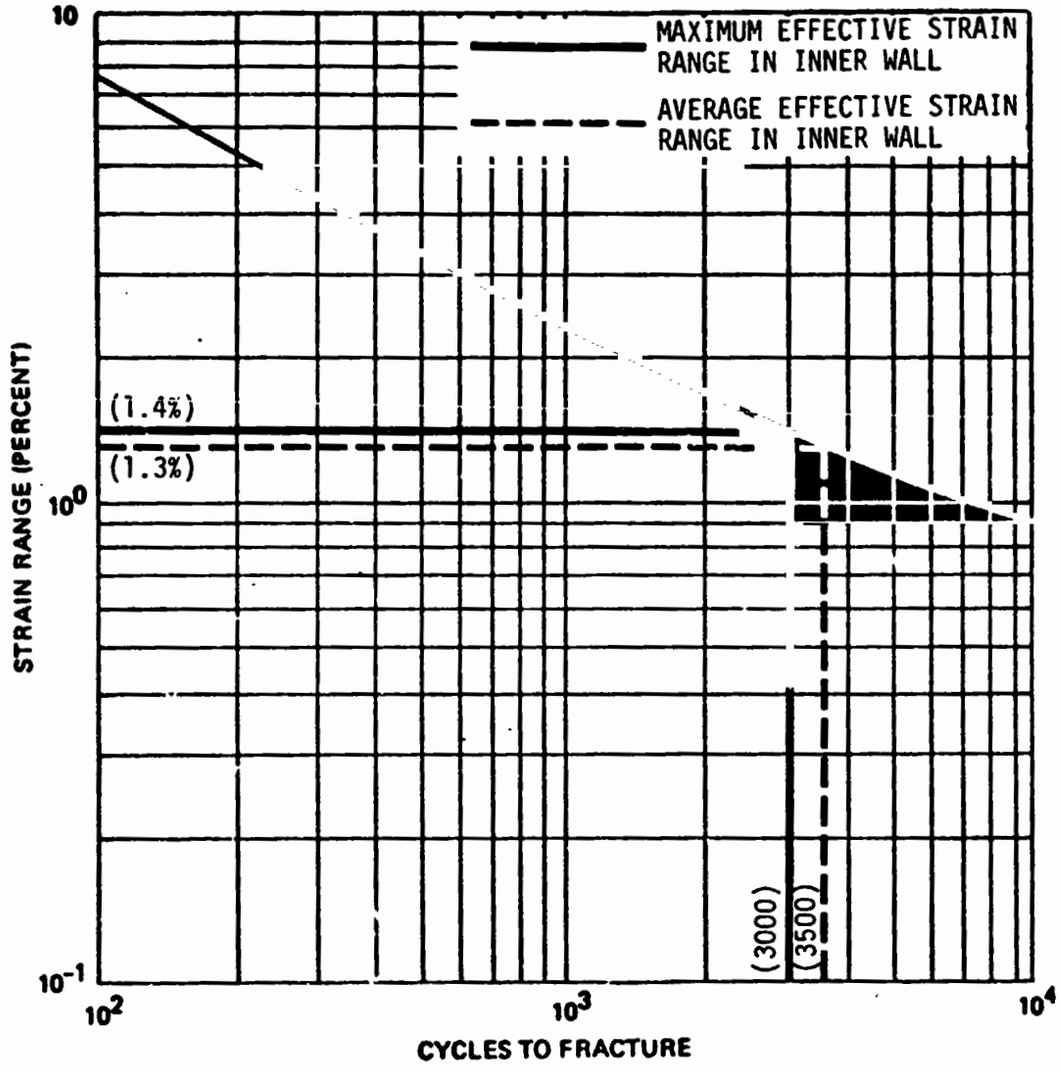

FIGURE 5.2-3 CYCLES TO FRACTURE BASED ON PREDICTED EFFECTIVE STRAIN RANGE AT THROAT PLANE OF CONFIGURATION B.1

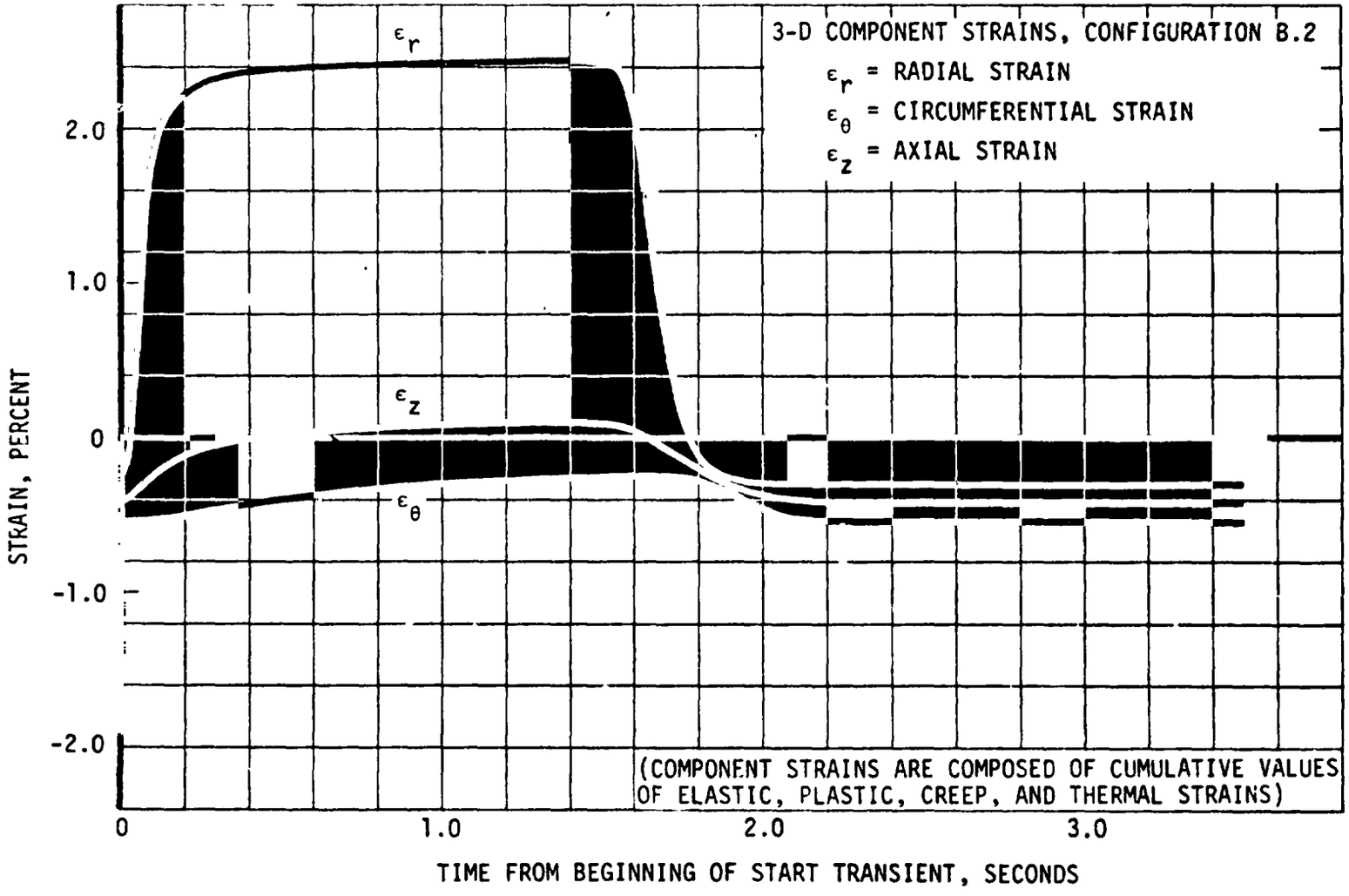

FIGURE 5.2-4 3-D CYCLIC STRAIN ON INNER WALL HEATED SURFACE AT RIB CENTERLINE, CONFIGURATION B.2 THROAT PLANE

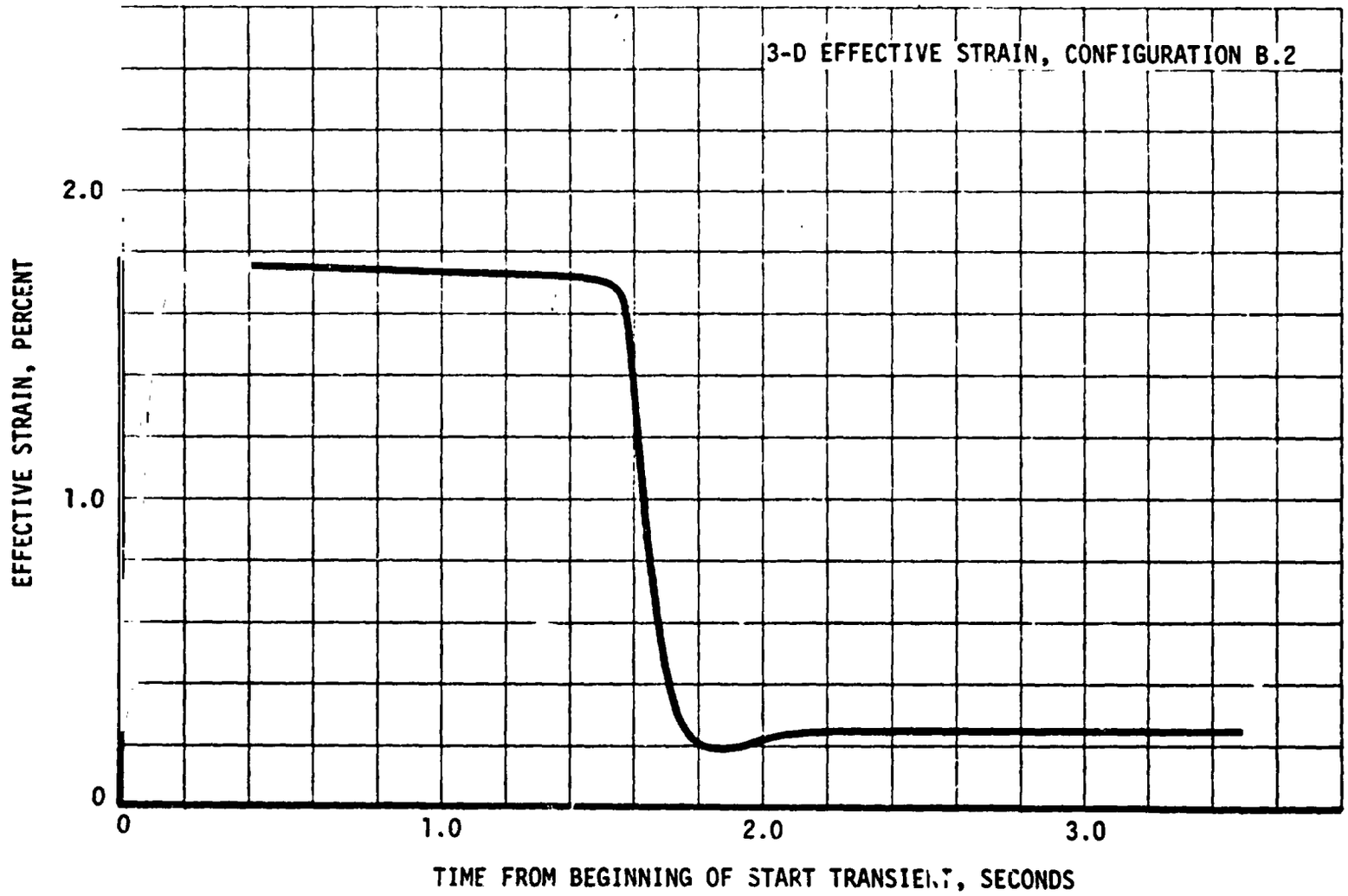

FIGURE 5.2-5 3-D CYCLIC EFFECTIVE STRAIN ON INNER WALL HEATED SURFACE AT RIB CENTERLINE, CONFIGURATION B.2 THROAT PLANE

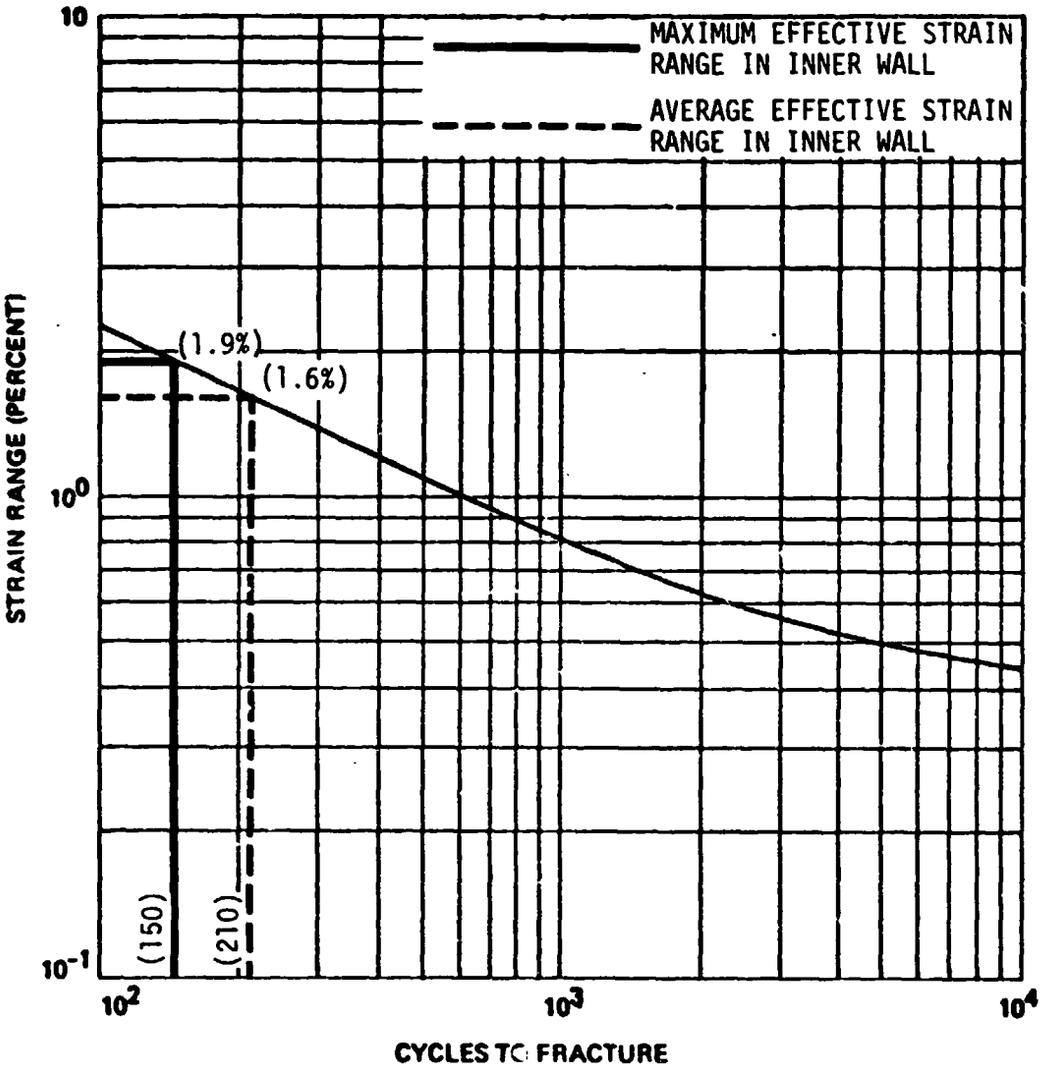

FIGURE 5.2-6 CYCLES TO FRACTURE BASED ON PREDICTED EFFECTIVE STRAIN RANGE AT THROAT PLANE OF CONFIGURATION B.2

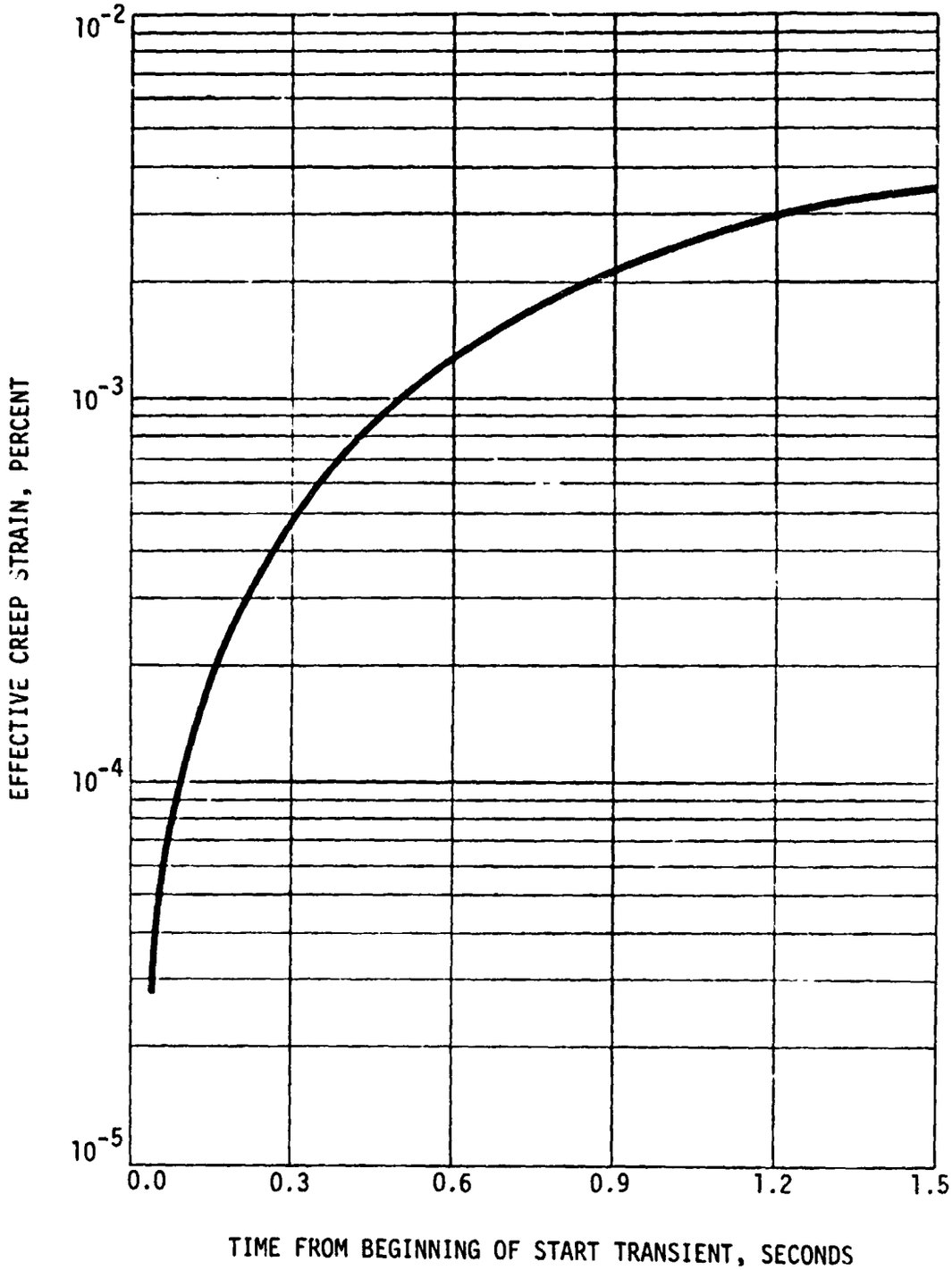

FIGURE 5.2-7 FIRST-CYCLE EFFECTIVE CREEP STRAIN AT THROAT PLANE OF CONFIGURATION B.2

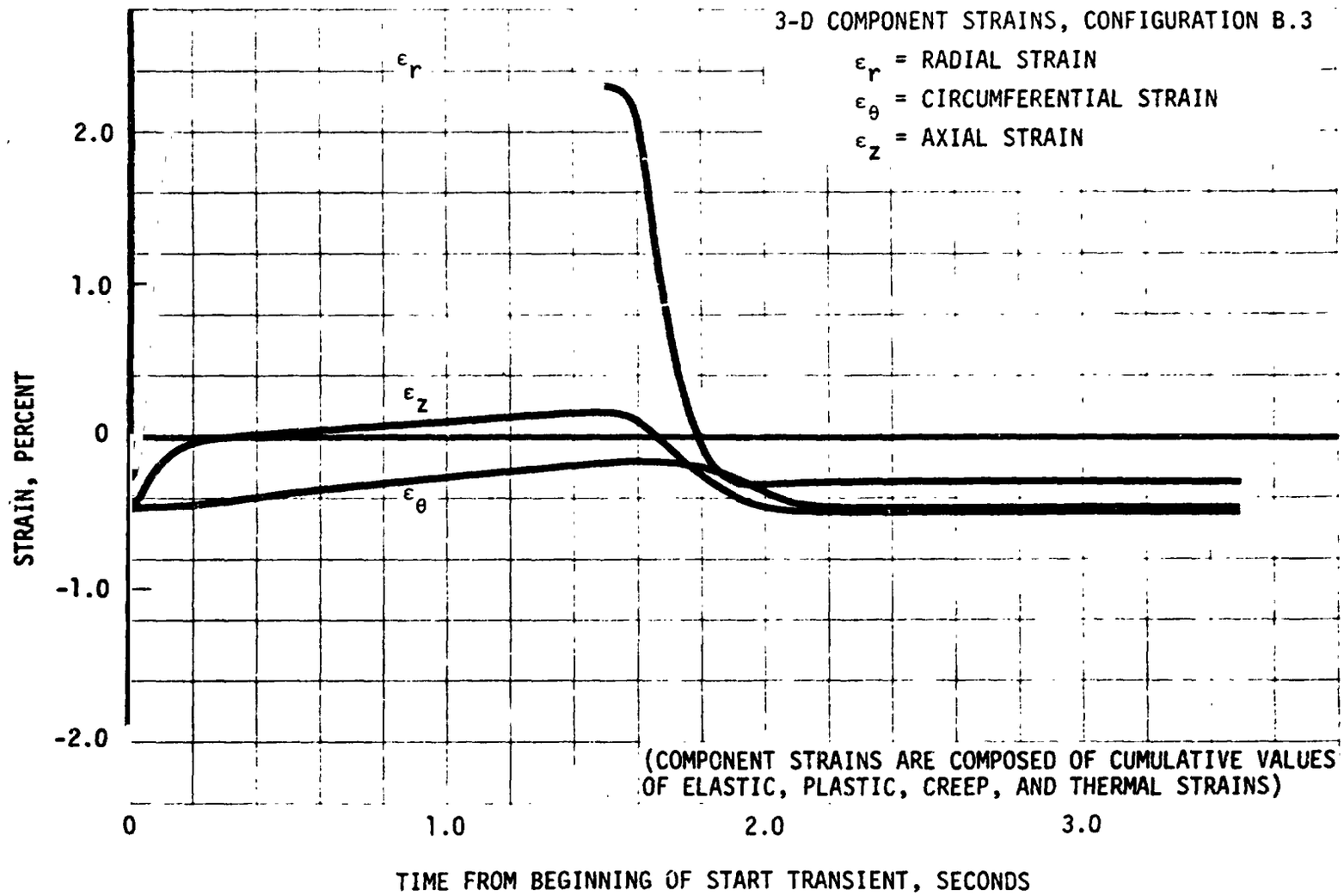

FIGURE 5.2-8 3-D CYCLIC STRAIN ON INNER WALL HEATED SURFACE AT RIB CENTERLINE, CONFIGURATION B.3 THROAT PLANE

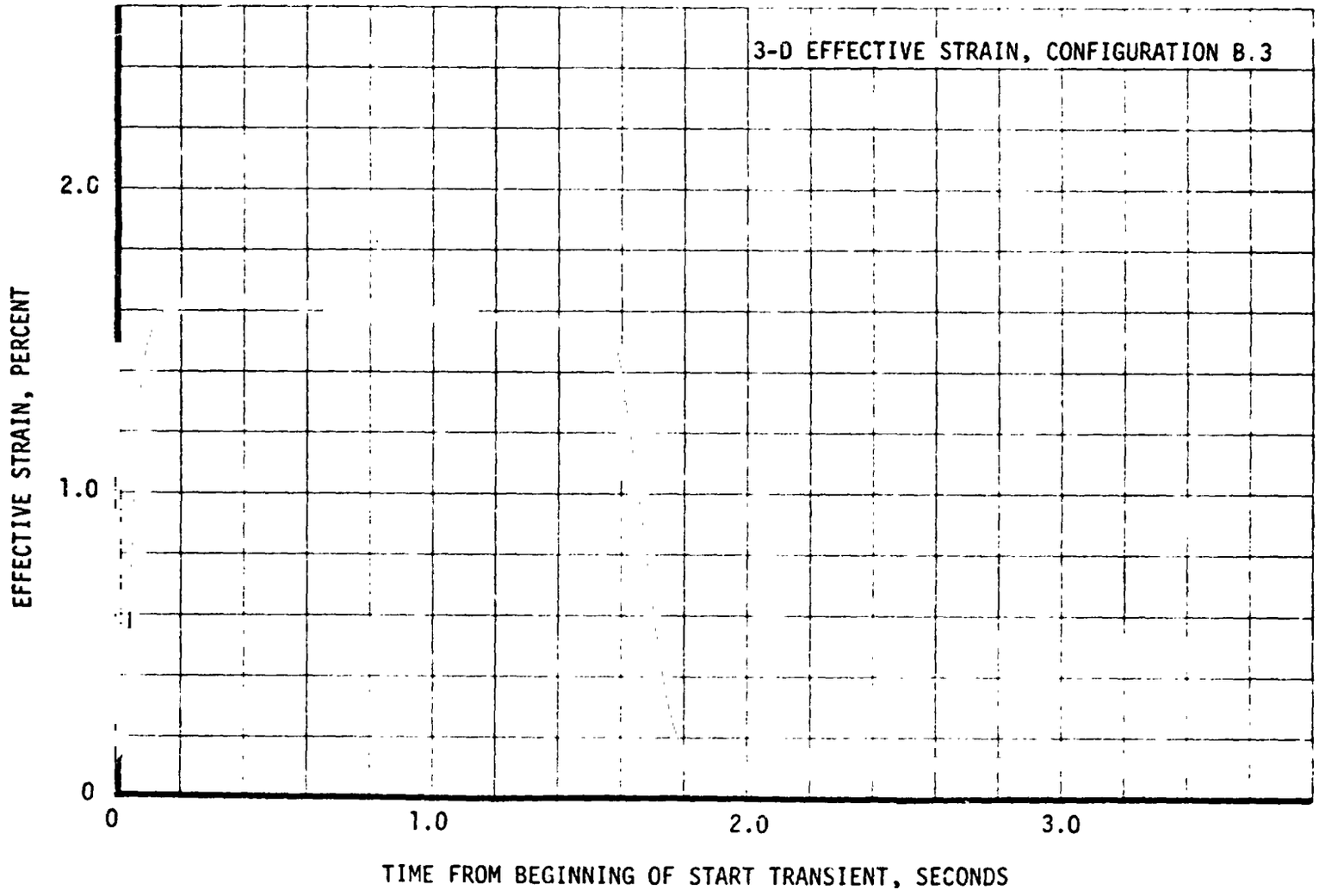

FIGURE 5.2-9 3-D CYCLIC EFFECTIVE STRAIN ON INNER WALL HEATED SURFACE AT RIB CENTERLINE. CONFIGURATION B.3 THROAT PLANE

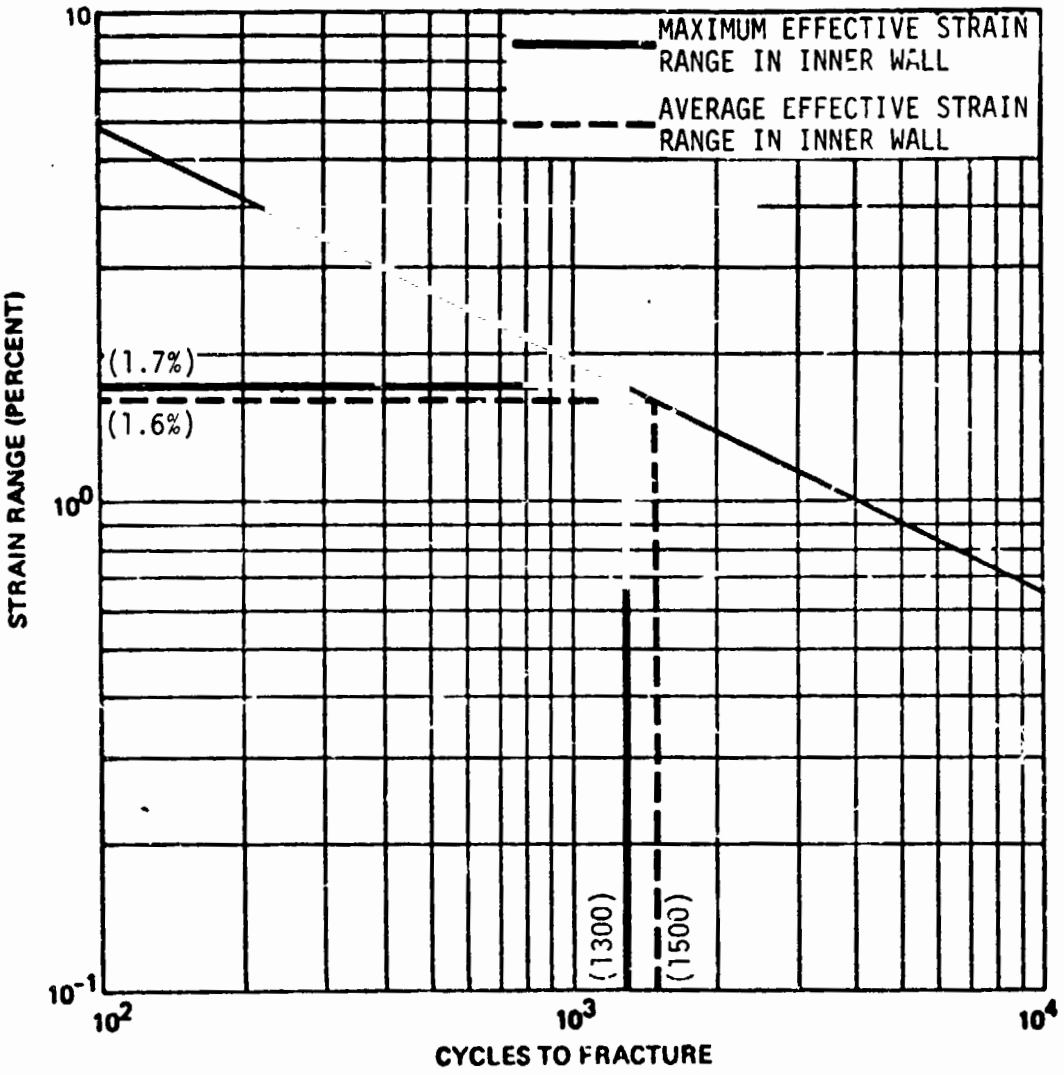

FIGURE 5.2-10 CYCLES TO FRACTURE BASED ON PREDICTED EFFECTIVE STRAIN RANGE AT THROAT PLANE OF CONFIGURATION B.3

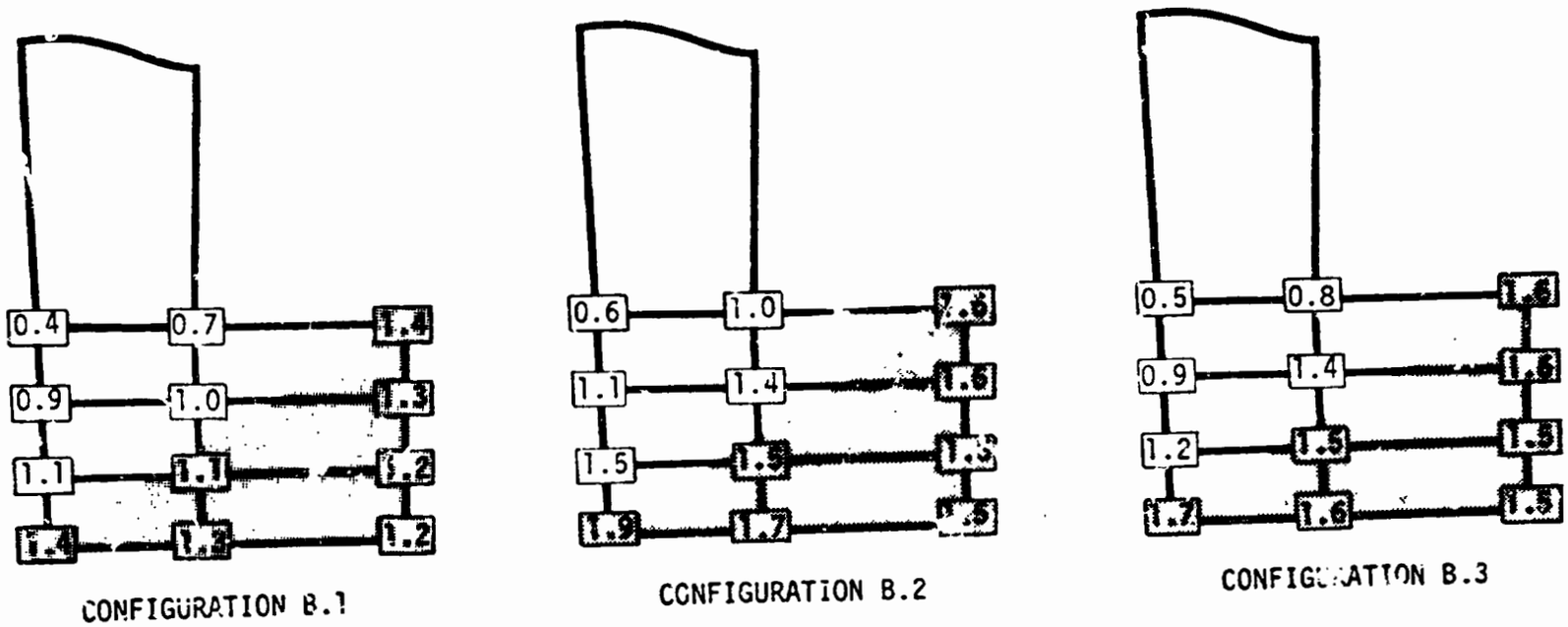

FIGURE 5.2-11 EFFECTIVE STRAIN RANGE DISTRIBUTION (PERCENT) AT CYLINDER THROAT PLANE

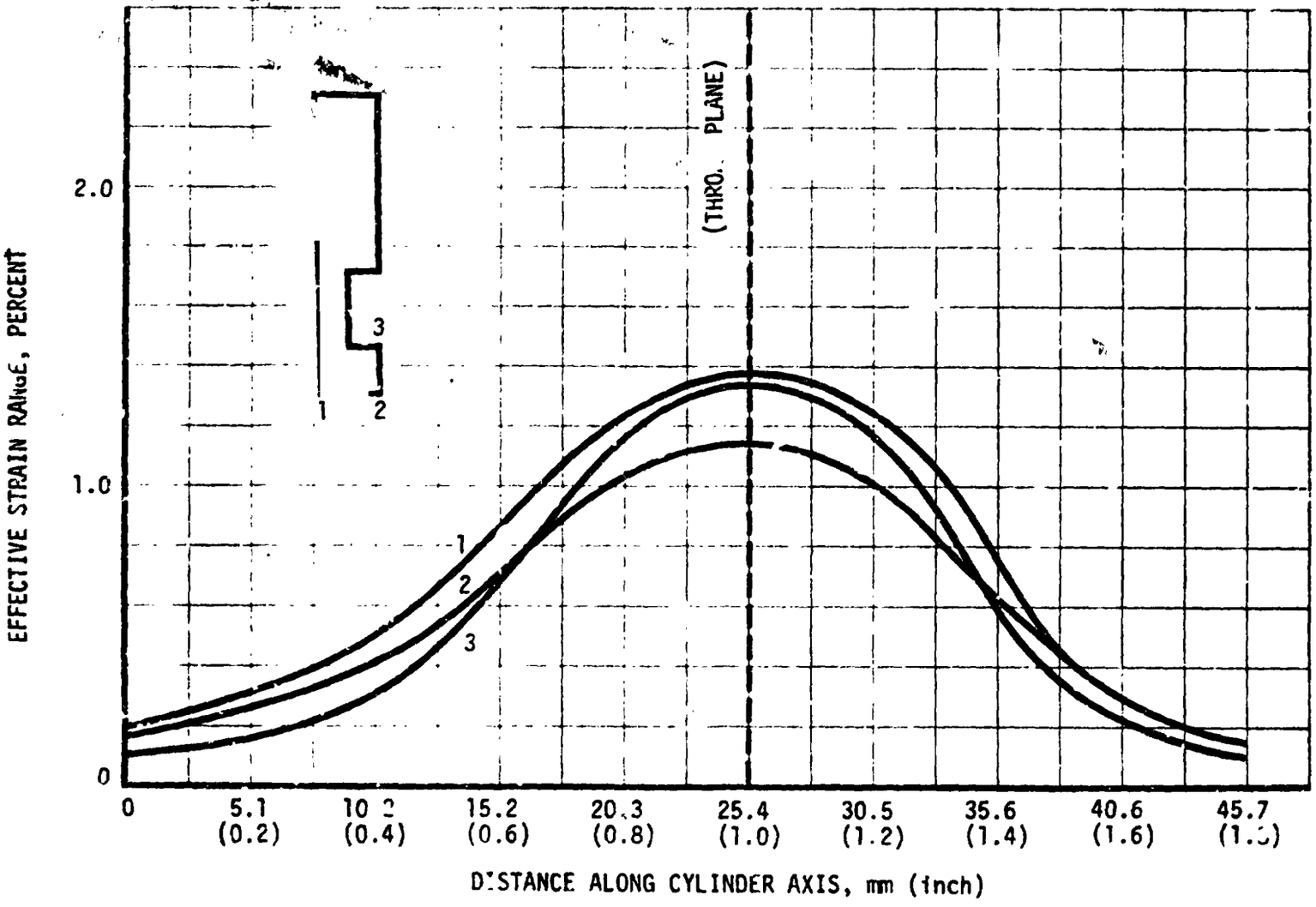

FIGURE 5.2-12 AXIAL DISTRIBUTION OF EFFECTIVE STRAIN RANGE, CONFIGURATION B.1

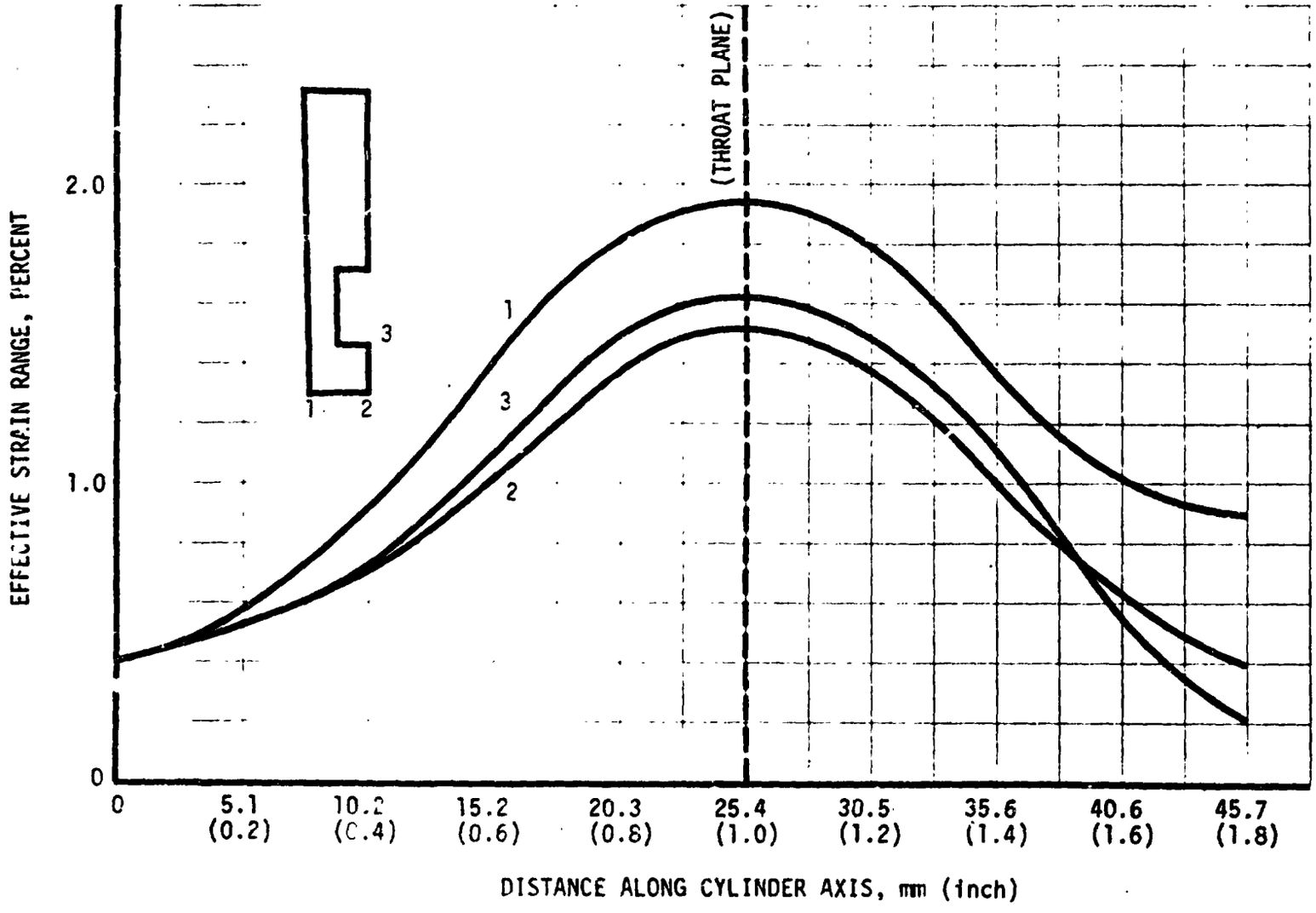

FIGURE 5.2-13 AXIAL DISTRIBUTION OF EFFECTIVE STRAIN RANGE, CONFIGURATION B.2

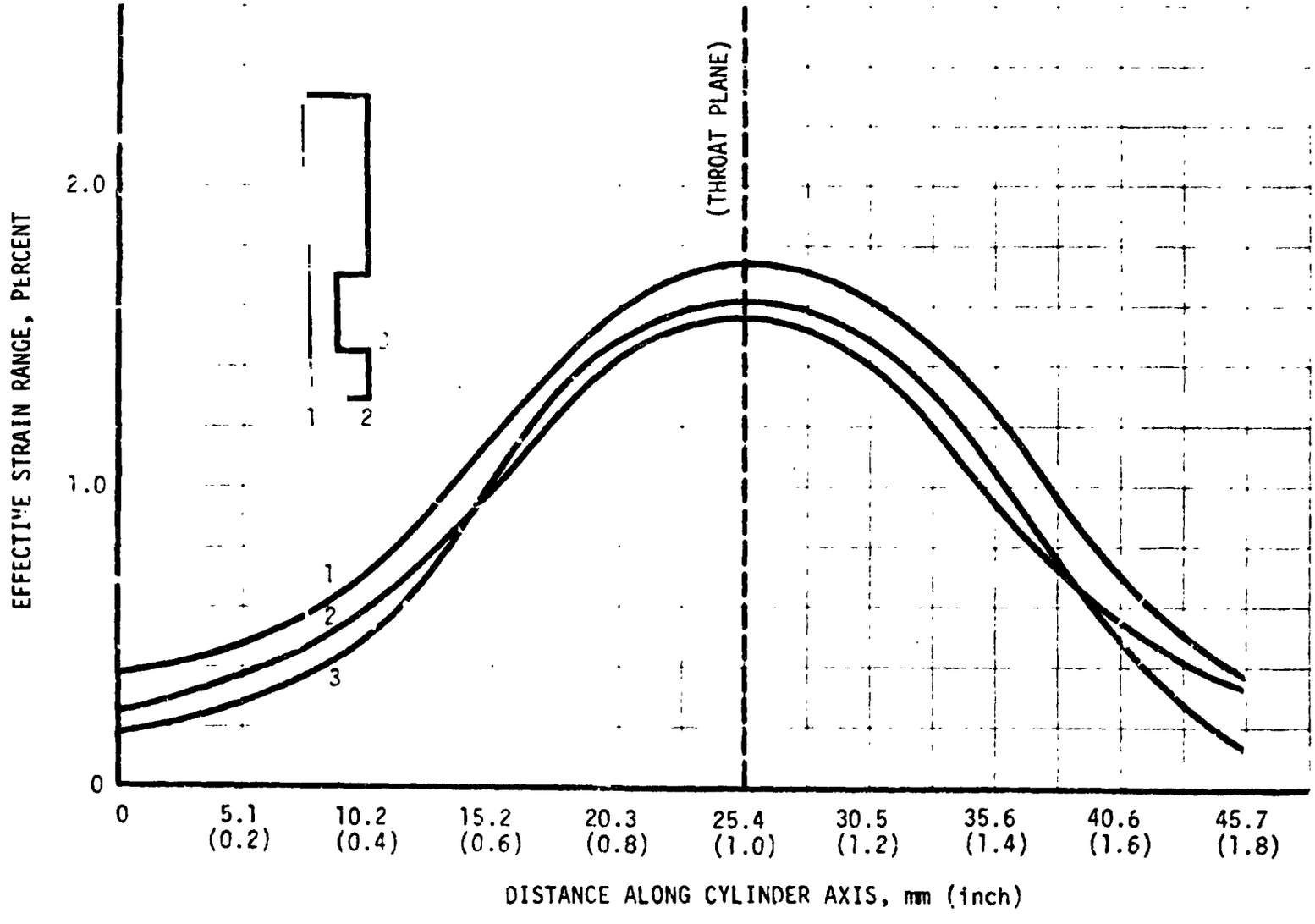

FIGURE 5.2-14 AXIAL DISTRIBUTION OF EFFECTIVE STRAIN RANGE, CONFIGURATION B.3

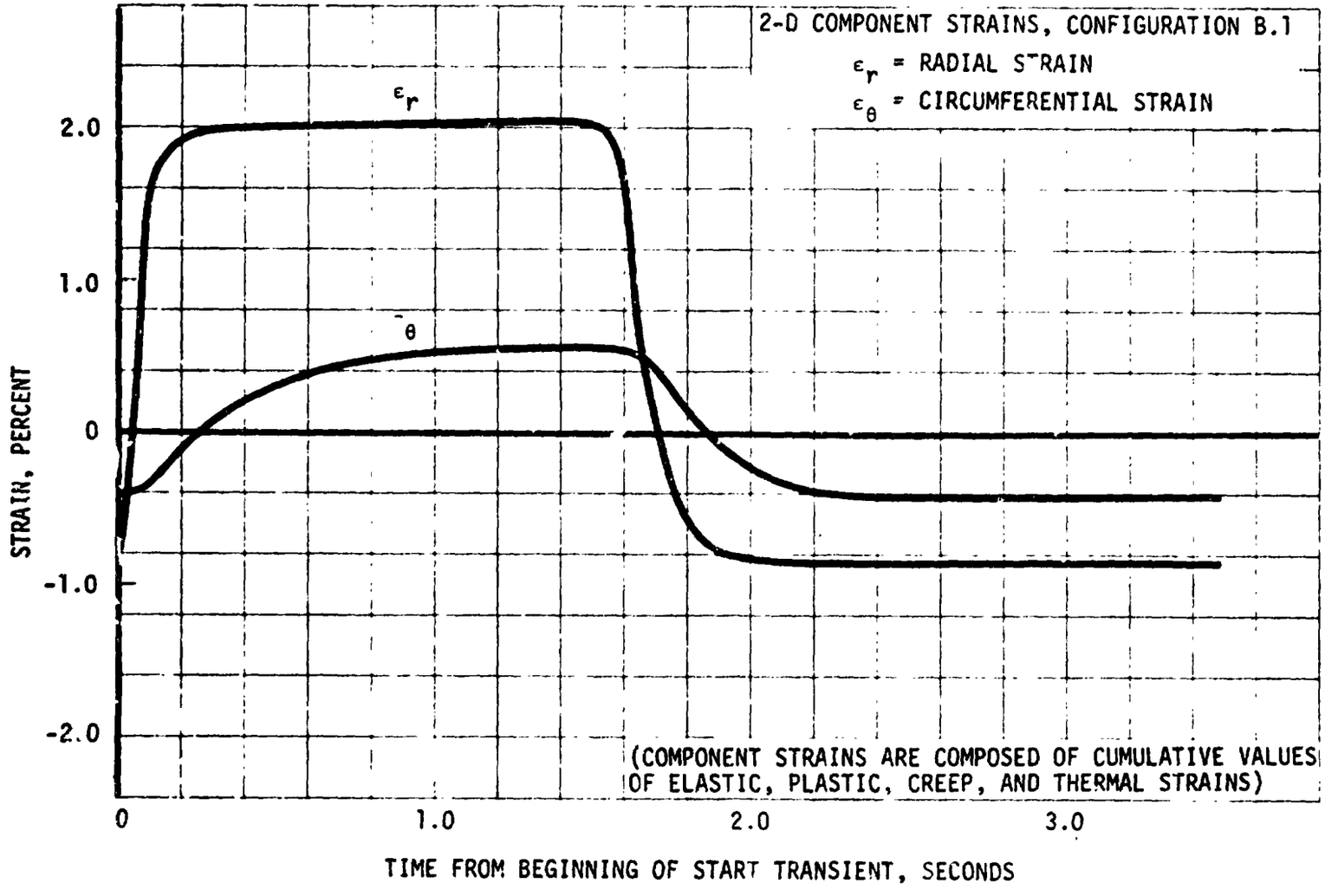

FIGURE 5.3-1 2-D CYCLIC STRAIN ON INNER WALL HEATED SURFACE AT RIB CENTERLINE, CONFIGURATION B.1 THROAT PLANE

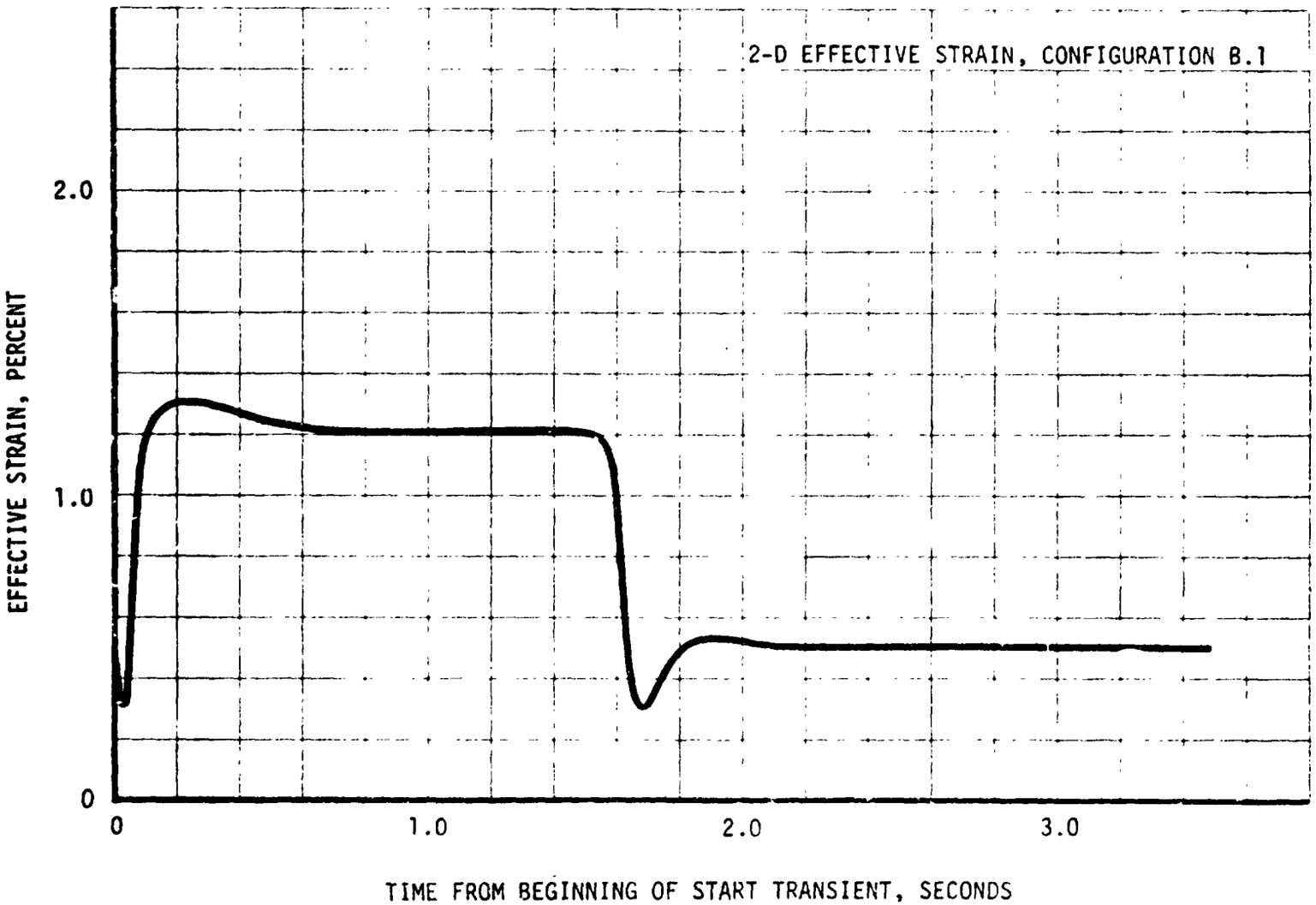

FIGURE 5.3-2 2-D CYCLIC EFFECTIVE STRAIN ON INNER WALL HEATED SURFACE AT RIB CENTERLINE, CONFIGURATION B.1 THROAT PLANE

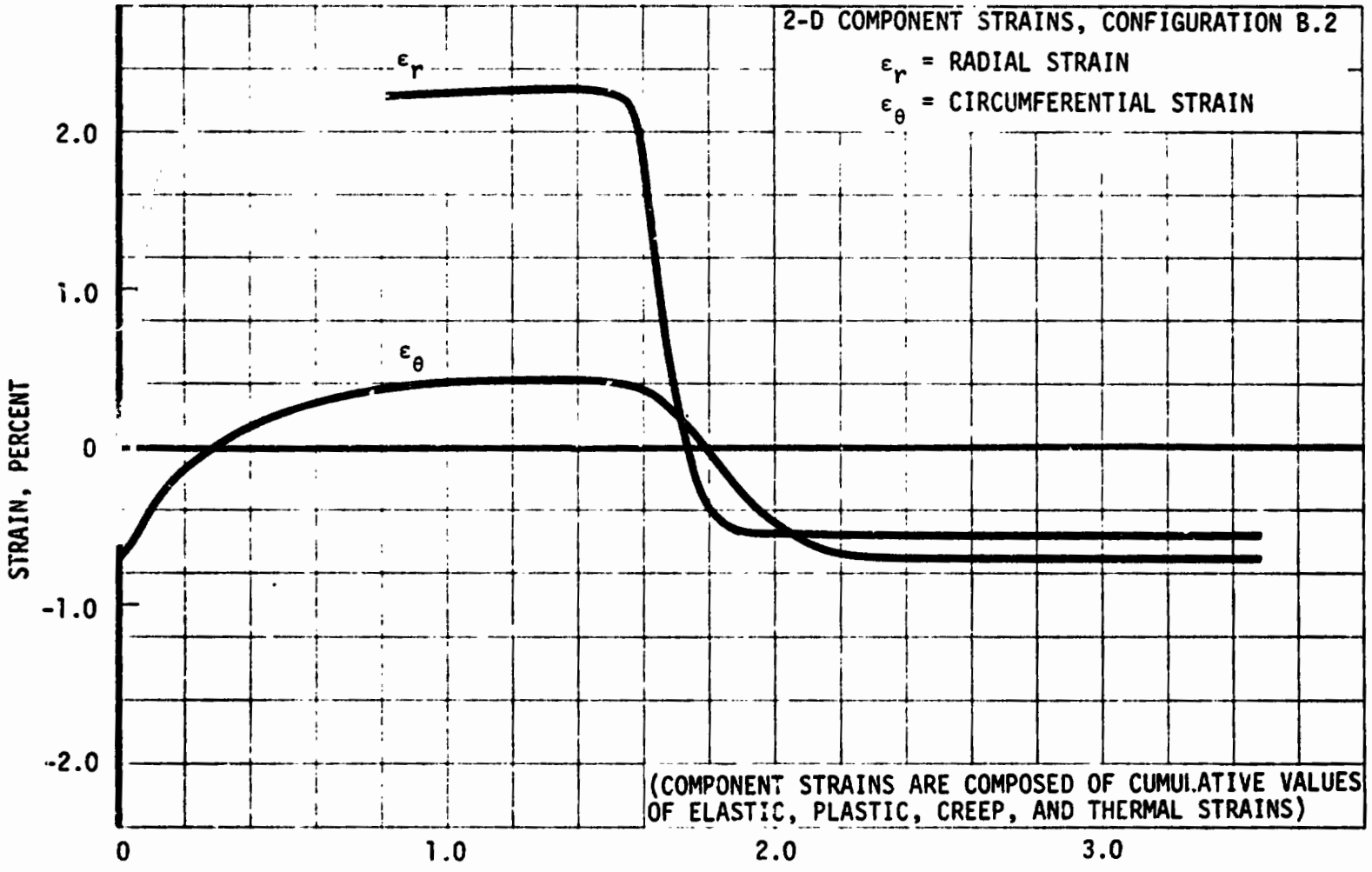

FIGURE 5.3-3 2-D CYCLIC STRAIN ON INNER WALL HEATED SURFACE AT RIB CENTERLINE, CONFIGURATION B.2 THROAT PLANE

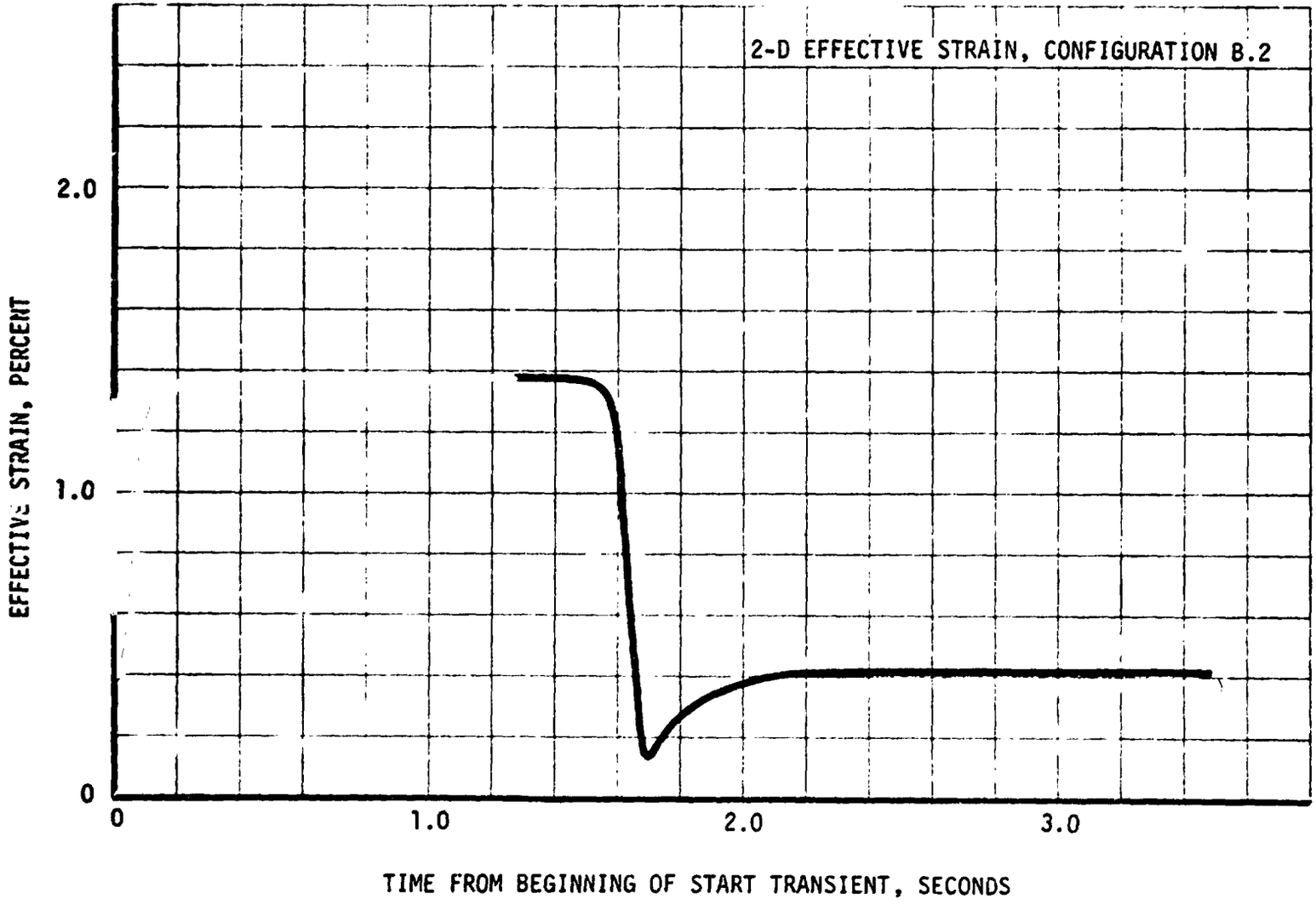

FIGURE 5.3-4 2-D CYCLIC EFFECTIVE STRAIN ON INNER WALL HEATED SURFACE AT RIB CENTERLINE, CONFIGURATION B.2 THROAT PLANE

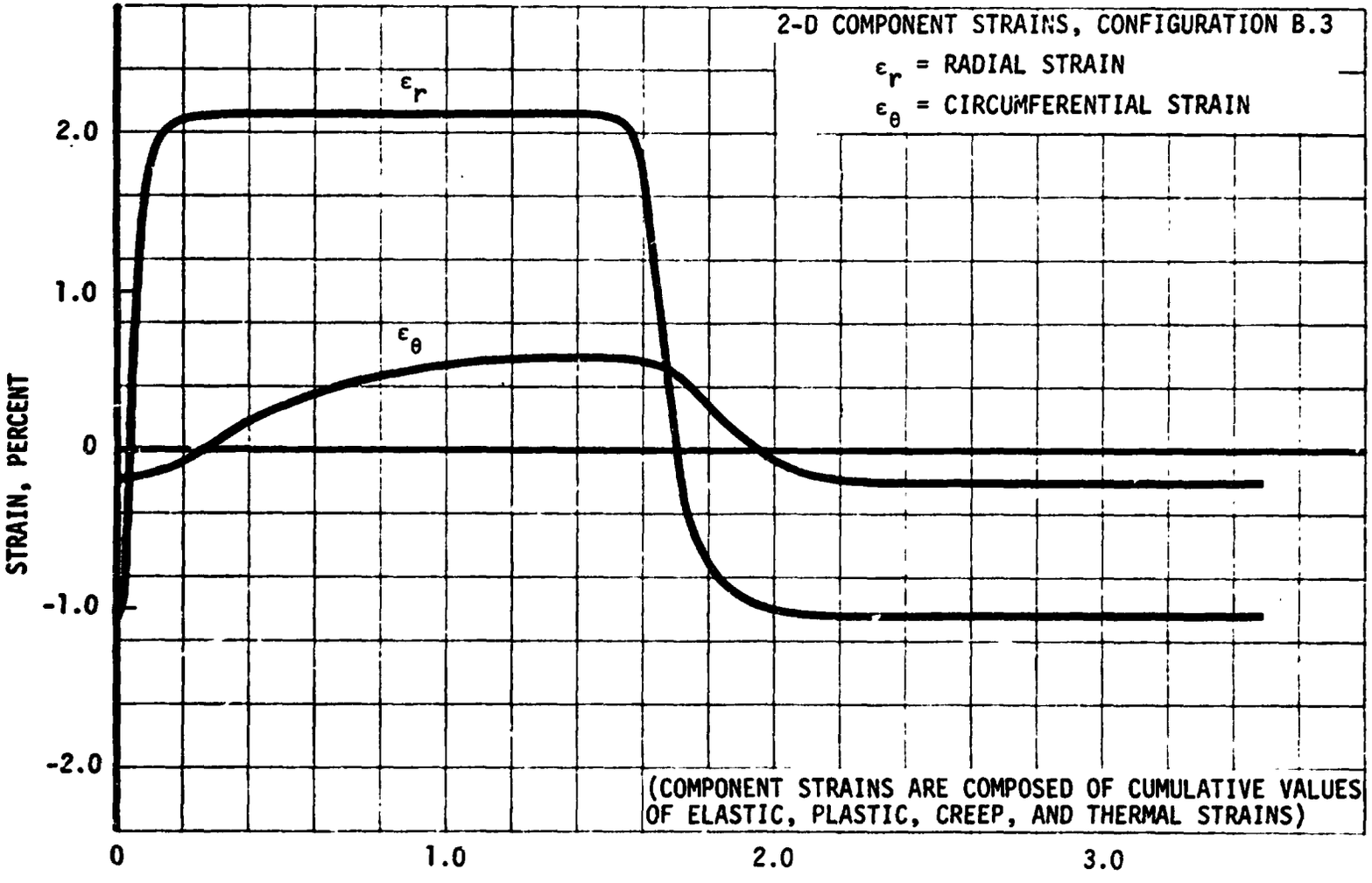

FIGURE 5.3-5 2-D CYCLIC STRAIN ON INNER WALL HEATED SURFACE AT RIB CENTERLINE, CONFIGURATION B.3 THROAT PLANE

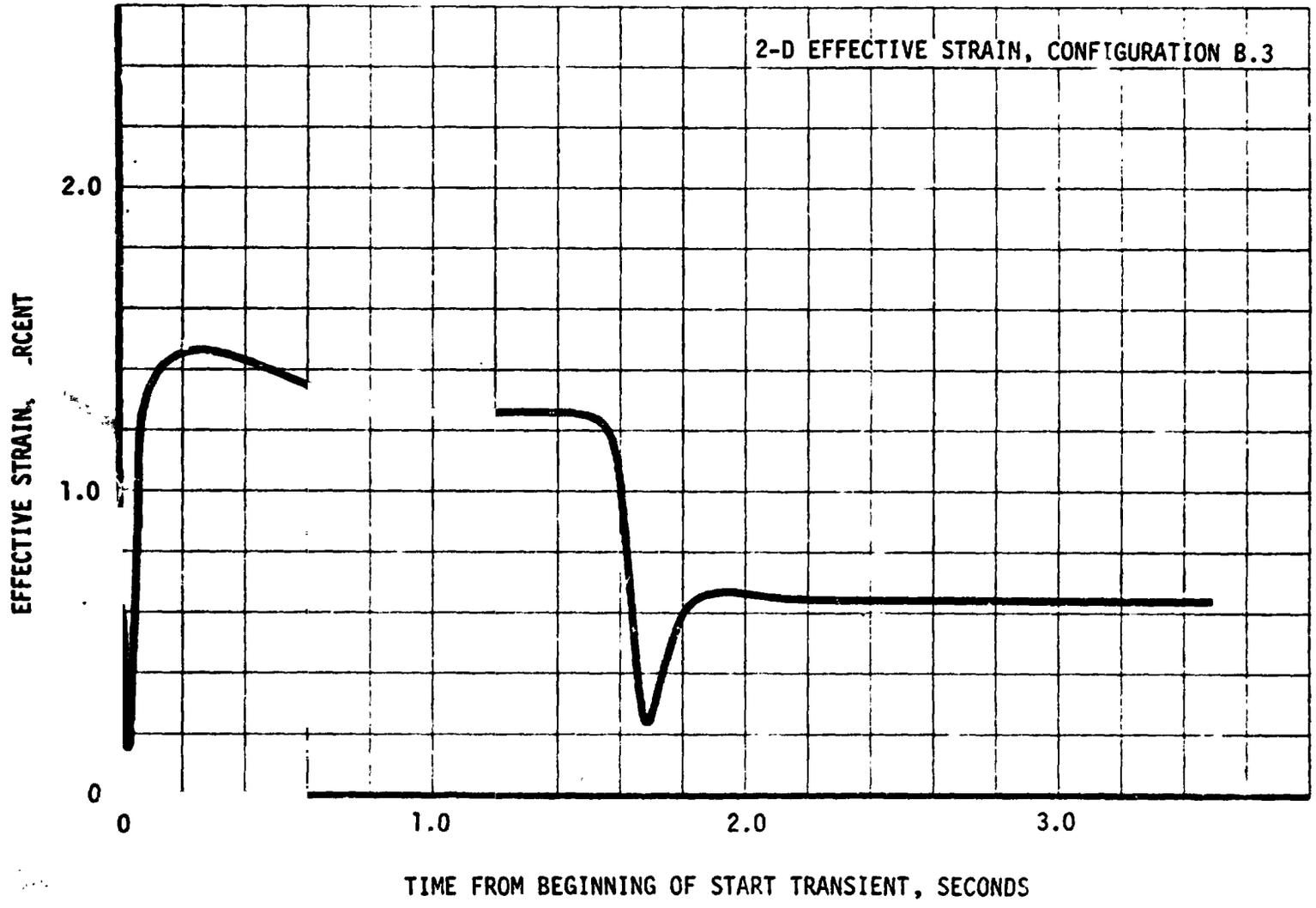

FIGURE 5.3-6 2-D CYCLIC EFFECTIVE STRAIN ON INNER WALL HEATED SURFACE AT RIB CENTERLINE, CONFIGURATION B.3 THROAT PLANE

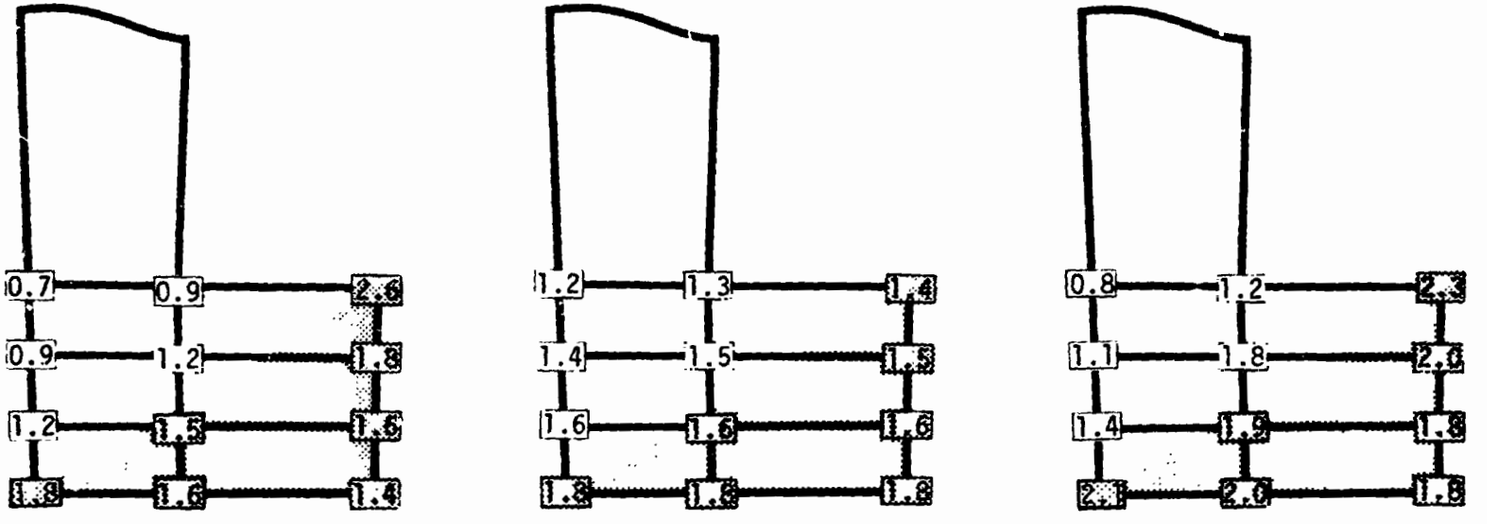

CONFIGURATION B.1 CONFIGURATION B.2 CONFIGURATION B.3

FIGURE 5.3-7 EFFECTIVE STRAIN RANGE DISTRIBUTION (PERCENT) AT CYLINDER THROAT PLANE OF 2-D FINITE ELEMENT MODEL

TABLE 5.3-I COMPARISON OF 2-D AND 3-D THRUST CHAMBER LIFE PREDICTIONS

CONFIGURATION	MODEL	EFFECTIVE STRAIN RANGE (PERCENT)		CYCLES TO FRACTURE	
		MAXIMUM	AVERAGE	MINIMUM	AVERAGE
B.1	2-D	2.6	1.8	800	1700
B.1	3-D	1.4	1.3	3000	3500
B.2	2-D	1.8	1.6	160	210
B.2	3-D	1.9	1.6	150	210
B.3	2-D	2.3	2.0	700	920
B.3	3-D	1.7	1.6	1300	1500

6.0 CONCLUDING REMARKS

The objective of this study was to analytically determine and compare the low-cycle fatigue life of each of the three configurations of the LeRC plug nozzle thrust chamber. The results of the study were obtained from 3-D analyses which predicted cyclic histories of temperature and strain caused by specified boundary conditions. Obviously, the predicted thermomechanical behavior is highly dependant upon the prescribed boundary conditions, and accurate prediction of fatigue life is greatly affected by how closely the specified conditions match the actual operating cycle. If the specified conditions are accurate, the predicted temperatures and strains obtained from the BETA and BOPACE models will closely correspond to typical behavior of the cylinders.

The thermal analysis results from the 3-D Thrust Chamber Life Prediction Study were examined from two standpoints: an assessment of the accuracy of the 3-D analytical model in simulating the thrust chamber's response, and a comparison with 2-D results in attempt to evaluate the validity of the latter. Although final conclusions regarding these two questions depend upon examination of strain and fatigue-life analysis results, certain tentative conclusions can be drawn from the thermal data alone.

The principal question regarding the accuracy of the 3-D thermal model relates to the mesh size of the nodal network. Although some effects of the relatively coarse mesh size were detected in the temperature levels in Figure 4.1-3 and in the temperature gradients indicated in Figure 4.3-3, the general character of the 3-D results supports a conclusion that the model was entirely adequate for purposes of this study.

The corresponding 2-D and 3-D thermal analyses yielded very similar results in terms of throat plane temperature histories and throat plane isotherm patterns. Furthermore, the axial temperature distributions showed little or no axial temperature gradients in the immediate vicinity of the throat planes. Thus, assuming the use of appropriate

6.0 (Continued)

boundary conditions, it appears that a 2-D analysis is capable of accurately predicting thermal response at the throat plane. The boundary conditions for this study, however, vary axially and the influence of boundary values at planes other than the throat plane upon chamber response at the throat plane was impossible to predict without a 3-D analysis. These facts appear to preclude the definition of an appropriate set of effective throat plane boundary conditions for 2-D analysis. Thus, the credibility of a two-dimensional approach remains questionable.

The finite-element model was designed to simulate as closely as possible the behavior of the structure. This requirement determined the mesh size and type of element used in the analysis. Because of loading conditions (temperatures and pressures) and configuration, the 3-D quadratic isoparametric element was required for this study. Results of Section 5.1 indicate the accuracy provided by the relatively coarse mesh of complex elements. The use of complex elements was also warranted by economic considerations. In 3-D problems of this nature, as implied in Section 5.1, the complex element presents a considerable economic advantage over simple (linear) elements. It was also shown in Section 5 that 3-D models are more appropriate than 2-D to these cylinders because measurable extensional and shearing strains along all three coordinate axes will be present at the throat plane during the major portion of the cycle; although the maximum effective strain during heating coincided with a condition of plane-strain, the residual effective strain included nonzero values of all three components of direct strain. Thus the effective strain range of the cycle can be determined only with the 3-D model. It was noted that residual effective strains predicted by the 2-D plane-strain models were significantly larger than the 3-D values, and in general, the 2-D effective ranges of strain were larger than the 3-D results.

The most significant reason for comparable behavior in the 2-D and 3-D models of B.2 appears to be the influence of the closeout wall on inner wall displacement. The relatively thick EFCu outer wall with greater

6.0 (Continued)

stiffness than the OFHC inner wall imposed more constraint on the B.2 inner wall than in configurations B.1 and B.3. This constraint was characterized by the deformations of the heated and outer surfaces of the cylinder. For example, at time = 0.15 second after startup the axial displacement between the stations located 3.8 mm either side of the throat plane was only 0.0015 mm greater at the heated surface than the outer surface of B.2. The corresponding difference in B.1 (which was subject to the same loading) was 0.012 mm. Thus, the B.1 inner wall with higher yield strengths and higher tangent moduli, tended to govern structural behavior. The relatively flexible inner wall of B.2, on the other hand, was constrained by the outer wall which was thicker, cooler, and had higher mechanical properties. Obviously selection of the closeout wall material and its geometry have a significant effect on structural behavior and fatigue life of the inner wall.

The description of material characteristics is important in that the data must define material behavior in a given range of temperature, strain and strain rate. Thus, the constitutitive data are intended only to describe a limited number of physical phenomena decided at the outset for a given material. Unfortunately, available materials data did not include all the information necessary to characterize the thrust chamber. For example, stress-strain hysteresis loops necessary for defining hardening characteristics were not available. Thus, static monotonic stress-strain curves were used, and no isotropic hardening or change in kinematic hardening from cycle-to-cycle was assumed for the high strain rates expected in the critical regions of the chamber. The use of the monotonic stress-strain curves probably resulted in somewhat larger than actual inelastic strains because copper yield strengths and moduli probably increase with increasing rates of strain. Material properties derived from laboratory test conditions which more closely simulate the high temperature-high strain rate thrust chamber cycle would provide data for greater confidence in predicted thrust chamber behavior.

6.0 (Continued)

Obviously the interpretation of low-cycle fatigue data and determination of the life prediction curve will have a significant effect on the predicted life of the structure. For example, a 20 percent vertical shift of the curve for 1/2 hard Amzirc (Figure 3.1-8) results in a 50 percent increase in life at a strain range of 2 percent. Even more important is the slope of the life prediction curve.

Although creep damage was insignificant in the plug nozzle chamber, as temperatures and burn times increase creep would probably have a measurable effect on low-cycle fatigue life. Creep data for this study were very limited. Accurate assessment of cyclic creep behavior, especially under more severe conditions, can be achieved only if appropriate test data are available to characterize first and second stages of creep.

7.0 REFERENCES

1. J. J. Esposito and R. F. Zabora, Thrust Chamber Life Prediction - Mechanical and Physical Properties of High Performance Rocket Nozzle Materials, NASA CR-134806, NASA Lewis Research Center Contract NAS3-17838, March 1975.

2. W. H. Armstrong and E. W. Brogren, Thrust Chamber Life Prediction - Plug Nozzle Centerbody and Cylinder Life Analysis, NASA CR-134822, NASA Lewis Research Center Contract NAS3-17838, May 1975.

3. W. H. Armstrong and E. W. Brogren, Thrust Chamber Life Prediction - Fatigue Life Parametric Study, NASA CR-134823, NASA Lewis Research Center Contract NAS3-17838, May 1975.

APPENDIX

TWO-DIMENSIONAL LIFE PREDICTION ANALYSIS OF CONFIGURATION B.2

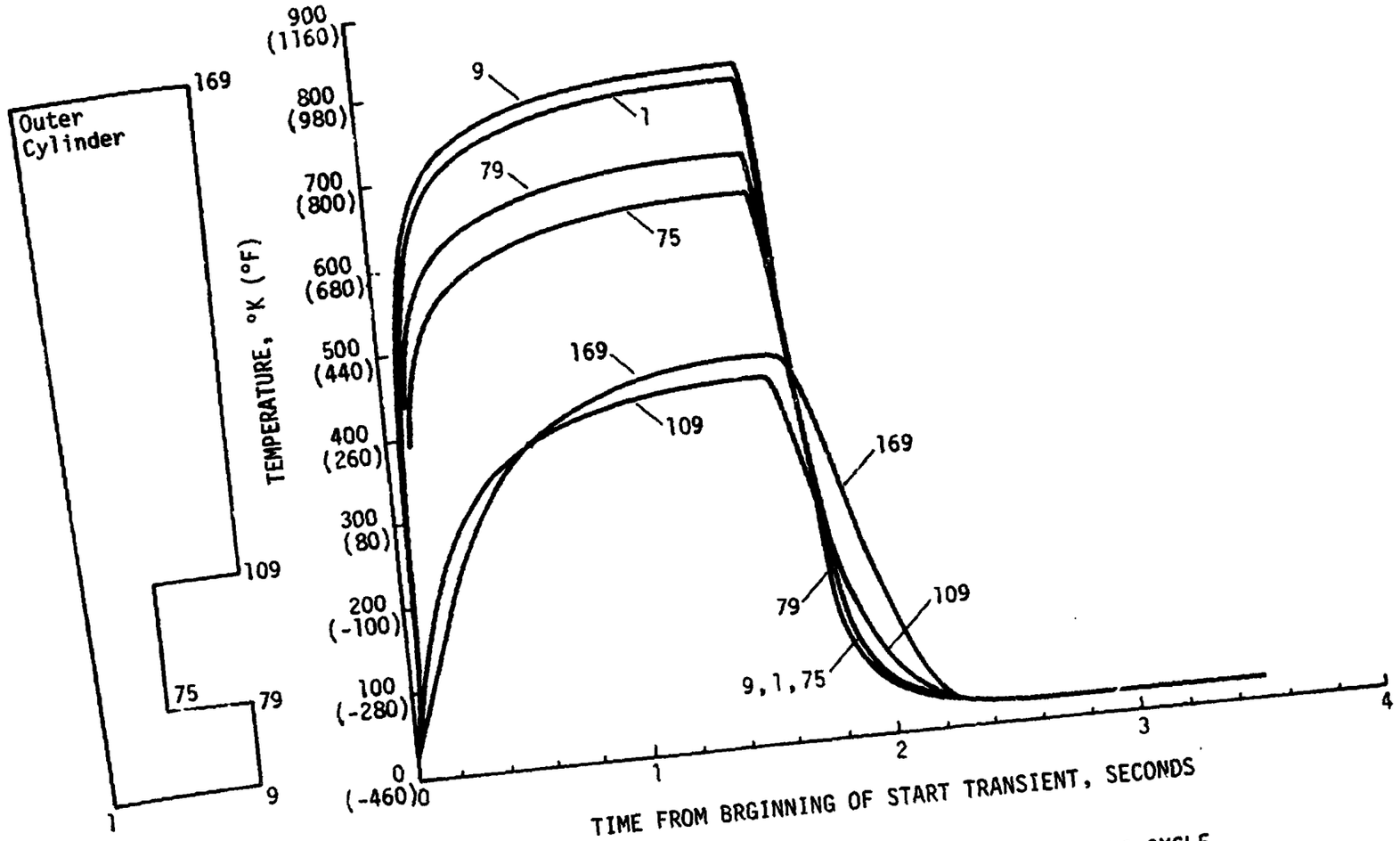

REPRESENTATIVE 2-DIMENSIONAL TEMPERATURES FOR HEATING-COOLING CYCLE AT THROAT PLANE OF OUTER CYLINDER

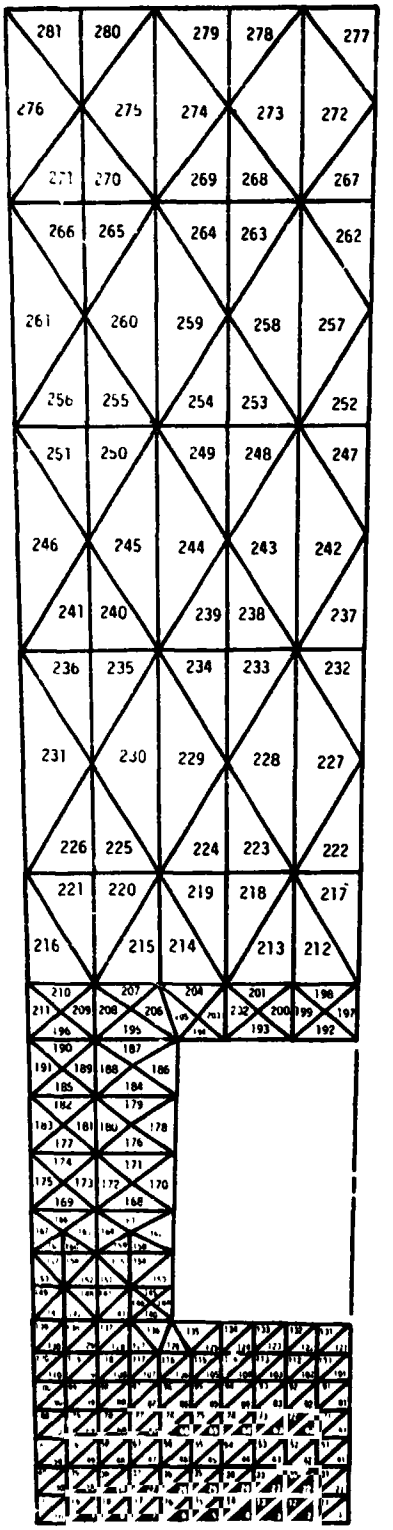

TOTAL NUMBER OF ELEMENTS = 281
TOTAL NUMBER OF NODES = 174
TOTAL NUMBER OF FREEDOMS = 348

PLUG NOZZLE OUTER CYLINDER 2-D FINITE ELEMENT MODEL
SHOWING ELEMENT IDENTIFICATION NUMBERS

PREDICTED 2-DIMENSIONAL TEMPERATURES AND STRAINS FOR
INITIAL CHILLDOWN AND TYPICAL HEATING-COOLING CYCLE - CONFIGURATION B.2

ELEMENT	TIME (sec)	*CUMULATIVE STRAINS (%) ε_r	ε_θ	ε_z	ε_{eff}	TEMP. (°R)
1	0.030	-.12	.06	.09	.13	419
10		-.11	.06	.09	.12	424
131		-.14	.07	.10	.15	412
135		-.14	.10	.09	.16	418
1	0.050	-.22	.10	.15	.23	346
10		-.20	.09	.15	.22	354
131		-.26	.12	.16	.27	333
135		-.26	.17	.16	.28	343
1	0.100	-.26	.09	.21	.28	282
10		-.24	.08	.20	.26	290
131		-.29	.11	.21	.31	272
135		-.30	.16	.21	.32	283
1	0.200	-.29	.04	.26	.32	212
10		-.26	.01	.26	.30	218
131		-.30	.04	.27	.33	206
135		-.32	.08	.26	.35	213
1	0.300	-.29	.00	.30	.34	165
10		-.26	-.04	.32	.32	168
131		-.30	-.01	.31	.35	160
135		-.32	.02	.30	.36	165
1	1.650	-.30	-.10	.40	.42	50
10	(STARTUP)	-.24	-.17	.40	.40	50
131		-.30	-.11	.40	.42	50
135		-.30	-.10	.40	.42	50
1	1.665	-.27	-.11	.35	.37	107
10		-.21	-.18	.35	.37	104
131		-.27	-.12	.36	.38	97
135		-.28	-.11	.36	.39	94
1	1.680	-.16	-.18	.24	.27	244
10		-.08	-.28	.25	.31	235
131		-.21	-.16	.28	.31	196
135		-.20	-.18	.29	.32	182

*COMPONENT STRAINS DO NOT INCLUDE THERMAL STRAIN. SUBSCRIPTS r, θ, z DENOTE RADIAL, TANGENTIAL AND AXIAL STRAINS RESPECTIVELY. TIME ORIGIN IS THE BEGINNING OF INITIAL CHILLDOWN. THE CUMULATIVE THERMAL STRAIN IS EQUAL TO THE NEGATIVE VALUE LISTED FOR ε_z.

ELEMENT	TIME (sec)	CUMULATIVE STRAINS (%) ε_r	ε_θ	ε_z	ε_{eff}	TEMP. (°R)
1	1.685	-.06	-.22	.18	.23	315
10		.02	-.34	.19	.31	303
131		-.14	-.18	.23	.27	249
135		-.13	-.22	.25	.29	230
1	1.690	.06	-.28	.12	.25	392
10		.15	-.40	.13	.36	376
131		-.05	-.22	.18	.24	307
135		-.04	-.27	.21	.27	281
1	1.695	.21	-.35	.03	.33	492
10		.30	-.48	.05	.46	470
131		.06	-.28	.12	.25	383
135		.07	-.32	.15	.29	349
1	1.700	.37	-.43	-.06	.46	590
10		.45	-.56	-.03	.59	563
131		.18	-.33	.06	.30	461
135		.18	-.38	.09	.35	419
1	1.706	.57	-.52	-.16	.64	701
10		.65	-.66	-.13	.76	668
131		.33	-.39	-.03	.42	561
135		.33	-.46	.02	.46	510
1	1.712	.72	-.59	-.25	.78	792
10		.80	-.74	-.21	.90	755
131		.47	-.45	-.11	.54	645
135		.46	-.52	-.05	.56	587
1	1.725	.92	-.66	-.37	.97	917
10		.98	-.81	-.33	1.07	876
131		.65	-.52	-.22	.70	764
135		.64	-.58	-.16	.72	700
1	1.738	1.05	-.71	-.46	1.10	1009
10		1.10	-.85	-.42	1.18	969
131		.77	-.56	-.31	.81	852
135		.76	-.62	-.24	.82	785
1	1.744	1.09	-.72	-.49	1.14	1039
10		1.14	-.86	-.45	1.22	996
131		.80	-.56	-.34	.84	880
135		.79	-.63	-.27	.85	812

ELEMENT	TIME (sec)	CUMULATIVE STRAINS (%) ε_r	ε_θ	ε_z	ε_{eff}	TEMP. (°R)
1	1.750	1.13	-.73	-.52	1.18	1064
10		1.18	-.86	-.47	1.25	1022
131		.83	-.56	-.36	.87	905
135		.82	-.63	-.29	.88	836
1	1.775	1.20	-.73	-.59	1.24	1125
10		1.24	-.86	-.54	1.31	1083
131		.87	-.55	-.41	.90	963
135		.86	-.61	-.35	.91	895
1	1.800	1.26	-.73	-.65	1.30	1184
10		1.30	-.85	-.61	1.36	1143
131		.92	-.53	-.47	.95	1021
135		.91	-.60	-.40	.94	953
1	1.850	1.30	-.69	-.71	1.34	1239
10		1.34	-.80	-.67	1.38	1199
131		.94	-.48	-.53	.96	1074
135		.93	-.53	-.46	.95	1008
1	1.950	1.32	-.62	-.78	1.35	1299
10		1.36	-.72	-.74	1.39	1263
131		.95	-.39	-.60	.97	1133
135		.94	-.43	-.53	.95	1071
1	2.500	1.33	-.45	-.90	1.36	1413
10		1.36	-.52	-.87	1.38	1384
131		.94	-.21	-.72	.98	1244
135		.92	-.22	-.66	.94	1190
1	2.850	1.33	-.42	-.92	1.37	1432
10		1.36	-.50	-.89	1.39	1402
131		.94	-.20	-.74	.99	1262
135		.92	-.20	-.68	.95	1210
1	3.200	1.33	-.42	-.93	1.37	1438
10	(SHUTDOWN)	1.36	-.50	-.90	1.39	1408
131		.94	-.19	-.74	.99	1267
135		.92	-.20	-.69	.95	1216
1	3.205	1.32	-.40	-.91	1.35	1419
10		1.35	-.48	-.88	1.38	1391
131		.93	-.18	-.73	.97	1252
135		.90	-.18	-.67	.93	1202

ELEMENT	TIME (sec)	CUMULATIVE STRAINS (%) ε_r	ε_θ	ε_z	ε_{eff}	TEMP. (°R)
1	3.210	1.30	-.39	-.89	1.32	1400
10		1.32	-.46	-.86	1.34	1372
131		.91	-.17	-.71	.95	1235
135		.89	-.16	-.66	.91	1187
1	3.215	1.28	-.38	-.87	1.30	1382
10		1.30	-.44	-.84	1.32	1356
131		.90	-.16	-.69	.93	1220
135		.87	-.14	-.64	.89	1174
1	3.220	1.26	-.36	-.85	1.28	1361
10		1.28	-.42	-.82	1.29	1336
131		.88	-.14	-.67	.91	1203
135		.85	-.12	-.62	.87	1158
1	3.225	1.24	-.35	-.83	1.25	1344
10		1.26	-.40	-.80	1.26	1320
131		.86	-.13	-.66	.89	1189
135		.83	-.10	-.61	.84	1146
1	3.230	1.22	-.33	-.80	1.22	1323
10		1.23	-.38	-.78	1.23	1300
131		.83	-.12	-.64	.86	1171
135		.80	-.09	-.59	.82	1130
1	3.240	1.16	-.30	-.76	1.16	1285
10		1.17	-.34	-.74	1.17	1265
131		.79	-.09	-.60	.81	1139
135		.75	-.05	-.56	.76	1101
1	3.250	1.11	-.26	-.72	1.10	1250
10		1.12	-.30	-.71	1.10	1232
131		.70	-.06	-.57	.76	1110
135		.70	-.02	-.53	.71	1075
1	3.260	.98	-.20	-.65	.98	1186
10		1.00	-.24	-.64	.99	1170
131		.63	-.01	-.51	.66	1053
135		.58	.04	-.48	.61	1022
1	3.280	.75	-.09	-.52	.75	1068
10		.77	-.12	-.51	.76	1058
131		.43	.08	-.40	.48	950
135		.39	.14	-.38	.45	926

ELEMENT	TIME (sec)	CUMULATIVE STRAINS (%) ε_r	ε_θ	ε_z	ε_{eff}	TEMP. (°R)
1	3.300	.54	.00	-.40	.54	951
10		.56	-.03	-.40	.56	946
131		.26	.14	-.30	.34	846
135		.22	.22	-.29	.34	831
1	3.325	.34	.07	-.27	.35	814
10		.37	.04	-.27	.37	813
131		.10	.20	-.19	.23	727
135		.05	.28	-.18	.26	718
1	3.350	.15	.13	-.14	.19	679
10		.18	.10	-.14	.20	682
131		-.06	.24	-.07	.21	608
135		-.10	.33	-.07	.28	607
1	3.375	.01	.16	-.04	.12	569
10		.05	.13	-.04	.10	574
131		-.17	.25	.01	.24	512
135		-.21	.34	.01	.32	515
1	3.400	-.11	.18	.06	.16	460
10		-.06	.14	.05	.12	468
131		-.25	.25	.09	.30	417
135		-.29	.34	.09	.37	424
1	3.425	-.18	.17	.13	.22	374
10		-.13	.13	.12	.17	384
131		-.30	.23	.16	.34	343
135		-.34	.32	.15	.40	352
1	3.450	-.24	.16	.19	.28	298
10		-.18	.12	.18	.22	309
131		-.34	.21	.21	.37	276
135		-.38	.30	.20	.42	287
1	3.500	-.29	.12	.28	.34	196
10		-.23	.06	.27	.2[illegible]	206
131		-.38	.15	.29	.40	186
135		-.42	.22	.28	.45	197
1	3.700	-.24	-.11	.36	.36	104
10		-.17	-.20	.35	.36	106
131		-.31	-.12	.36	.40	101
135		-.35	-.09	.35	.41	104

ELEMENT	TIME (sec)	CUMULATIVE STRAINS (%) ε_r	ε_θ	ε_z	ε_{eff}	TEMP. (°R)
1	3.900	-.23	-.19	.40	.41	50
10	to	-.15	-.29	.40	.42	50
131	5.150	-.28	-.20	.40	.43	50
135		-.32	-.18	.40	.44	50

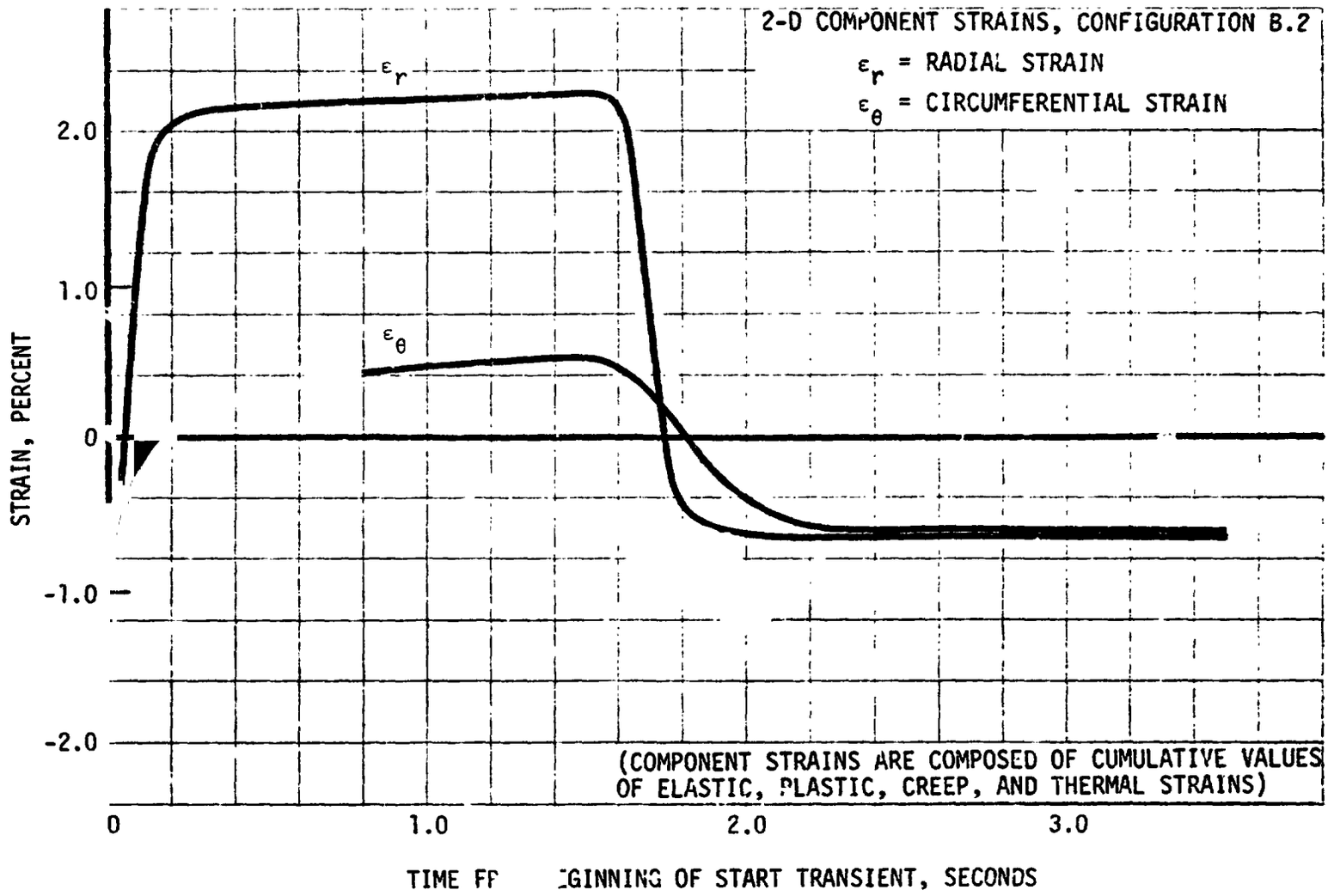

2-D CYCLIC STRAIN AT ELEMENT #1, CONFIGURATION B.2

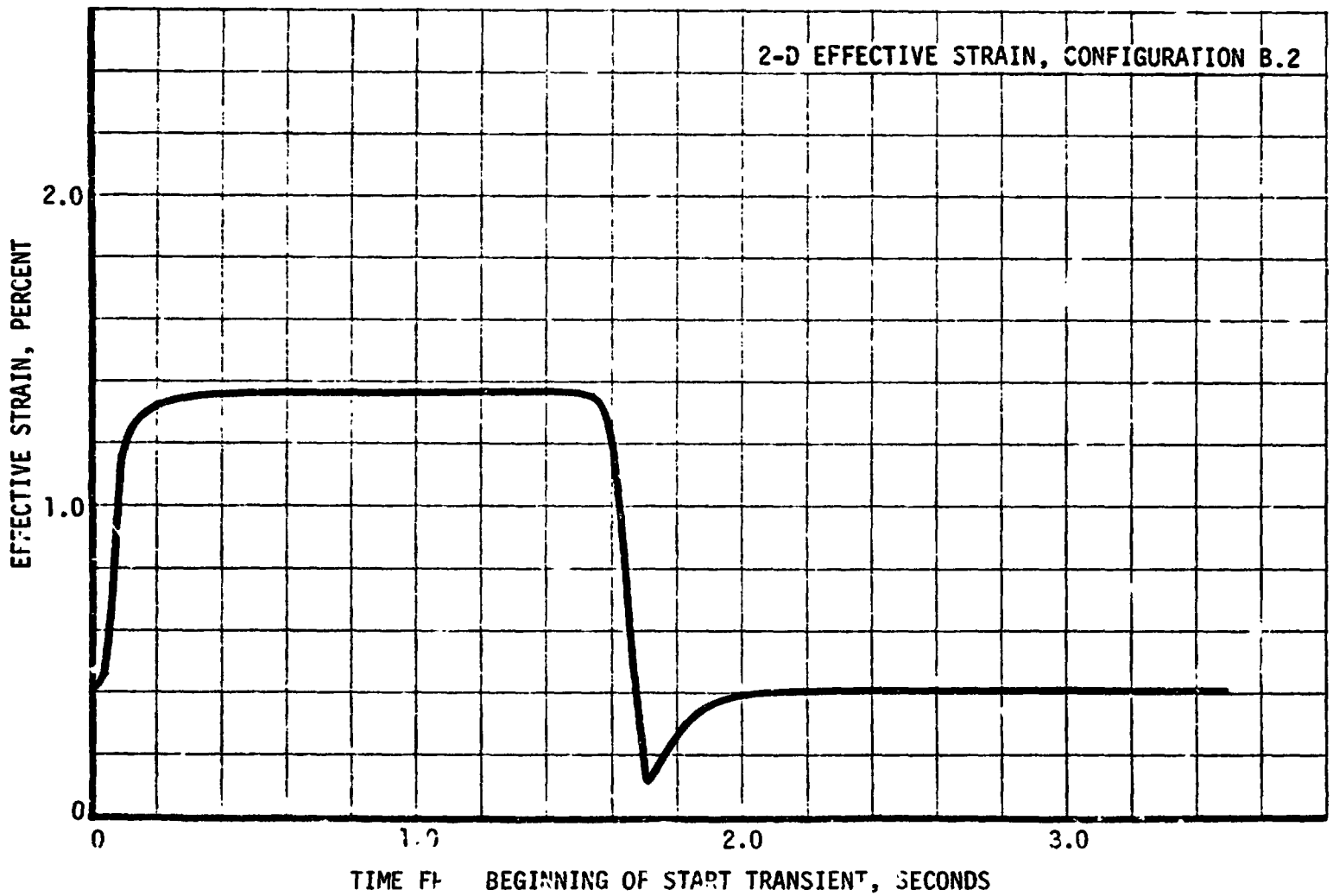

2-D CYCLIC EFFECTIVE STRAIN AT ELEMENT #1, CONFIGURATION B.2

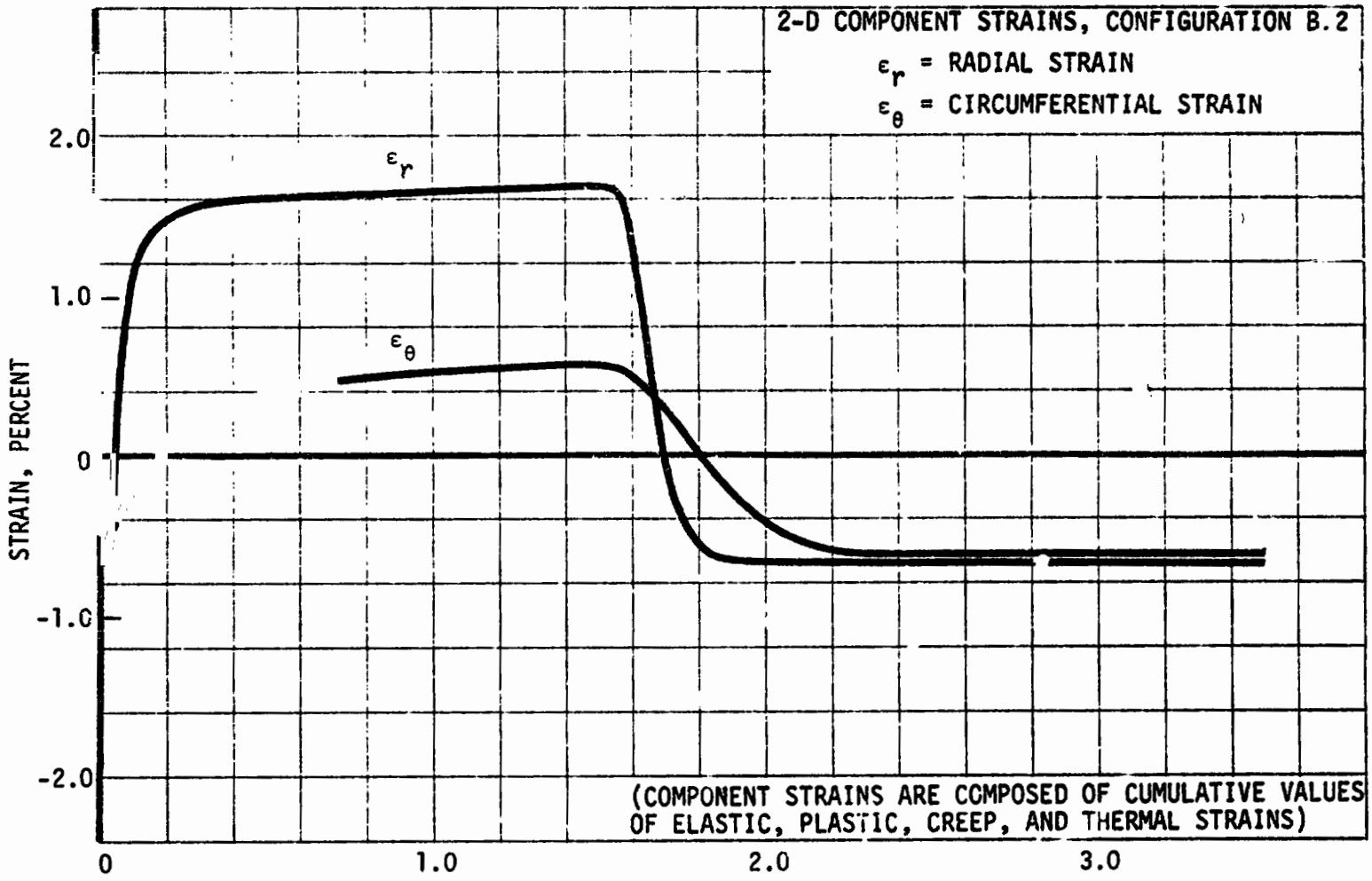

2-D CYCLIC STRAIN AT ELEMENT #131, CONFIGURATION B.2

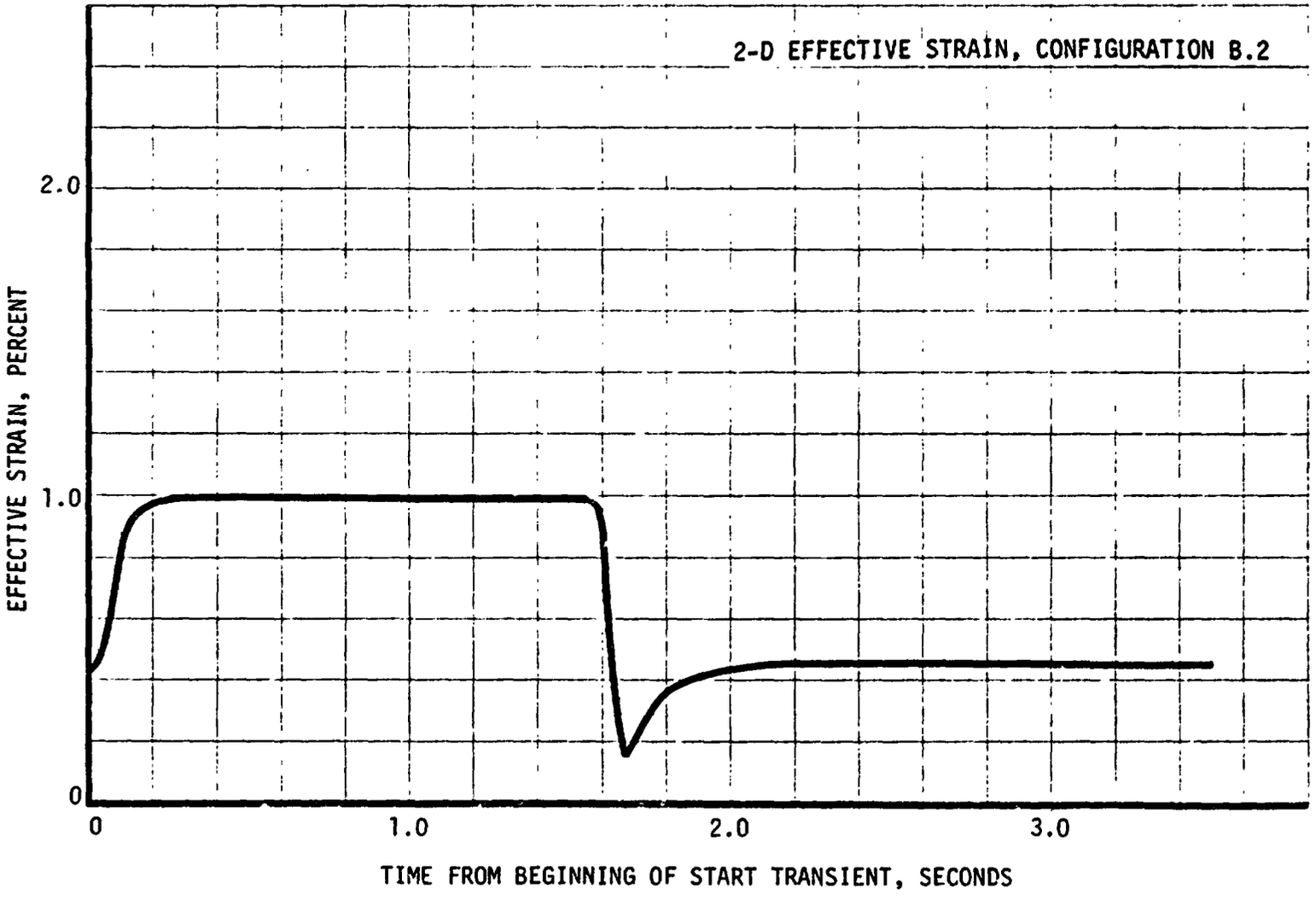

2-D CYCLIC EFFECTIVE STRAIN AT ELEMENT #131, CONFIGURATION B.2

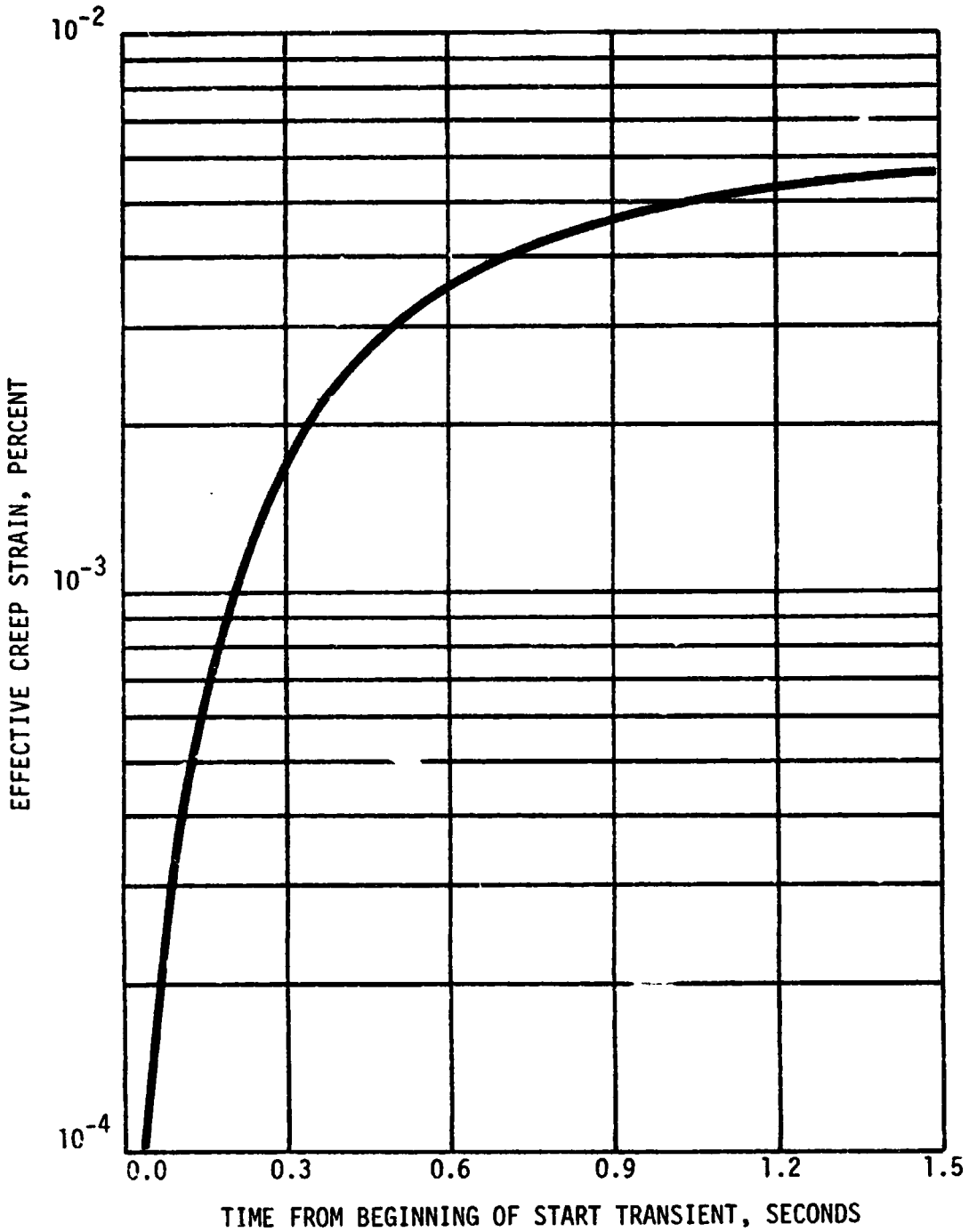

FIRST CYCLE EFFECTIVE CREEP STRAIN FROM 2-D ANALYSIS
OF CONFIGURATION B.2

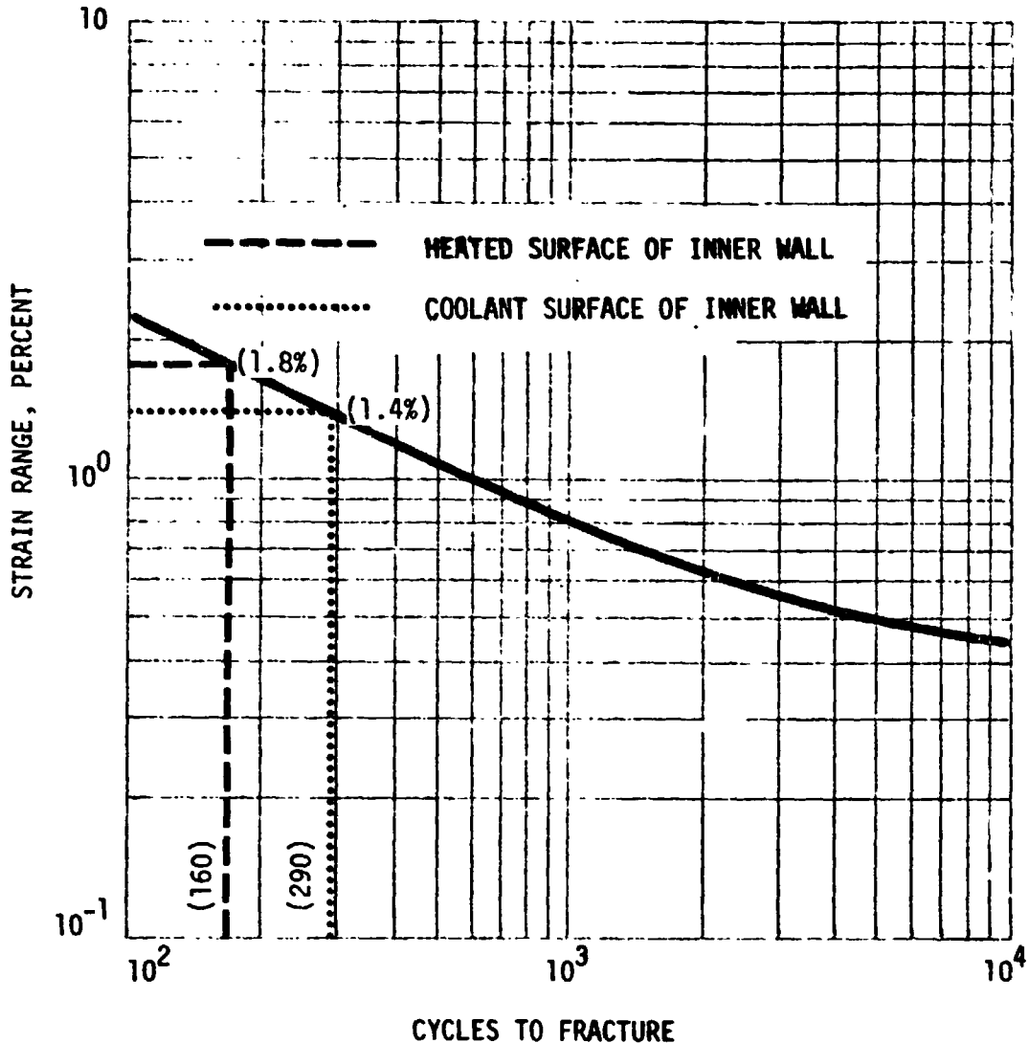

PREDICTED LOW-CYCLE FATIGUE LIFE FROM 2- DIMENSIONAL ANALYSIS OF THROAT PLANE REGION OF CONFIGURATION B.2

SUMMARY OF MAXIMUM STRAIN CONDITIONS IN 2-DIMENSIONAL
FINITE-ELEMENT MODEL OF OUTER CYLINDER (CONFIGURATION B.2)

ELEMENT I. D. NO.	TOTAL EFFECTIVE STRAIN (%) TIME=1.55 SEC	TIME=3.50 SEC	TOTAL EFFECTIVE STRAIN RANGE (%)	MAXIMUM TEMPERATURE (°R)	LIFE (CYCLES)
1	1.37	0.41	1.78	1438	160
10	1.39	0.42	1.81	1408	160
131	0.99	0.43	1.42	1267	290
135	0.95	0.44	1.39	1216	290

TIME FROM BEGINNING OF START TRANSIENT, SECONDS